

**DEVELOPMENT OF  $\text{Al}_2\text{O}_3$  -  $\text{Sm}_2\text{SrAl}_2\text{O}_7$  CERAMIC  
COMPOSITE THERMAL BARRIER COATINGS FOR  
HIGH TEMPERATURE APPLICATIONS**

Thesis

Submitted in partial fulfilment of the requirements for the degree of

**DOCTOR OF PHILOSOPHY**

by

**FREDY JAMES J**



**Department of Metallurgical and Materials Engineering  
NATIONAL INSTITUTE OF TECHNOLOGY, KARNATAKA  
SURATHKAL, MANGALORE – 575025**

**July, 2023**



## DECLARATION

I hereby declare that the research thesis entitled “**Development of  $\text{Al}_2\text{O}_3$  -  $\text{Sm}_2\text{SrAl}_2\text{O}_7$  ceramic composite thermal barrier coatings for high temperature applications**” which is being submitted to the National Institute of Technology, Karnataka, Surathkal, in partial fulfilment of the requirements for the award of the Degree of **Doctor of Philosophy** in the Department of Metallurgical and Materials Engineering, is a bonafide report of the research work carried out by myself. The material contained in this research thesis has not been submitted to any university for the award of any degree.

**Place: NITK Surathkal**

**Date: 11-07-2023**



Fredy James J

Register Number: 177MT003

Department of Metallurgical  
and Materials Engineering

NITK Surathkal



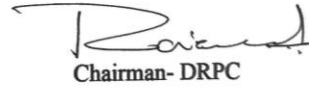
## CERTIFICATE

This is to certify that the Research Thesis entitled "**Development of  $\text{Al}_2\text{O}_3$  -  $\text{Sm}_2\text{SrAl}_2\text{O}_7$  ceramic composite thermal barrier coatings for high temperature applications**" submitted by Mr. Fredy James J (177MT003) as the record of the research work carried out by him, is accepted as the Research Thesis submission in partial fulfilment of the requirements for the award of degree of Doctor of Philosophy.



Research Guide

Dr. Shashi Bhushan Arya  
Assistant Professor  
Metallurgical & Materials Engineering  
NITK Surathkal



Chairman - DRPC

Metallurgical & Materials  
Engineering  
NITK Surathkal

Chairman - DRPC  
Dept. of Metallurgical and Materials Engineering  
National Institute of Technology Karnataka, Surathkal  
Post Srinivasnagar, Mangaluru - 575 025  
Karnataka, India



## ACKNOWLEDGEMENTS

First and foremost, I am deeply indebted to my supervisor, Dr. Shashi Bhushan Arya, Assistant Professor, Department of Metallurgical and Materials Engineering, NITK, Surathkal for his valuable advice, motivation and continuous support throughout the research period. His support during the challenging times was extremely benevolent.

I would like to extend my deepest gratitude to the members of the Research Progress Assessment Committee, Dr. Bhibuti Das (Associate Professor, Department of Civil Engineering) and Dr. Jagannatha Nayak, (Professor, Department of Metallurgical and Materials Engineering) for their insightful comments and suggestions in the course of the work.

I wish to extend my profound appreciation to former HODs, Prof. Udaya Bhat K, Dr. Anandhan Sreenivasan, Prof. Narayan Prabhu and current HOD, Dr. Ravishankar K S for availing the academic support throughout the years.

I am much obliged to Dr. Satish Tailor, Metallizing Equipment Co. Pvt. Ltd, Jodhpur, India for offering the thermal spray coating facilities required. The Department of Mechanical Engineering, Ramaiah Institute of Technology, Bangalore is greatly acknowledged for availing the erosion test facilities. Dr. C.P Paul, (Head, Laser Additive Manufacturing, RRCAT) is deeply acknowledged for providing the laser treatment facilities required for the work. I am really thankful to Dr. D Satish Kumar, JSW Steels, Bellari for his support offered for the work.

This endeavour would not have been possible without the analytical facility support from the Central Research Facility, NITK. The help received from the technical operators Mrs. Aniz, Mr. Akash, Mr. Sanath, Mr. Pradeep and Mrs. Pratheeksha is deeply appreciated. I would like to thank the non-teaching staff of the Metallurgical and Materials Engineering Department for their valuable help during the research work.

And I am indeed pleased with the encouragement and support received from my fellow seniors and colleagues Ajmal, Vinay, Ankush, Silajit, Kunal, Rahul, and Shyam.

My friends Sachin, Niyas, Sudhish, Alvin and Liben are greatly appreciated for backing me at difficult times. It is with a great and profound sense of gratitude, I thank my wife Dr. Stiniya, my parents and family for their continuous encouragement for the completion of the work.

All the praise is to God.



**Dedicated to my beloved wife and parents**



## Table of Contents

Abstract.....	i
List of Figures .....	i
List of Tables .....	ix
List of Abbreviations .....	i
1 Introduction.....	1
1.1 Outline of the thesis.....	3
2 Literature Survey .....	1
2.1 Components of a TBC system.....	1
2.1.1 Substrate.....	1
2.1.2 Bond Coat .....	3
2.1.3 Top Coat.....	5
2.1.4 Thermally grown oxide.....	7
2.2 Thermal spray methods .....	8
2.3 Major failure mechanisms in thermal barrier coatings.....	12
2.3.1 Oxidation behavior of various thermal barrier coatings .....	12
2.3.2 Hot corrosion behavior of various thermal barrier coatings .....	15
2.3.3 Erosion behavior of various thermal barrier coatings.....	20
2.4 Surface modification of coatings.....	22
2.4.1 Laser modification .....	22
2.5 Summary of literature and importance of the present study .....	24
2.6 Objectives of the study.....	26
3 Materials and Methods.....	27
3.1 Preparation of coating feedstock .....	27
3.2 Laser modification of samples .....	30

3.3	Characterization of coatings.....	31
3.3.1	Density and porosity measurements .....	31
3.3.2	Electrochemical Impedance Spectroscopy measurements.....	31
3.4	High-temperature isothermal oxidation tests .....	32
3.5	Hot corrosion tests.....	32
3.6	Erosion tests .....	33
	Results and Discussion .....	37
4	Coating development and characterization of as-coated samples.....	37
4.1	Feedstock materials .....	37
4.1.1	Samarium strontium aluminate .....	37
4.1.2	Alumina powder.....	39
4.1.3	Composite powder mixture.....	41
4.2	As-coated TBC sample.....	42
4.2.1	EBSD analysis of developed coatings .....	47
4.2.2	Mechanical properties of as-coated samples.....	48
5	Oxidation, hot corrosion, and erosion behavior of as-coated samples .....	49
5.1	Isothermal oxidation behavior of as-coated samples .....	49
5.1.1	Surface examination of oxidized samples.....	49
5.1.2	Cross-section analysis and TGO growth.....	52
5.1.3	Kinetics of oxidation.....	57
5.1.4	Electrochemical Impedance Spectroscopy (EIS) analysis of as-coated samples .....	59
5.2	Hot corrosion behavior of as-coated samples .....	61
5.2.1	Hot corrosion of as-coated samples in 50 % wt. Na <sub>2</sub> SO <sub>4</sub> + 50 % wt. V <sub>2</sub> O <sub>5</sub> at 700 °C and 900 °C .....	63

5.2.2	Hot corrosion of as-coated samples in 90 %wt. Na <sub>2</sub> SO <sub>4</sub> + 5 %wt. V <sub>2</sub> O <sub>5</sub> + 5 wt.% NaCl at 700 °C and 900 °C.....	69
5.2.3	Overview of corrosion interactions.....	73
5.3	Solid particle erosion behavior of as-coated samples .....	77
5.3.1	Macroscopic observation of eroded samples .....	77
5.3.2	Cumulative erosion mass loss.....	79
5.3.3	Average erosion values .....	80
5.3.4	Influence of microstructural and mechanical features on erosion behavior .....	82
5.3.5	Erosion mechanism.....	84
5.4	Summary of test results of as-coated sample .....	89
6	Characterization of laser-treated samples .....	91
6.1	EBSD analysis of laser-treated samples.....	97
6.2	Mechanical properties of laser-treated samples .....	98
6.3	Summary .....	99
7	Oxidation, hot corrosion and erosion behavior of laser-treated samples.....	101
7.1	Isothermal oxidation behavior of laser-treated samples.....	101
7.1.1	Cross-sectional analysis and TGO formation .....	103
7.1.2	Kinetics of oxidation of laser-treated samples.....	105
7.1.3	Electrochemical Impedance Spectroscopy (EIS) analysis of laser-treated samples.....	108
7.2	Hot corrosion behavior of laser-treated samples.....	111
7.2.1	Hot corrosion of laser-treated samples in 50 %wt. Na <sub>2</sub> SO <sub>4</sub> + 50 %wt. V <sub>2</sub> O <sub>5</sub> at 700 °C and 900 °C.....	112
7.2.2	Hot corrosion of laser-treated samples in 90 %wt. Na <sub>2</sub> SO <sub>4</sub> + 5 %wt. V <sub>2</sub> O <sub>5</sub> + 5 wt.% NaCl at 700 °C and 900 °C.....	116
7.3	Solid particle erosion behavior of laser-treated samples.....	121

7.3.1	Macroscopic observation of eroded samples .....	121
7.3.2	Cumulative erosion mass loss and average erosion values.....	122
7.3.3	Microstructural changes and erosion response of laser-treated samples .....	124
7.4	Summary of test results of laser-treated sample.....	130
8	Conclusion .....	131
8.1	Scope for future works .....	132
	References.....	135

## Abstract

Composite thermal barrier coatings with top coat composition 70 wt. %  $\text{Al}_2\text{O}_3$  - 30 wt. %  $\text{Sm}_2\text{SrAl}_2\text{O}_7$  was prepared through atmospheric plasma spraying. The rare earth material  $\text{Sm}_2\text{SrAl}_2\text{O}_7$  was synthesized in the laboratory through molten salt technique at 1100 °C. Commercially available NiCrAlY powder was used as bond coat. The as-coated sample is characterized by XRD, SEM, EBSD and Raman spectroscopy. The top coat exhibited three phases  $\text{Sm}_2\text{SrAl}_2\text{O}_7$ ,  $\gamma\text{-Al}_2\text{O}_3$ , and  $\alpha\text{-Al}_2\text{O}_3$ . The high temperature oxidation, hot corrosion and erosion tests were performed to examine the integrity of the coatings in critical conditions. Further, the surface of the coatings were modified with a laser beam to reduce the roughness and to seal the open porosities.

The isothermal oxidation tests at 1100 °C for 150 h showed a parabolic weight gain and a nearly uniform  $\text{Al}_2\text{O}_3$  layer formation at interface. The laser-treated samples showed a comparatively lower parabolic rate constant ( $k_p = 2.2 \text{ mg}^2\text{cm}^{-4}\text{s}^{-1}$ ) than the as-coated samples ( $k_p = 2.5 \text{ mg}^2\text{cm}^{-4}\text{s}^{-1}$ ). Dissociation of top coat was observed from the XRD analysis of oxidized surface. The electrochemical impedance spectroscopy of the laser-treated samples revealed a higher impedance than the as-coated samples due to eliminated porosity. The hot corrosion resistance of the samples at 700 °C and 900 °C were analyzed in aviation and marine conditions employing the salt combinations 50 % wt.  $\text{Na}_2\text{SO}_4$  + 50 % wt.  $\text{V}_2\text{O}_5$  and 90 % wt.  $\text{Na}_2\text{SO}_4$  + 5 % wt.  $\text{V}_2\text{O}_5$  + 5 % wt.  $\text{NaCl}$ , respectively. The samples manifested a lower resistance in marine conditions than aviation conditions, while the laser-treated samples showed a better hot corrosion resistance than the as-coated samples. The solid particle erosion tests using alumina erodent was carried out on the composite coatings at 200 °C and 800 °C. A mixed mode of failure with brittle and ductile material removal mechanisms was observed in the eroded areas. The weight monitoring calculated a higher average erosion value for the as-coated samples exposed to 800 °C at a 90° impact angle. Overall, the laser-treated samples showed a better performance at high temperatures due to the better mechanical properties and sealing of the porosities generated due to the coating process.

**Keywords:** Thermal barrier coatings, surface modifications, isothermal oxidation, hot corrosion, solid particle erosion, electrochemical impedance spectroscopy





## List of Figures

Figure 1.1 Oxidation in gas turbine high pressure compressor blade surface (GE) .....	2
Figure 1.2 Corrosive deposits on compressor blade (Aust and Pons, 2019) .....	2
Figure 1.3 Erosion on leading edge of a turbine fan blade (Alqallaf et al. 2020).....	3
Figure 2.1 Basic architecture of a thermal barrier coating.....	1
Figure 2.2 The cross section of interior of a jet engine showing the hot section parts (Guardian Graphics).....	2
Figure 2.3 Oxidation and corrosion resistance of various bond coats (Strang, 2000) ...	4
Figure 2.4 Performance variation of ZrO <sub>2</sub> with different composition of Y <sub>2</sub> O <sub>3</sub> (Stecura, 1985) .....	5
Figure 2.5 Thermal expansion coefficients of different rare earth aluminates (Feng et al., 2012) .....	6
Figure 2.6 TGO formed at interface of a YSZ top coat and NiCrAlY bond coat (Saremi et al., 2008) .....	8
Figure 2.7 Classification of various thermal spray processes by temperature and particle velocity (Kuroda et al., 2008) .....	9
Figure 2.8 a) Schematic of APS process and b) microstructure developed through APS (Wang et al., 2015).....	10
Figure 2.9 a) Schematic of HVOF process and b) microstructure developed through HVOF (Eskandarany, 2020) .....	10
Figure 2.10 Major failure modes in TBCs .....	12
Figure 2.11 The hot corrosion attack on a turbine blade (Eliaz et al.,2002).....	16
Figure 2.12 Photograph showing erosion in a turbine blade (Naib, 2016) .....	20
Figure 2.13 Schematic of densification of top coat by laser- treatment in a YSZ-Lanthanum hexa-aluminate gradient coating (Khan et al., 2021).....	23
Figure 2.14 Laser glazed YSZ thermal barrier coating with a top densified layer (Tsai et al., 2007) .....	23
Figure 3.1 Flowchart of Sm <sub>2</sub> SrAl <sub>2</sub> O <sub>7</sub> synthesis .....	27
Figure 3.2 Photographic image of synthesized SSA powder.....	28
Figure 3.3 Schematic of the plasma spray setup.....	29

Figure 3.4 Equipment used for laser treatment of developed samples .....	30
Figure 3.5 Photographic images showing a) developed samples for hot corrosion.....	33
Figure 3.6 Schematic diagram of the erosion testing facility .....	34
Figure 3.7 a) Air jet erosion tester, b) sample holder and c) heating setup employed for high temperature erosion testing.....	35
Figure 4.1 The morphology of synthesized SSA powder in a) low and b) high magnifications.....	38
Figure 4.2 XRD pattern of the SSA powder synthesized at 1100 °C for 24 h in controlled atmosphere furnace .....	38
Figure 4.3 Crystal structure of samarium strontium aluminate powder developed from VESTA software.....	39
Figure 4.4 Morphology of alumina powder used in composite top coat .....	40
Figure 4.5 XRD spectrum of alumina powder used for composite top coat.....	40
Figure 4.6 Crystal structure of alumina powder developed from VESTA software ...	41
Figure 4.7 a) SEM image of the composite mixture b), c) EDS analysis of SSA and alumina particle in the composite mixture respectively .....	42
Figure 4.8 The surface of as-coated specimen viewed in SEM at different magnifications a) 500 X b) 1000 X c) 2000 X d) 5000 X .....	43
Figure 4.9 Cross-section of the developed TBC observed under SEM.....	44
Figure 4.10 Elemental mapping of as-coated surface.....	44
Figure 4.11 Surface roughness profile and profilometric image of as-coated sample.	45
Figure 4.12 XRD pattern of the as-coated composite sample surface.....	46
Figure 4.13 a) Phase map and b) grain size distribution of as-coated samples .....	47
Figure 4.14 Inverse pole figure of as-coated samples.....	48
Figure 4.15 Load displacement curves for as-coated samples measure by nanoindentation.....	48
Figure 5.1 Surface image of as-coated samples after isothermal oxidation at 1100 °C for 150h.....	49
Figure 5.2 Magnified surface image of as-coated samples after oxidation test at 1100 °C for 150 h.....	50
Figure 5.3 EDS analysis of the surface after exposure at 1100 °C for 150 h .....	50

Figure 5.4 XRD patterns of as-coated samples after oxidation for different durations .....	52
Figure 5.5 a) Cross-section of developed coatings exposed to 30 h oxidation at 1100 °C, b) EDS mapping of TGO region.....	53
Figure 5.6 a) Cross-section of developed coatings exposed to 90 h oxidation at 1100 °C, b) EDS mapping of TGO region.....	53
Figure 5.7 a) Cross-section of developed coatings exposed to 150 h oxidation at 1100 °C, b) EDS mapping of TGO region.....	54
Figure 5.8 a) High magnification view of lump formation at interface of as-coated sample after oxidation tests b) EDS analysis of lump .....	56
Figure 5.9 Weight gain per unit area of as-coated samples exposed to oxidation test at 1100 °C for different durations .....	58
Figure 5.10 Square of weight gain per area of as-coated samples exposed to oxidation test at 1100 °C for different durations.....	59
Figure 5.11 EIS Nyquist plot of as-coated samples .....	60
Figure 5.12 Graph showing the resistance of as-coated samples in the exposed conditions.....	61
Figure 5.13 Photographs of as-coated samples after hot corrosion in various conditions .....	62
Figure 5.14 XRD pattern of as-coated sample exposed to 50 %wt Na <sub>2</sub> SO <sub>4</sub> + 50 %wt V <sub>2</sub> O <sub>5</sub> at 700 °C .....	64
Figure 5.15 The SEM morphology of failed samples exposed to 50 %wt Na <sub>2</sub> SO <sub>4</sub> + 50 %wt V <sub>2</sub> O <sub>5</sub> at 700 °C showing .....	65
Figure 5.16 XRD pattern of sample exposed to 50 %wt Na <sub>2</sub> SO <sub>4</sub> + 50 %wt V <sub>2</sub> O <sub>5</sub> at 900 °C .....	66
Figure 5.17 The SEM morphology of failed samples exposed to 50 %wt Na <sub>2</sub> SO <sub>4</sub> + 50 %wt V <sub>2</sub> O <sub>5</sub> at 900 °C showing .....	67
Figure 5.18 Raman spectrum of as-coated samples after hot corrosion tests at 50 % wt Na <sub>2</sub> SO <sub>4</sub> + 50 %wt V <sub>2</sub> O <sub>5</sub> at 700 °C and 900 °C.....	69
Figure 5.19 XRD pattern of sample exposed to 90 % wt Na <sub>2</sub> SO <sub>4</sub> + 5 %wt V <sub>2</sub> O <sub>5</sub> + 5 %wt NaCl at 700 °C.....	70

Figure 5.20 The SEM morphology of failed samples exposed to 90 % wt Na <sub>2</sub> SO <sub>4</sub> + 5 % wt V <sub>2</sub> O <sub>5</sub> + 5 % wt NaCl at 700 °C showing .....	70
Figure 5.21 XRD pattern of sample exposed to 90 % wt Na <sub>2</sub> SO <sub>4</sub> + 5 % wt V <sub>2</sub> O <sub>5</sub> + 5 % wt NaCl at 900 °C .....	71
Figure 5.22 The SEM morphology of failed samples exposed to 90 % wt Na <sub>2</sub> SO <sub>4</sub> + 5 % wt V <sub>2</sub> O <sub>5</sub> + 5 % wt NaCl at 900 °C showing .....	72
Figure 5.23 Raman spectrum of as-coated samples after hot corrosion tests at 90 % wt Na <sub>2</sub> SO <sub>4</sub> + 5 % wt V <sub>2</sub> O <sub>5</sub> + 5 % wt NaCl at 700 °C and 900 °C .....	73
Figure 5.24 Photographic images of as-coated samples exposed to erosion under various conditions .....	78
Figure 5.25 Graph showing cumulative mass loss of coating vs cumulative mass of erodents for as-coated samples subjected to various erosion conditions .....	80
Figure 5.26 Plots showing a) steady state erosion rate and b) average erosion values of as-coated samples at different conditions .....	80
Figure 5.27 SEM image of the erodents used .....	82
Figure 5.28 a) XRD patterns of scars of samples eroded at various conditions b) EDS composition of scar of samples exposed at 800 °C and c) 200 °C at 90° angle d) Nominal weight percentages observed in scars .....	84
Figure 5.29 Profilometric images of erosion scars in as-coated samples subjected to erosion at different conditions .....	85
Figure 5.30 High magnification SEM images of as-coated samples exposed to various erosion conditions .....	86
Figure 5.31 Schematic diagram of erosion mechanisms observed in the developed coating .....	87
Figure 6.1 Image showing the burning marks on coating surface on exposure to laser beam with various power levels .....	91
Figure 6.2 a) SEM image showing localized burning marks on samples treated with 60 W laser power, b) The high magnification view of the burned regions .....	92
Figure 6.3 Photograph of the as-coated and laser modified samples .....	92
Figure 6.4 The surface of laser-treated specimen observed in SEM at different magnifications a) 500 X b) 1000 X .....	93
Figure 6.5 Elemental mapping of laser coated sample surface .....	94

Figure 6.6 a) Surface roughness profile and b) profilometric image of laser-treated sample surface.....	94
Figure 6.7 Surface XRD pattern of the laser-treated samples .....	95
Figure 6.8 Normalized XRD patterns of as-coated and laser-treated sample surfaces	96
Figure 6.9 a) Phase map and b) grain size distribution of laser-treated samples.....	98
Figure 6.10 Inverse pole figure of laser-treated samples.....	98
Figure 6.11 Load displacement curves for laser-treated samples measure by nanoindentation.....	99
Figure 7.1 Surface image of laser-treated samples after isothermal oxidation at 1100 °C for 150 h.....	101
Figure 7.2 Magnified surface image of laser-treated samples after isothermal oxidation test at 1100 °C for 150 h .....	102
Figure 7.3 XRD patterns of laser modified samples after oxidation for different durations.....	103
Figure 7.4 a) Cross-section of laser-treated coatings exposed to 30 h oxidation at 1100 °C b) EDS mapping of TGO region.....	104
Figure 7.5 a) Cross-section of laser-treated coatings exposed to 90 h oxidation at 1100 °C b) EDS mapping of TGO region.....	104
Figure 7.6 a) Cross-section of laser-treated coatings exposed to 150 h oxidation at 1100 °C b) EDS mapping of TGO region.....	105
Figure 7.7 a) Weight gain per unit area of laser-treated samples b) Comparison of weight gain between as-coated and laser-treated samples.....	106
Figure 7.8 Square of weight gain per unit area plotted against time for laser-treated samples.....	107
Figure 7.9 Schematic of oxidation in a) as-coated and b) laser-treated samples.....	107
Figure 7.10 Nyquist plots for the as-coated and laser-treated samples.....	108
Figure 7.11 Hot corrosion resistances of laser-treated samples in different corrosive conditions.....	111
Figure 7.12 Photographs of laser-treated samples after hot corrosion in various conditions.....	112
Figure 7.13 XRD pattern of laser-treated sample exposed to 50 % wt Na <sub>2</sub> SO <sub>4</sub> + 50 % wt V <sub>2</sub> O <sub>5</sub> at 700 °C.....	113

Figure 7.14 The SEM morphology of laser-treated samples exposed to 50 % wt Na <sub>2</sub> SO <sub>4</sub> + 50 % wt V <sub>2</sub> O <sub>5</sub> at 700 °C showing.....	113
Figure 7.15 XRD pattern of laser-treated sample exposed to 50 % wt Na <sub>2</sub> SO <sub>4</sub> + 50 % wt V <sub>2</sub> O <sub>5</sub> at 900 °C.....	114
Figure 7.16 The SEM morphology of laser-treated samples exposed to 50 % wt Na <sub>2</sub> SO <sub>4</sub> + 50 % wt V <sub>2</sub> O <sub>5</sub> at 900 °C showing.....	115
Figure 7.17 Raman spectrum of laser-treated samples after hot corrosion tests at 50 % wt. Na <sub>2</sub> SO <sub>4</sub> + 50 % wt. V <sub>2</sub> O <sub>5</sub> at 700 °C and 900 °C.....	115
Figure 7.18 XRD pattern of laser-treated sample exposed to 90 % wt Na <sub>2</sub> SO <sub>4</sub> + 5 % wt V <sub>2</sub> O <sub>5</sub> + 5 % wt NaCl at 700 °C.....	116
Figure 7.19 The SEM morphology of laser-treated samples exposed to 90 % wt. Na <sub>2</sub> SO <sub>4</sub> + 5 % wt. V <sub>2</sub> O <sub>5</sub> + 5 % wt. NaCl at 700 °C showing.....	117
Figure 7.20 XRD pattern of laser-treated sample exposed to 90 % wt. Na <sub>2</sub> SO <sub>4</sub> + 5 % wt. V <sub>2</sub> O <sub>5</sub> + 5 % wt. NaCl at 900 °C.....	118
Figure 7.21 The SEM morphology of laser-treated samples exposed to 90 % wt. Na <sub>2</sub> SO <sub>4</sub> + 5 % wt. V <sub>2</sub> O <sub>5</sub> + 5 % wt. NaCl at 900 °C showing.....	118
Figure 7.22 Raman spectrum of laser-treated samples after hot corrosion tests at 90 % wt Na <sub>2</sub> SO <sub>4</sub> + 5 % wt V <sub>2</sub> O <sub>5</sub> + 5 % wt NaCl at 700 °C and 900 °C.....	119
Figure 7.23 Photographic images of laser-treated samples exposed to erosion under various conditions .....	121
Figure 7.24 Graph showing cumulative mass loss of coating vs cumulative mass of erodents for laser-treated samples exposed at 200 °C and 800 °C .....	123
Figure 7.25 a) Comparison of cumulative mass loss in as-coated and laser-treated samples b) Initial weight loss of as-coated and laser-treated samples.....	123
Figure 7.26 Plots showing a) average erosion values and b) steady state erosion rate of laser-treated samples at different conditions.....	124
Figure 7.27 XRD patterns of scars in laser-treated samples eroded at various conditions .....	126
Figure 7.28 Profilometric view of eroded areas in laser-treated samples.....	127
Figure 7.29 High magnification SEM images of laser-treated samples exposed to various erosion conditions .....	128

Figure 7.30 Schematic diagram of erosion mechanisms observed in as-coated and laser-treated samples at 800 °C (not in scale).....129





## List of Tables

Table 2.1 Comparison of different thermal spray techniques (Amin et al. 2016) .....	11
Table 2.2 Oxidation behavior of different TBC materials under different atmospheres .....	13
Table 2.3 Hot corrosion behavior of different TBC materials under different corrosive conditions.....	16
Table 2.4 Erosion behavior of different TBC materials under different erosive conditions.....	21
Table 2.5 Effect of laser treatment in different TBC systems .....	23
Table 2.6 Comparison of properties of alumina and SSA .....	25
Table 3.1 Composition (wt.%) of commercially available NiCrAlY powder used for bond coat.....	29
Table 3.2 Composition of Inconel 718 substrate in wt.% .....	29
Table 3.3 Operating parameters used for atmospheric plasma spray coating.....	30
Table 3.4 Parameters used for air jet erosion testing .....	34
Table 4.1 Cross-sectional composition of developed composite coatings (wt.%) .....	45
Table 5.1 Thickness and composition of the TGO region observed in as-coated samples after oxidation .....	54
Table 5.2 Composition of sample cross-section after isothermal oxidation tests for 150 h duration (wt.%) .....	55
Table 5.3 Obtained values of equivalent circuit elements for as-coated samples .....	60
Table 5.4 Details of the corrosive conditions tested.....	62
Table 5.5 Composition of the products formed on as-coated samples exposed to aviation conditions at 700 °C.....	64
Table 5.6 Composition of the products formed on as-coated samples exposed to aviation conditions at 900 °C.....	67
Table 5.7 Composition of the products formed on c samples exposed to marine conditions at 700 °C.....	71
Table 5.8 Composition of the products formed on as-coated samples exposed to marine conditions at 900 °C.....	72

Table 5.9 Scar dimensions of samples exposed to various conditions measured in surface profilometer.....	78
Table 5.10 Mechanical properties of the as-coated samples and similar systems.....	83
Table 6.1 EDS composition of laser-treated surface .....	93
Table 6.2 FWHM values of major peaks in as-coated and laser-treated samples .....	97
Table 7.1 Composition of laser-treated sample surfaces after isothermal oxidation tests .....	102
Table 7.2 Composition of as-coated and laser-treated sample cross-section after isothermal oxidation tests .....	105
Table 7.3 Obtained values of equivalent circuit elements for laser-treated samples.	108
Table 7.4 Composition of the products formed on laser-treated samples exposed to aviation conditions at 700 °C.....	114
Table 7.5 Composition of the products formed on laser-treated samples exposed to aviation conditions at 900 °C.....	115
Table 7.6 Composition of the products formed on laser-treated samples exposed to marine conditions at 700 °C.....	117
Table 7.7 Composition of the products formed on laser-treated samples exposed to marine conditions at 900 °C.....	118
Table 7.8 Scar dimensions of laser-treated samples exposed to various conditions measured in surface profilometer.....	122
Table 7.9 Initial slope of cumulative weight loss plot in as-coated and laser-treated samples.....	124

## List of Abbreviations

APS	Atmospheric Plasma Spray
ASTM	American Society for Testing and Materials
DL	Double-layer
DyZ	Dysprosium Zirconate
EBSD	Electron Backscatter Diffraction
EB-PVD	Electron Beam Physical Vapor Deposition
EDM	Electro-discharge Machining
EDS	Electron Dispersive Spectroscopy
EIS	Electrochemical Impedance Spectroscopy
FE-SEM	Field Emission Scanning Electron Microscopy
GZ	Gadolinium Zirconate
HVOF	High-Velocity Oxy-Fuel Deposition
JCPDS	Joint Committee on Powder Diffraction Standards
LZ	Lanthanum Zirconate
OCP	Open Circuit Potential
SEM	Scanning Electron Microscopy
SL	Single-layer
SSA	Samarium Strontium Aluminate
SLPM	Standard litres per minute
TBCs	Thermal Barrier Coatings
TGO	Thermally Grown Oxide

XRD X-Ray Diffraction

YSZ Yttria Stabilized Zirconia

# 1 Introduction

Gas turbines have dominated the field of propulsion, with better performance and efficiencies at higher operating temperatures. These high-temperature conditions may induce different degradation mechanisms in gas turbine systems. The maintenance of gas turbine engines is very much intricate and often demand the rejection of existing vanes and blades due to component deterioration. The taxonomy of gas turbine failures appends an ‘external and internal surface damage’, which includes oxidation, cracking, and erosion. Thermal Barrier Coatings (TBCs) are employed in gas turbines to improve the life of the components, resisting these failure mechanisms in critical operating conditions (Soares 2008; Aust and Pons 2019). The application of a TBC provides thermal insulation, with a 100 °C – 300 °C reduction in surface temperature of metallic components, thereby reducing cooling requirements and increasing thermal efficiency and durability (Bajpai et al. 2015). The typical design of a TBC comprises three layers; a ceramic top coat, a metallic bond coat, and a superalloy substrate. As these individual layers own different material and thermo-mechanical characteristics, the property mismatch and significant temperature gradients result in stress development and cracking during operation (Saral and Toplan 2009). This makes the design of the TBC system very crucial in the performance and lifetime of the components.

At high temperatures, the TBC is subjected to oxidation, where oxygen penetrates into the top coat by ionic diffusion and gas penetration. The overall oxygen flux depends on the chemistry of the coating, microstructure, and prevailing environments. This oxygen flux leads to the formation of a thermally grown oxide (TGO) at the top coat bond coat interface, which may create stresses in the system depending on the composition and geometry of the TGO formed (Fox and Clyne 2004). As shown in Figure 1.1, oxidation also affects the surface composition of the components, degrading the properties and resulting in spalling of the surface.

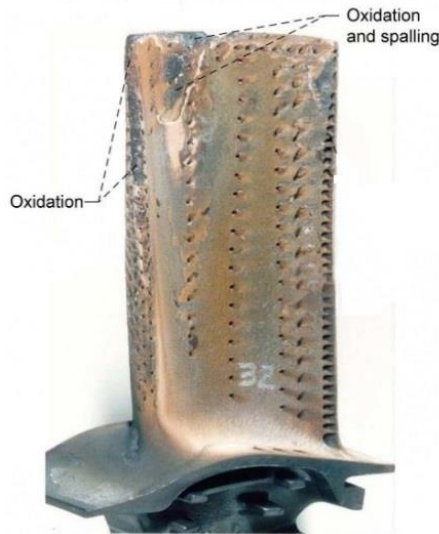


Figure 1.1 Oxidation in gas turbine high pressure compressor blade surface (GE)

The hot corrosion in a gas turbine is the chemical attack of the component surface by corrosive salts such as  $\text{Na}_2\text{SO}_4$ ,  $\text{V}_2\text{O}_5$ , and  $\text{NaCl}$ , emerging from the low-quality fuels used in the system, which gets deposited on the component surface as shown in Figure 1.2. At high temperatures, the low melting corrosives tend to infiltrate the coatings. The conventional TBC systems, such as Ytria Stabilized Zirconia (YSZ) suffer from phase transformations and destabilization in the presence of corrosives. The coatings may present a porous structure with cracks after exposure to hot corrosion conditions. The resistance of a system towards hot corrosion depends on the overall chemistry, reactivity, high-temperature stability, and surface conditions of the coating.



Figure 1.2 Corrosive deposits on compressor blade (Aust and Pons, 2019)

The erosion in a gas turbine is the surficial material removal by the impact of solid particles embedded in the inlet gas stream. Figure 1.3 shows the erosion on the leading edge of a turbine fan blade. The succession of impacts leads to material removal from

the surface, leading to component failure. The resistance against high-temperature erosion depends on the surface properties and mechanical properties of the system. A surface with high hardness is recognized to offer better erosion resistance (Alqallaf et al. 2020; Aust and Pons 2019; Puspitasari et al. 2021).



Figure 1.3 Erosion on leading edge of a turbine fan blade (Alqallaf et al. 2020)

To resist these mechanisms, the material choice of the TBCs is highly significant. New materials are under research, as the conventional material YSZ suffers from phase transformations (from tetragonal to monoclinic phase) at high temperatures. The coating material should possess a low thermal conductivity, high thermal expansion coefficient, and high-temperature stability (Bajpai et al. 2015). In addition to the material properties, the surface conditions are also significant in controlling the life of the coatings under critical conditions. The surface modifications on TBC can have convincing improvements in performance, through re-engineering of the surface. Laser treatment on a surface can produce a fine-grained compact coating with higher density, lower porosity, and improved microstructures.

## 1.1 Outline of the thesis

**Chapter 1** includes a brief introduction to the failure methods of gas turbine components and the application of thermal barrier coatings.

**Chapter 2** incorporates the literature survey of various aspects of thermal barrier coatings. Detailed reviews on components of TBC, the performance of TBC systems in different oxidation, hot corrosion, and erosion environments are included. The importance of surface modifications on TBC behavior is also mentioned.

**Chapter 3** Comprise the details of the materials and methods employed for synthesizing the ceramic powder, coating development, surface modifications, and

various tests on the sample. The particulars of the equipment used and, parameters employed are reported.

**Chapter 4** includes the results of various characterization tests performed on the developed samples. Elaborate reports on morphological and microstructural properties are included.

**Chapter 5** incorporates the oxidation, hot corrosion, and erosion behavior of the as-coated samples. The samples are investigated for the corresponding mechanisms involved in each high-temperature interaction, and the observations are reported.

**Chapter 6** comprehends the results of various characterization tests performed on the laser-treated samples. The differences observed in morphological and microstructural properties between the as-coated and laser-treated samples are discussed in detail.

**Chapter 7** includes the oxidation, hot corrosion, and erosion behavior of the laser-treated samples. The behavior is compared with the as-coated samples and the differences observed are reported.

**Chapter 8** appends the salient conclusions derived from the research work performed. The future scope of the presented work is also mentioned.



## 2 Literature Survey

The thermal barrier coatings are applied on gas turbine components, to increase the overall efficiency and performance at higher operating temperatures. The components suffer from degradation mechanisms at higher temperatures. The primary purpose of TBC is to provide a functional surface with high-temperature stability protecting the underlying components (Daroonparvar et al. 2014; Jonnalagadda et al. 2017).

### 2.1 Components of a TBC system

A typical TBC system comprises a ceramic top coat and a metallic bond coat on a superalloy substrate. The basic architecture of a thermal barrier coating is shown in Figure 2.1.

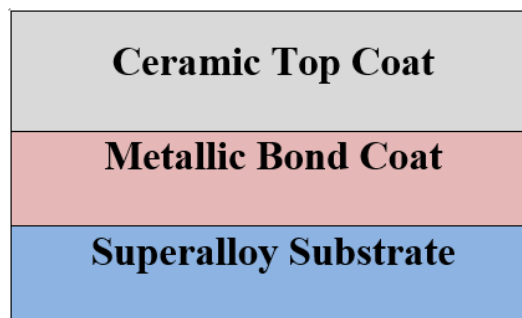


Figure 2.1 Basic architecture of a thermal barrier coating

#### 2.1.1 Substrate

The substrates for thermal barrier coatings are generally Nickel-based superalloys. Superalloys are heat-resistant alloys based on nickel, chromium or iron. The primary use of superalloys includes applications in gas turbines, coal plants, chemical industries, and other special applications demanding corrosion protection. Figure 2.2 shows the cross-section of the interior of a turbine system, depicting the hot section parts exposed to higher temperatures, which are generally made-up of superalloys. The major advantage of superalloys is that an exceptional combination of mechanical properties can be achieved by proper control of microstructure.

Fe-based superalloys are developed from stainless steel with an austenitic matrix of Ni and Fe, with above 25 % Ni, stabilizing the FCC phase. The Co-based superalloys comprise a network of carbides at the grain boundary, strengthening the

alloy even at high temperatures. The overall strength of the Co-based superalloys is lower than Ni-based alloys. They are highly resistant to creep and fatigue and are mostly used in static components where the stress level is lower than in rotating components.

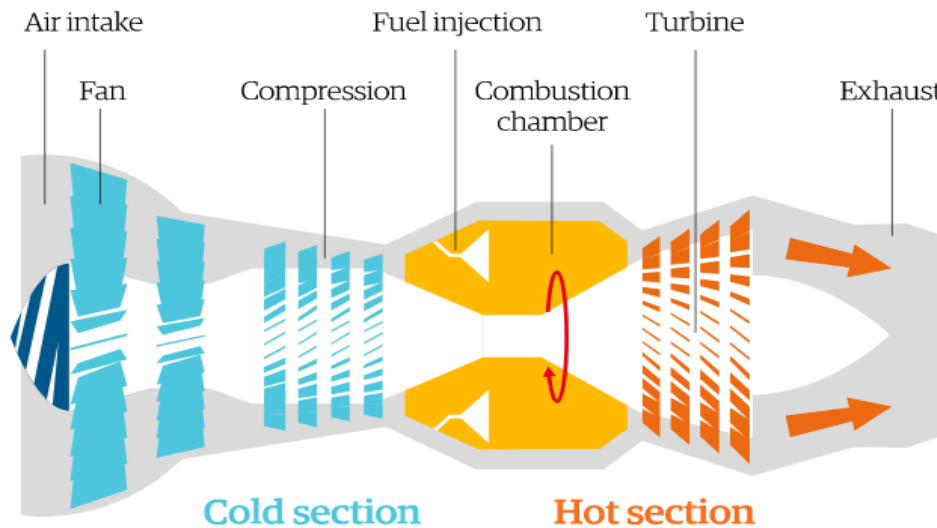


Figure 2.2 The cross section of interior of a jet engine showing the hot section parts (Guardian Graphics)

Ni-based superalloys are the most commonly used superalloys since their discovery in the 1960s because of their high-temperature phase stability, and superior load-bearing capability above 80 % of their melting temperature. The primary Ni-based superalloys are Ni-Cr-Fe based (Inconel 625, 718, 901), Ni-Mo-Fe based (Hastelloy A, B), and Ni-Cr-Mo based (Hastelloy X, C) (Thomas et al. 2006). IN 718 is a precipitation-hardened material with enhanced corrosion resistance, mechanical strength, and weldability, offering high creep strength at high temperatures. The composition contains significantly Fe, Nb, Mo, Ti, and Al. The stability is further enhanced by chromium alloying, while the Nb content enables the formation of NbC aiding the strength of the material (Akca and Gürsel 2015; ASM Aerospace specification Metals Inc. 2014). Inconel 718 strengthened by solid solution strengthening and precipitation hardening with  $\gamma$  and  $\gamma'$  phases offer a higher ultimate strength above 1920 MPa, which is retained at higher temperatures. The precipitation of  $\gamma'$  phase is the prime reason behind strengthening (Cemal et al. 2012; Furrer and

Fecht 1999). The entire purpose of the bond coat and top coat is to isolate the substrate from undesirable high-temperature effects.

### **2.1.2 Bond Coat**

Bond coats are metallic coatings applied on superalloy substrates to protect them from high-temperature corrosion and oxidation. The material must be thermally and structurally stable to avoid any softening or volume changes at high temperatures. The microstructure and chemistry of the bond coat have a significant role in the durability of the thermal barrier coating system. A bond coat with a low oxygen content and high aluminium activity can lead to a pure aluminum oxide formation upon high-temperature oxidation (Narita et al. 2005). The most used bond coat is MCrAlY, where M= Co and/or Ni. Figure 2.3 shows the oxidation and corrosion resistance of various bond coats commonly used. Better oxidation resistance is observed in NiCrAlY coatings, which makes them attractive at elevated temperatures. Generally, the MCrAlY coatings offer a higher oxidation resistance by sound oxide formation and good adhesion to the surface layer (Strang 2000). Researchers suggest an optimal concentration of 5.38 % Cr, 8-13 % Al, and Y 0.5-1 % within the bond coat. Yttrium improves the adhesion of the coatings, particularly with the oxide layer formed after oxidation. Ni content enables the formation of high-temperature phases Ni<sub>3</sub>Al and NiAl (Moskal 2009).

The NiCoCrAlY bond coat has shown exceptional oxidation and corrosion resistance than the NiCrAlY bond coat. A degradation mechanism in the case of CoCrAlY is the downward diffusion of Al to substrate, followed by Co and Cr movement. A CoCrAlY bond coat with 40 µm thickness exposed to cyclic oxidation at 1050 °C showed a lifetime of 160 h with the degradation from Al depletion. The high-temperature oxidation resistance of CoCrAlY is inferior to that of NiCrAlY. In addition, when used with Ni-based superalloys, the least chemical gradient between NiCrAlY and substrate, decelerates the diffusion effects (Han et al. 2018).

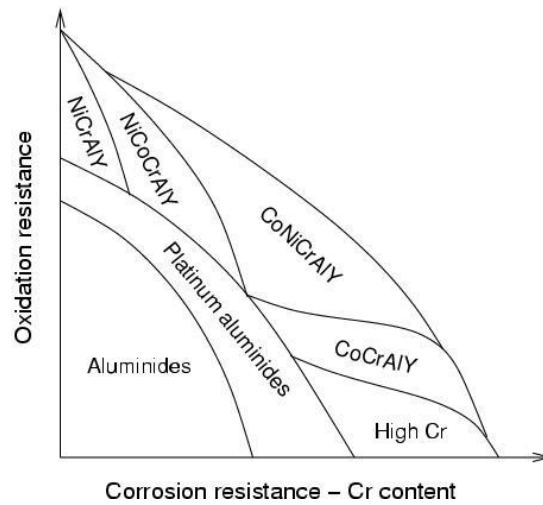


Figure 2.3 Oxidation and corrosion resistance of various bond coats (Strang, 2000)

Besides MCrAlY coatings, diffusion coatings of nickel aluminide ( $\beta$ -NiAl) and platinum aluminide are also used. These act as aluminium reservoirs promoting stable  $\alpha$ -Al<sub>2</sub>O<sub>3</sub> formation. Also, the stability of the  $\beta$ -NiAl phase is spread over a wide range of compositions, which enables the retention of phases even in the case of aluminium consumption. Platinum addition increases the oxidation resistance of the bond coat and promotes selective oxidation of aluminium, but slightly reduces the adhesion of the oxide film formed (Li et al. 2014).

The significance of diffusion barrier coatings is in creating an intermediate hindrance to Al diffusion and substrate element diffusion. Diffusion barrier bond coats with composition Re-Cr-Ni and Ni-aluminides applied on TMS 82+ and Hastelloy X were studied by Narita et al.. The bond coats were stable up to 1150 °C and prevents the inward diffusion of aluminium and outward diffusion of substrate elements. The TBC systems with these bond coats showed very little exfoliation of oxide scales, while the coatings without bond coats showed severe exfoliation. The material was found to be suitable for Ni-based, Fe-based and Co-based superalloys (Moskal 2009; Narita et al. 2005). A RuAl system with a 50:50 atomic percentage as a bond coat was found to be resistant to oxidation and forms a compact and uniform  $\alpha$ -Al<sub>2</sub>O<sub>3</sub> TGO, which offer a better life to components (Soare et al. 2017).

Different modifications on bond coats have been studied by various researchers. A combination of NiAl and CoCrAlY has been proved to have a better performance.

AlN dispersion reduced the thermal expansion coefficient, increased the mechanical strength, and further enhanced the life of the system (Mohan G Hebsur 2002).

### 2.1.3 Top Coat

The initial top coats used for thermal insulation were flame sprayed zirconia-calcia coatings. The zirconia-based coatings tend to destabilize upon exposure to high temperatures. Later,  $ZrO_2$ - $Y_2O_3$  ceramic applied on NiCrAlY bond coat was used by National Aeronautics and Space Administration (NASA) Lewis research center, where the yttria stabilizes the zirconia. From the different weight percentages of  $Y_2O_3$  addition varying from 12-20 %, Stecura (1985) proved that a 6-8 %  $Y_2O_3$  produces better results in thermal cycling as shown in Figure 2.4 (Stecura 1985; Miller 1997).

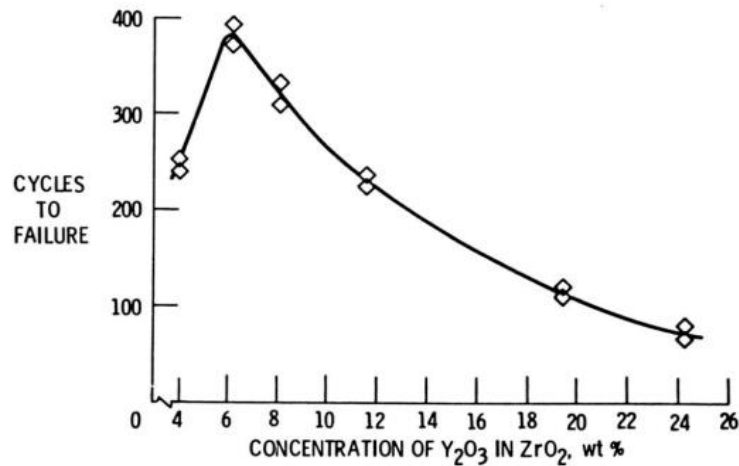


Figure 2.4 Performance variation of  $ZrO_2$  with different composition of  $Y_2O_3$  (Stecura, 1985)

The conventionally used YSZ displays a high thermal expansion coefficient of about  $11 \times 10^{-6} K^{-1}$  at  $1000^\circ C$ , and a low thermal conductivity of  $0.8-1.7 Wm^{-1}K^{-1}$ . The disadvantage with the YSZ coatings is the phase transformation from tetragonal to monoclinic, and the associated volume changes which lead to spallation, at temperatures around  $1200^\circ C$ .  $Al_2O_3$  is another favored TBC candidate due to the moderate thermal conductivity of about  $5.8 Wm^{-1}K^{-1}$  and high thermal expansion coefficient of  $9.6 K^{-1}$ . A higher thermal expansion coefficient always prevents spallation from expansion mismatch issues while employed with metallic systems. A higher density, lower oxygen permeability, and inertness towards chemical reactions

make alumina a promising TBC material. Despite all these factors, on high-temperature exposure, alumina tends to undergo phase transformations from  $\gamma$ - $\text{Al}_2\text{O}_3$  or  $\theta$ - $\text{Al}_2\text{O}_3$  to the  $\alpha$ - $\text{Al}_2\text{O}_3$  phase, which creates volumetric changes and subsequent spallation. This restrains the usage of alumina as a single-layer top coat material at high-temperature applications. The incorporation of alumina with YSZ has gained attraction in view of the better oxidation resistance offered. The presence of alumina supports in delaying the phase transformations in YSZ (Avcı et al. 2020; Zhu et al. 2012).

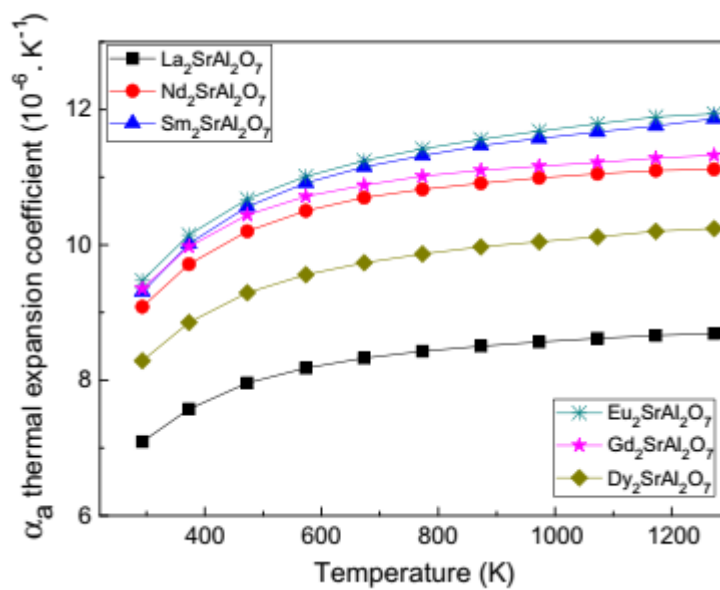


Figure 2.5 Thermal expansion coefficients of different rare earth aluminates (Feng et al., 2012)

The rare-earth zirconates ( $\text{REZr}_2\text{O}_7$ ) with pyrochlore structure are stable at high temperatures. In addition, they offer a low thermal conductivity than the conventional YSZ. But, the lower thermal expansion results in the development of stress during operation, leading to cracking and failure (Patnaik n.d.). Recent researchers have identified the Lanthanides/RE strontium aluminates ( $\text{Ln}_2\text{SrAl}_2\text{O}_7$ ) with a tetragonal structure and high-temperature stability to be used as a top coat. The material is very weakly anisotropic with quite low directional dependence. The single-layer  $\text{Sm}_2\text{SrAl}_2\text{O}_7$  coatings have shown satisfactory performance in oxidation conditions at 1100 °C and hot corrosion resistance towards vanadate and sulphate salts (Baskaran and Arya 2017; Feng et al. 2012). The  $\text{Sm}_2\text{SrAl}_2\text{O}_7$  offers a higher thermal expansion

coefficient of  $10\text{-}12 \times 10^{-6} \text{ K}^{-1}$  at high temperatures (Figure 2.5), which makes it compatible with alumina and other metallic coating systems.

#### **2.1.4 Thermally grown oxide**

The TGO is a reaction product formed within the TBC system, at the top coat bond coat interface, upon continuous exposure at elevated temperatures. The oxygen penetrating through the top coat interacts with the bond coat elements or elements present at the interface, resulting in oxide layer formation. In many thermal barrier coating systems, an initial exposure time will result in  $\text{Al}_2\text{O}_3$  TGO, while prolonged exposure leads to the formation of other oxides such as  $\text{Cr}_2\text{O}_3$ ,  $\text{NiO}$ , and spinel oxides such as  $\text{Ni}(\text{CrAl})_2\text{O}_4$ . The reactivity and abundance of Al at the interface is the primary driving force for  $\text{Al}_2\text{O}_3$  formation. The diffusion of substrate elements to the interface may contribute to spinel formation.

Out of the different oxides formed, better stability and adherence make  $\text{Al}_2\text{O}_3$  the most preferred TGO. An  $\text{Al}_2\text{O}_3$  TGO delays/prevents further reactions or spinel formations, depending on other properties of the coating. The least standard free energy of formation also favors the  $\text{Al}_2\text{O}_3$  formation thermodynamically. The TGO growth is a complex phenomenon generally reflecting a mass gain upon thermal exposure. The TGO growth attains different kinetics which can be described by a power law, parabolic law, etc depending on coating characteristics and prevailing environments. The oxygen ingress through the interconnected pores and cracks and ionic movement determines the extent of different oxide formations. The bond coat must act as a reservoir to supply Al to react with O, as a depletion in Al accelerates other undesired oxide formations. Figure 2.6 shows the TGO formation in a YSZ top coat and NiCrAlY bond coat system, where a uniform oxide layer is formed. Few researchers report that the  $\text{Al}_2\text{O}_3$  content at the interface rarely increases after 50 h, while increments in alumina TGO till 200 h is also reported (Saremi et al. 2008; Daroonparvar et al. 2013; Liu et al. 2016). The variations reported emphasize the fact that the TGO kinetics depends on multiple factors, including material and environmental variables. Despite the protection it offers, a thicker TGO creates a higher stress than a thin TGO. The stresses increase five-fold when the thickness includes spinel oxides. Overall, the thickness, geometry, and

composition of the TGO are significant in determining the durability of thermal barrier coatings.

The overall behavior of any top coat material depends on the microstructure, which in turn depends on the deposition technique employed. Different thermal spray methods are currently practiced for the development of TBCs.

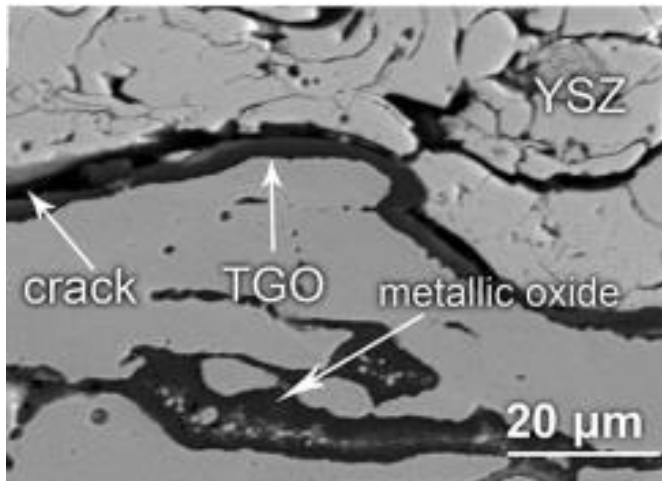


Figure 2.6 TGO formed at interface of a YSZ top coat and NiCrAlY bond coat (Saremi et al., 2008)

## 2.2 Thermal spray methods

Thermal spraying generally refers to coating methods where the feedstock is melted/heated and sprayed to the target surface. The resultant molten or semi-molten droplets are sprayed on to the substrate. Flame spraying is the first thermal spray process invented by M U Schoop. (Tucker C 1994) A wide variety of materials including metals, ceramics, polymers, etc can be sprayed using thermal spraying. The major thermal spray methods used include flame spraying, wire spraying, high-velocity oxyfuel (HVOF), and plasma spraying. Figure 2.7 shows the classification of various thermal spray processes by temperature and particle velocity (Kuroda et al. 2008).



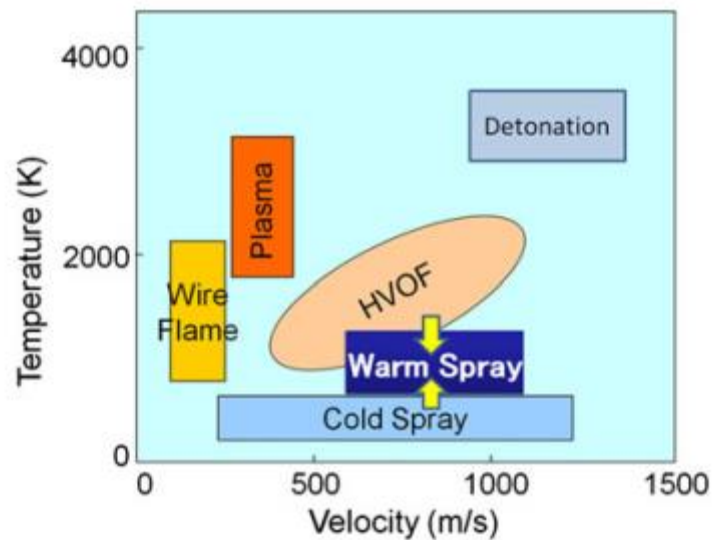


Figure 2.7 Classification of various thermal spray processes by temperature and particle velocity (Kuroda et al., 2008)

### ***Plasma Spraying***

A high-energy electric arc is generated between two electrodes, which ionizes the gas and creates a high-pressure plasma. The higher temperature created, increases the gas volume, increasing the pressure and velocity of the exit gas stream. Argon is the most preferred gas, because of its high inertness. The major operating parameters of plasma spraying include electric power, metered powder feed, gas flow rates, stand-off distances, etc. The plasma-sprayed coatings achieve a better bond strength and oxide-free dense structure when employed with vacuum spray systems (Dorfman 2012; Tucker C 1994). The schematic of the process and the general lamellar microstructure in a plasma sprayed coating is shown in Figure 2.8.

### ***HVOF***

In HVOF, a gaseous fuel is mixed with oxygen, and the combustion products are expanded through a nozzle. The stream exits with supersonic velocity. The powder particles are introduced into the stream within the nozzle, which achieves a very high velocity in the stream. The heated-up particles are accelerated to impinge on the substrate at a high velocity to form a compact layer. (Kuroda et al. 2008). The resultant

surface may have unmolten particles if the larger powder particles do not achieve sufficient temperature upon flight. The schematic of the process and the general microstructure is shown in Figure 2.9.

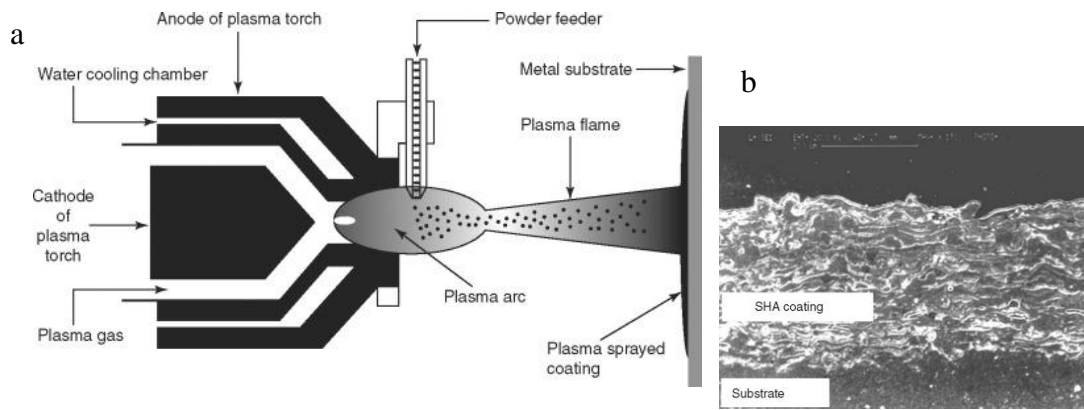


Figure 2.8 a) Schematic of APS process and b) microstructure developed through APS (Wang et al., 2015)

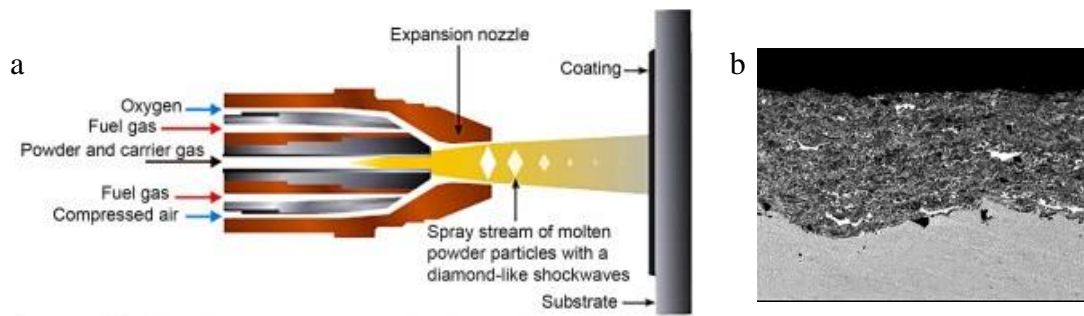


Figure 2.9 a) Schematic of HVOF process and b) microstructure developed through HVOF (Eskandarany, 2020)

### ***Cold spray***

Cold spraying is another solid-state coating technique, which depends on the kinetic energy of particles in a supersonic particulate stream, rather than the heat energy. The heating of gas in a cold spray is to generate the sonic velocity in a convergent-divergent nozzle. As the expansion of the gas in the divergent nozzle creates a cooling, the exit gas stream will be of lower temperature with high velocity. The very high velocity in the cold spray process produces a dense, oxide-free microstructure with induced compressive stresses (Eskandarany 2020; Smith 2007).

### ***Electron Beam Physical Vapor Deposition (EB-PVD)***

The EB-PVD technique produces columnar structured top coat with columns aligned perpendicular to the substrate. The inter-columnar gap provides sufficient strain tolerance and reduction in thermal conductivity. But these gaps may entertain oxygen penetration at elevated temperatures. The EB-PVD coatings are well known for their resistance to cyclic fatigue at elevated temperatures (Chen and Dong 2015).

The properties of the developed coatings depend greatly on the techniques and parameters employed. A comparison of different thermal spray processes, as in Table 2.1 shows that the highest flame temperature is in the case of plasma spray, while the HVOF technique produces coatings with the least porosity and high adhesion (Amin and Panchal 2016). Wire arc and wire flame spray methods are comparatively inferior to other techniques concerning the quality of coatings and temperature produced.

Table 2.1 Comparison of different thermal spray techniques (Amin et al. 2016)

<b>Process</b>	<b>Heat Source</b>	<b>Flame temperature °C</b>	<b>Gas velocity m/s</b>	<b>Porosity %</b>	<b>Adhesion MPa</b>
Plasma spraying	Plasma flame	12000-16000	500-600	2-5	40-70
Wire arc spray	Electric arc	5000-6000	<300	5-10	28-41
Wire flame spray	Oxy-fuel combustion	3000	<300	5-10	14-21
HVOF	Oxy-gas fuel combustion	3200	1200	1-2	>70

## 2.3 Major failure mechanisms in thermal barrier coatings

The field of thermal barrier coatings has seen a larger extent of research and resultant progress in performance. The major mechanisms reported to cause component failure are high-temperature oxidation, hot corrosion, and solid particle erosion, as illustrated in Figure 2.10. The response of the coating and failure in each case depends on the environment, material composition, and other surface conditions prevailing.

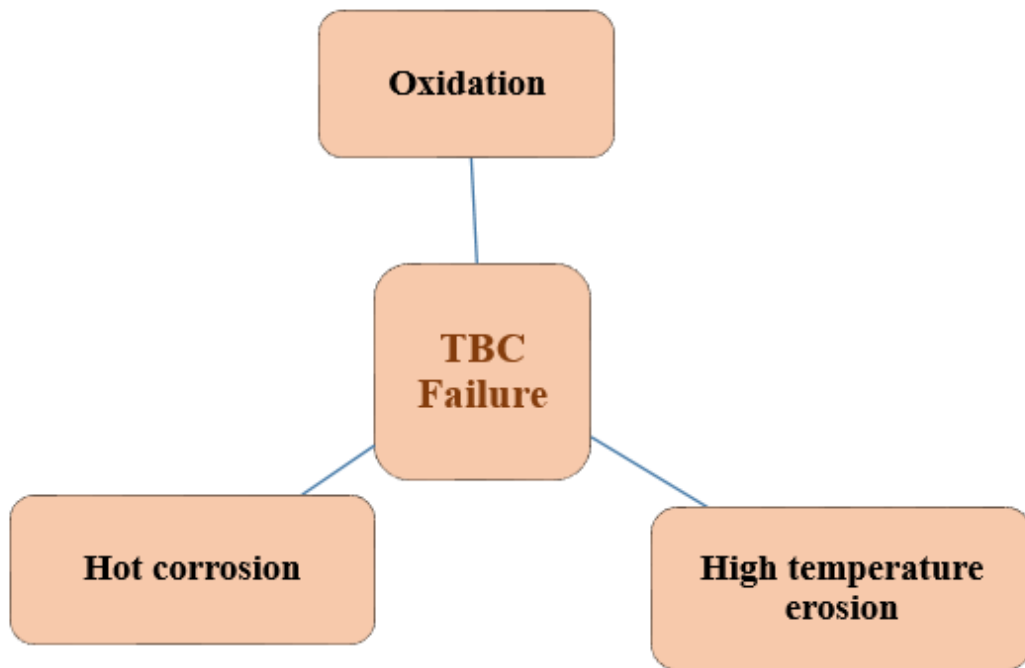


Figure 2.10 Major failure modes in TBCs

### 2.3.1 Oxidation behavior of various thermal barrier coatings

The ionic conduction of the top coat and the interconnected pores and cracks leads to the diffusion of oxygen through the top coat and subsequent oxidation. The major effect of oxidation is the oxide formation at the bond coat top coat interface. The evolution of TGO and its accompanying effects are discussed in previous sections. The oxidation response of a TBC system depends on the coating design, material properties, and oxidizing environments. The Table 2.2 includes the oxidation performance of a few major top coat material candidates reported by researchers.

Table 2.2 Oxidation behavior of different TBC materials under different atmospheres

<b>Material and Environment</b>	<b>Remarks</b>	<b>Reference</b>
Nanostructured Alumina + YSZ composite 1100 °C	Nanostructured Alumina + YSZ composite had better oxidation resistance than conventional YSZ coatings. A lower TGO thickness was observed in composite coatings for all durations tested.	(Keyvani et al. 2014)
Gd <sub>2</sub> Zr <sub>2</sub> O <sub>7</sub> , YSZ 1100 °C, 100 h	GZ systems showed better oxidation results by their lower thermal conductivity, low oxygen permeability, and structural stability at high temperatures. GZ systems own a lower fracture toughness than YSZ and may lead to the early crack formation during high-temperature exposure	(Doleker and Karaoglanli 2017)
YSZ, YSZ/Al <sub>2</sub> O <sub>3</sub> double layer 1100 °C, 100 h	A thicker TGO was formed in single-layer YSZ coatings than YSZ/Al <sub>2</sub> O <sub>3</sub> double-layer system. Spinel oxides like NiCr <sub>2</sub> O <sub>4</sub> , NiCrO <sub>3</sub> , and NiCrO <sub>4</sub> were formed in YSZ coating, but not seen in a double-layer system. The dense alumina layer prevented oxygen permeation to bond coat.	(Saremi et al. 2008)
Laser modified La <sub>2</sub> Zr <sub>2</sub> O <sub>7</sub> , YSZ double-layer system 1100 °C, 100 h	Laser modification resulted in a dense structure with lower surface roughness. Laser treatment reduced the oxygen permeability and a lower TGO growth was observed. More pure alumina was detected in TGO of treated samples.	(Li et al. 2022)
La <sub>2</sub> Zr <sub>2</sub> O <sub>7</sub> without a bond coat	The oxidation products were Fe <sub>2</sub> O <sub>3</sub> , Cr <sub>2</sub> O <sub>3</sub> , NiCr <sub>2</sub> O <sub>4</sub> , and Nb <sub>2</sub> O <sub>5</sub> . The developed coatings	(Huang et al. 2020)

1100 °C, 110 h	were not efficient in resisting oxidation for a longer duration.	
LaPO <sub>4</sub> /YSZ double-layer (DL)	The spallation of LaPO <sub>4</sub> /YSZ DL TBCs initially occurred in the LaPO <sub>4</sub> coating, while YSZ coating and the interfaces retained structural integrity. The failure was mainly attributed to the low toughness of LaPO <sub>4</sub> .	(Zhang et al. 2018)
1050 °C for 5 min, followed by water quenching.		
GdZ and DyZ	GdZ shows mud-cracking type failure in cyclic testing while 7YSZ and DyZ spall off by buckling-driven strip-like or large area spallation. Single-layer coatings of both GdZ and DySZ show a longer lifetime than the standard 7YSZ. The minimum TGO growth rate was for the single-layer GdZ TBC while DySZ and 7YSZ show very similar TGO growth rate.	(Munawar et al. 2014)
1100 °C for 50 min and forced cooling in 10 min.		
7-YSZ thick TBC with controlled segmentation crack densities	Controlled segmentation densities in the coating were developed manually after coating deposition. This increases strain tolerance by developing vertical cracks in the coating.	
1150 °C for 30 min and force coling by compressed air.	Segmented coating shows a performance better than the standard porous coatings at similar testing conditions.	
Pt and PdPt-aluminide bond coats	The test stopped after 1100 cycles based on non-destructive evaluation indicating the onset of the YSZ top coat delamination.	(Swadźba 2018)

1100 °C for 1.15 h in laboratory air environment followed by 15 min of cooling.	The thickness of the TGO after 1100 cycles on the PdPt aluminide bond coating is 8 μm while that on the Pt aluminide is 10 μm. Oxide scales are composed of typical columnar α-Al <sub>2</sub> O <sub>3</sub> grains.	
8YSZ with NiCrAlY Bond Coat	The growth rate of the oxide layer in the initial hours of isothermal oxidation is higher than the cyclic test, and later the rates become identical.	(Torkashvand et al. 2018)
1070 °C for 30 minutes, cooled to room temperature in 15 minutes.	The existence of TGO with a thickness of approximately 2–3 μm improves the resistance of TBC against thermal shocks. Applying the compound loading (temperature gradient and isothermal) to the TBC samples led to a significant decrease in their cycle life	

### 2.3.2 Hot corrosion behavior of various thermal barrier coatings

The components in gas turbines are exposed to severe corrosive conditions at high temperatures. The ‘hot corrosion’ refers to the severe chemical attack on the component surface due to the elements like Na, S, Cl, and V. These detrimental elements are found to be originated from the fuels and molten ash in the operating environments. The hot corrosion is mainly classified into two; Type-1 (below 750 °C) and Type-2 (above 750 °C). The hot corrosion resistance of a system towards any corrosive salt depends on the material properties and surface properties. The image of a gas turbine component affected by a hot corrosion attack is shown in Figure 2.11. Severe cracking and the presence of blisters were reported on the surface (Eliaz et al. 2002). The salt mixture also plays a significant role in the hot corrosion attack as molten chlorine generally induces cracks in the coating. The Table 2.3 includes the hot corrosion performance of a few major top coat material candidates reported by researchers.

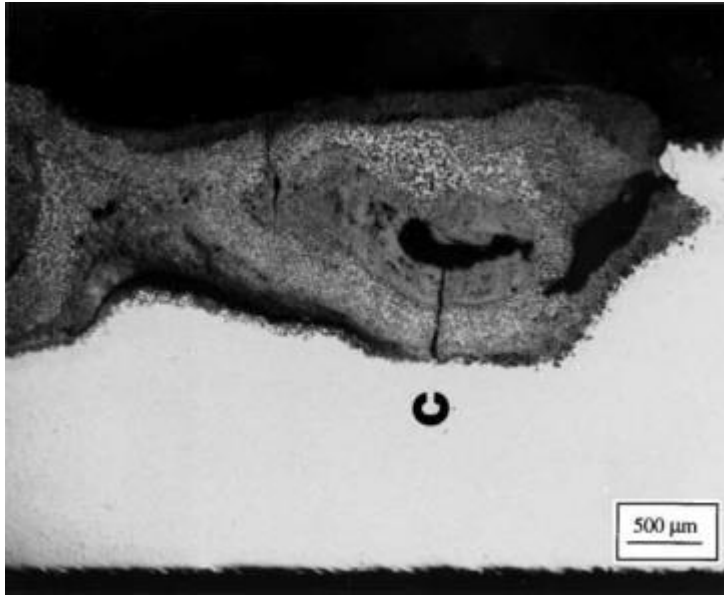


Figure 2.11 The hot corrosion attack on a turbine blade (Eliaz et al.,2002)

Table 2.3 Hot corrosion behavior of different TBC materials under different corrosive conditions

Material Environment	Remarks	Reference
NiCrAlY with alumina/YSZ dispersion	Dispersion of YSZ and alumina increases the hot corrosion rate of NiCrAlY. The test resulted in the formation of spinels, namely NiCr <sub>2</sub> O <sub>4</sub> , NiAl <sub>2</sub> O <sub>4</sub> , and Cr <sub>2</sub> O <sub>3</sub> . The extent of corrosion attack in increasing order- Plain NiCrAlY < NiCrAlY + 25 wt. % Al <sub>2</sub> O <sub>3</sub> < NiCrAlY +25 wt. % YSZ < NiCrAlY +50 wt. % YSZ < NiCrAlY + 75 wt. % YSZ.	(Sreedhar et al. 2009)
Na <sub>2</sub> SO <sub>4</sub> +V <sub>2</sub> O <sub>5</sub> at 800 °C	Leaching of Ytria led to the formation of monoclinic zirconia	
Yb <sub>2</sub> Zr <sub>2</sub> O <sub>7</sub>		(Li et al. 2010)



Molten $V_2O_5$ , 600–800 °C in air	<p>Different reaction products of <math>ZrV_2O_7</math>, <math>YbVO_4</math>, and <math>m-ZrO_2</math> were identified.</p> <p>Vanadium compounds will react more readily with the ceramics having a strong basicity.</p> <p>Formation of <math>m-ZrO_2</math> resulted in cracks.</p>	
<p>3-4 % YSZ</p> <hr/> <p>Air and sulphur rich atmosphere at 750 °C</p>	<p>The YSZ coatings were found to be physically and structurally stable in the air.</p> <p>In air, addition of MgO inhibitor could nullify the corrosive effect of <math>V_2O_5</math> by formation of <math>Mg_3V_2O_8</math> refractory compound.</p> <p>In sulphur- rich atmosphere, YSZ exhibits undesirable phase transformation from t-phase to monoclinic.</p> <p>Effect of MgO inhibitor is not appreciable in sulphur-rich atmosphere.</p>	(Bajpai et al. 2015)
<p>8 % YSZ</p> <hr/> <p><math>Na_2SO_4 + V_2O_5</math> at 950 °C</p>	<p>Formation of <math>YVO_4</math> and <math>m-ZrO_2</math> observed along with <math>NiCr_2O_4</math>, <math>CoCr_2O_4</math>, <math>AlCrO_3</math>, <math>NiCrO_3</math>, <math>CoNiO_3</math> and oxides (<math>NiCrO_4</math>, <math>CoNiO_2</math>, and <math>CoNiO_4</math>) at interface.</p> <p>On cracking or dissolution of TGO, elements diffuse from bond coat to top coat and form spinels.</p> <p>Shift in high-angle peaks indicated a high level of stresses present in the coating due to the formation of <math>YVO_4</math> and <math>m-ZrO_2</math>.</p>	(Qureshi et al. 2016)

LaPO <sub>4</sub> /YSZ	The surfaces of the corroded samples had smooth and rough zones.	
V <sub>2</sub> O <sub>5</sub> salt at 700–1000 °C	No apparent degradation of the coatings could be observed and the interface between the LaPO <sub>4</sub> and the YSZ coatings remains intact. LaPO <sub>4</sub> /YSZ TBCs have high resistance to V <sub>2</sub> O <sub>5</sub> corrosion, which might be due to the formation of La(P,V)O <sub>4</sub> solid solution (little detrimental effect) rather than other new crystals.	(Zhang et al. 2018)
Al <sub>2</sub> O <sub>3</sub> -YSZ composite TBC on gradient MCrAlY coating	The high Al content at the top of gradient CoNiCrAlYSi coatings resulted in the formation of an adhesive, dense, and uniform α-Al <sub>2</sub> O <sub>3</sub> oxide as a TGO. This reduced the oxidation and corrosion of the metallic bond coat. The presence of alumina in the top coat reduced the permeability of the ionic components and oxide ions towards the metallic bond coat and delayed the formation of YVO <sub>4</sub> .	(Mohammadi et al. 2018)
Na <sub>2</sub> SO <sub>4</sub> +NaVO <sub>3</sub> at 880°C	The existence of alumina in the ceramic top coat and as a TGO, led to chemical bonding between TGO and the ceramic top coat interface which moderates the mismatch stresses in the TGO interface.	
Uncoated Superfer 800H (Incoloy)	Very high weight gain was measured, with formation of chromium oxides.	(Singh et al. 2005)
Na <sub>2</sub> SO <sub>4</sub> + 60 % V <sub>2</sub> O <sub>5</sub>	Severe spallation was observed which is	

	attributed to the high strain developed from Fe <sub>2</sub> O <sub>3</sub> precipitation.	
Ni-20 Cr	Formation of phases NiO, Cr <sub>2</sub> O <sub>3</sub> , NiCr <sub>2</sub> O <sub>4</sub> , Ni(VO <sub>3</sub> ) <sub>2</sub> , and Fe <sub>2</sub> O <sub>3</sub> .	
Na <sub>2</sub> SO <sub>4</sub> + 60 % V <sub>2</sub> O <sub>5</sub>	Also, Al <sub>2</sub> O <sub>3</sub> is formed through the diffusion of Al from a substrate.	
Ni <sub>3</sub> Al	Inferior hot corrosion than Ni-20 Cr and NiCrAlY.	
Na <sub>2</sub> SO <sub>4</sub> + 60 % V <sub>2</sub> O <sub>5</sub> .	Formation of Ni <sub>3</sub> Al phase, and diffusion of Cr and Fe from the bond coat to the top surface was seen.	
LaTi <sub>2</sub> Al <sub>9</sub> O <sub>19</sub> /YSZ	LTA/YSZ DL system completed 1458 hot corrosion cycles in the corrosive atmosphere, while the samples completed 3033 thermal cycles without any corrosive salts. No decomposition of LTA was observed after the hot corrosion test. The molten salts infiltrate through cracks and react with a bond coat.	(Xiaoyun et al. 2012)
Na <sub>2</sub> SO <sub>4</sub> + NaCl		
YSZ, Gd <sub>2</sub> Zr <sub>2</sub> O <sub>7</sub> , YSZ/Gd <sub>2</sub> Zr <sub>2</sub> O <sub>7</sub>	Increased V <sub>2</sub> O <sub>5</sub> accelerated the damage of coatings. The double-layer system was more resistant to hot corrosion than single-layer coatings.	
45 wt.% Na <sub>2</sub> SO <sub>4</sub> + 55 wt.% V <sub>2</sub> O <sub>5</sub> at 1000 °C	Monoclinic zirconia and rod-shaped GdVO <sub>4</sub> and YVO <sub>4</sub> were identified as corrosion products. The columnar structure of the coatings was heavily damaged by corrosion.	(Jonnalagadda et al. 2017)

In general, the top coats tend to lose their stability in the presence of corrosive salts at high temperatures. Also, double-layer or composite-layer systems showed better resistance than single-layer top coats.

### 2.3.3 Erosion behavior of various thermal barrier coatings

Erosion is the mechanism of material removal from a component surface under the influence of external agents such as abrasive particles, gas streams, water jets etc. The gas turbine components are generally prone to erosion from solid particle impingement at higher temperatures. The erodents under the influence of high temperature can create substantial damage to the system, leading to thinning of components and failure. Figure 2.12 shows an eroded area in a turbine blade (Naib 2016).

The thermal barrier coating system can delay or prevent the material removal leading to the longevity of components. In general, the erosion response of a coating system depends on the impingement variables, erodent variables, and material variables. The main impingement variables include the erodent flux, velocity, and impact angle, while the erodent variables refer to the shape, size, and hardness of the erodent particle being impacted. The material variables include mechanical characteristics such as hardness, and microstructural features like porosities and defects (Krishnamurthy et al. 2012). The erosion behavior of different TBC systems tested under different erosion conditions and sample conditions are listed in Table 2.4.

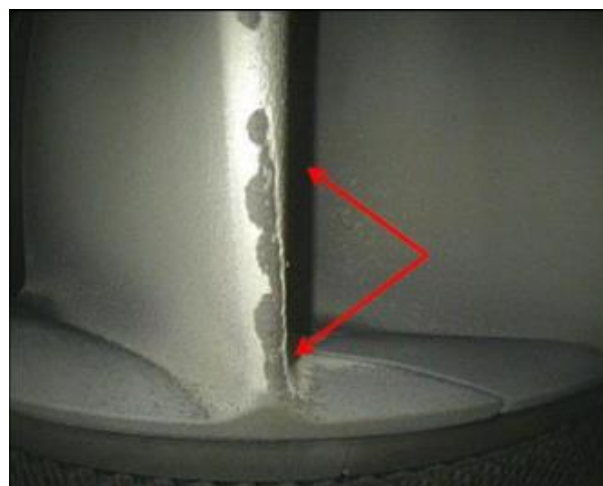


Figure 2.12 Photograph showing erosion in a turbine blade (Naib, 2016)

Table 2.4 Erosion behavior of different TBC materials under different erosive conditions

<b>Material</b>	<b>Remarks</b>	<b>Reference</b>
WC-Co/NiCrFeSiB	Ductile and brittle modes of material removal under erosion with silica sand at 40 m/s	(Ramesh et al. 2010)
Gadolinium Zirconate	Gd/YSZ double-layer measured higher fracture toughness and high erosion resistance when eroded under 50 $\mu$ m alumina at 110 m/s The cracks propagated along the lamellar microstructure aided in increasing the erosion resistance	(Yang et al. 2021)
Al <sub>2</sub> O <sub>3</sub> -TiO <sub>2</sub>	The sintered and coated samples offered a higher erosion resistance. The denser HVOF samples showed higher resistance than APS samples	(Matikainen et al. 2014)
8 % YSZ	EB-PVD coatings are more resistant to erosion than equivalent APS coatings, at both room temperature and higher temperature Maximum erosion is observed at a 90° impact angle	(Nicholls et al. 1999)
7-8 % YSZ	Erosion resistance decreased with increasing porosity. An increase in porosity from 15 % to 20 % traded off the erosion resistance. The high hardness can resist erosion damage to a greater extent	(Mahade et al. 2021)

The mechanism of oxidation, hot corrosion, and erosion are primarily dependent on the surface characteristics. Any alterations on the surface can affect the performance of the system.

## **2.4 Surface modification of coatings**

Surface modifications on coating have been performed to overcome certain shortcomings of thermal sprayed coatings. The performance of the thermal barrier coatings is highly dependent on the microstructure of the system. The surface modification techniques like shot peening, thermo-chemical processes, and laser treatment facilitate a desirable change in morphology and microstructure (Alexander et al. 2020).

### **2.4.1 Laser modification**

The thermal sprayed coatings often reveal open porosities on the surface, which is detrimental to oxidation and hot corrosion resistance at high temperatures. Also, the coated surfaces are often identified with unmolten particles which brings down the mechanical properties of the component. The surface modification by laser treatment aids in providing a better surface by remelting the existing surface and sealing off the porosities and other defects. In addition, the control of parameters can induce segmented cracks in the coating, which improves the strain tolerance during high-temperature operation. The densified layer on top may tend to increase the thermal conductivity, while it offers higher protection in critical environments. The laser treatment of a YSZ/Lanthanum hexa-aluminate gradient coating produced a dense layer with segmentation cracks as in the schematic shown in Figure 2.13. The entrapment of gases within the system aids in preventing the easy conduction of thermal energy across the coating (Khan et al. 2021). Lower oxidation and lower TGO growth in laser-treated YSZ coatings have been reported (Múnez et al. 2011). Figure 2.14 shows a densified YSZ top layer produced from laser glazing.

The laser treatment of coatings is a complex phenomenon subject to the coating material, surface conditions, and laser parameters. The Table 2.5 shows the effect of laser treatment on various TBC systems. A lower energy density may lead to insufficient melting, while higher energy tend to shrink the layer due to ablation and may lead to warping. The response of the material may vary according to its absorption characteristics. Bulk alumina is reflective to laser until 1500 °C, while the absorptance rises with a further temperature rise (Zhang and Modest 1998).

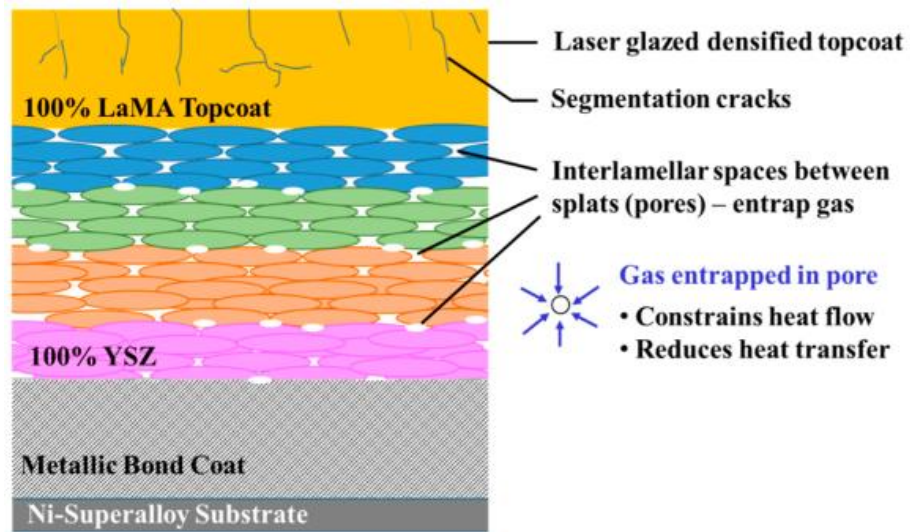


Figure 2.13 Schematic of densification of top coat by laser- treatment in a YSZ-Lanthanum hexa-aluminate gradient coating (Khan et al., 2021)

Table 2.5 Effect of laser treatment in different TBC systems

Material	Remarks on laser treatment	Reference
$Al_2O_3$	Observed phase transformations from metastable phases. Produced a dense microstructure with a pore-free surface and thermally induced cracks	(Moriya et al. 2016)
8 YSZ	Abrasion resistance increases by laser glazing. Segmentation cracks are seen on the top coat	(Ahmaniemi et al. 2004)
8YSZ	Induces a densified layer with cracks perpendicular to the surface. Improved damage tolerance is observed. The oxidation is reported to be delayed after laser treatment.	(Múnez et al. 2011)

As ceramics have a very high melting point, the usage of low melting eutectic binders with ceramics is also a practice to ensure desired melting. The additives must

not react with the coating powders, but should absorb the laser energy (Zhang and LeBlanc 2016).

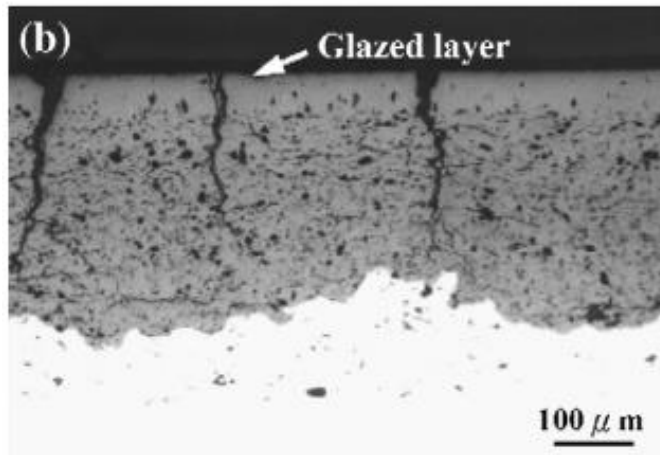


Figure 2.14 Laser glazed YSZ thermal barrier coating with a top densified layer (Tsai et al., 2007)

## 2.5 Summary of literature and importance of the present study

The field of thermal barrier coatings has seen a larger extent of research and resultant progress in performance. The reported research sheds light on the fact that no materials used to date are delighting at resisting all the failure mechanisms possible at higher temperatures. The single-layer designs do not offer adequate protection, while the double-layer designs suffer from thermal expansion mismatch concerns. A composite coating with proper material choices can perform satisfactorily at higher temperatures. Still, the amount of research data on such composite coatings is slender.

Alumina is well-known for its least diffusivity and high density. Reports suggest a higher oxidation and hot corrosion resistance in  $\text{Al}_2\text{O}_3$ -YSZ composite coatings, with the best performance with 65 wt.% of alumina content in the composite. The rare earth material  $\text{Sm}_2\text{SrAl}_2\text{O}_7$  is proved to be a competent candidate for TBC. A comparison of properties is given in Table 2.6 (Feng et al. 2012; Lampke et al. 2011). The thermal expansion coefficients of SSA and alumina are not outlying enough to cause major mismatch failures. Moreover, the introduction of a comparatively softer material into the alumina matrix can enhance strain tolerance and reduce cracking tendencies. An  $\text{Al}_2\text{O}_3$  -  $\text{Sm}_2\text{SrAl}_2\text{O}_7$  composite thermal barrier coating is envisaged to perform better



in high-temperature environments. It is believed that the outcome of the proposed research work will contribute to the progress of the thermal barrier coating domain.

Table 2.6 Comparison of properties of alumina and SSA

	<b>Al<sub>2</sub>O<sub>3</sub></b>	<b>Sm<sub>2</sub>SrAl<sub>2</sub>O<sub>7</sub></b>
Thermal expansion coefficient ( $\alpha$ )	$8.68 \times 10^{-6} \text{ K}^{-1}$	$10-12 \times 10^{-6} \text{ K}^{-1}$
Thermal conductivity	$5.8 \text{ Wm}^{-1}\text{K}^{-1}$	$2.3 \text{ Wm}^{-1}\text{K}^{-1}$

## 2.6 Objectives of the study

- ✓ To synthesize, samarium strontium aluminate powder using molten salt synthesis and to develop a  $\text{Al}_2\text{O}_3$  -  $\text{Sm}_2\text{SrAl}_2\text{O}_7$  composite thermal barrier coating on Inconel 718 with NiCrAlY bond coat.
- ✓ To examine the oxidation resistance of the  $\text{Al}_2\text{O}_3$  -  $\text{Sm}_2\text{SrAl}_2\text{O}_7$  composite coatings.
- ✓ To analyze the performance of the  $\text{Al}_2\text{O}_3$  -  $\text{Sm}_2\text{SrAl}_2\text{O}_7$  composite coatings against hot corrosion in aviation and marine atmospheres.
- ✓ To investigate the solid particle erosion resistance of the system at high temperatures.
- ✓ To study the effect of surface modification on oxidation, hot corrosion and high temperature erosion of the TBC system.

### 3 Materials and Methods

This chapter includes a detailed description of the procedures followed, equipment used for the development of the 70 wt. %  $\text{Al}_2\text{O}_3$  - 30 wt. %  $\text{Sm}_2\text{SrAl}_2\text{O}_7$  composite thermal barrier coatings and surface modification using laser. The strategies and practices used for oxidation, hot corrosion, erosion tests, and sample characterizations are discussed in detail.

#### 3.1 Preparation of coating feedstock

The rare earth ceramic samarium strontium aluminate (SSA) was synthesized via molten salt synthesis technique from the precursor components  $\text{Sm}_2\text{O}_3$ ,  $\text{SrO}$ , and  $\text{Al}_2\text{O}_3$ . The flowchart of the synthesis process is shown in Figure 3.1.

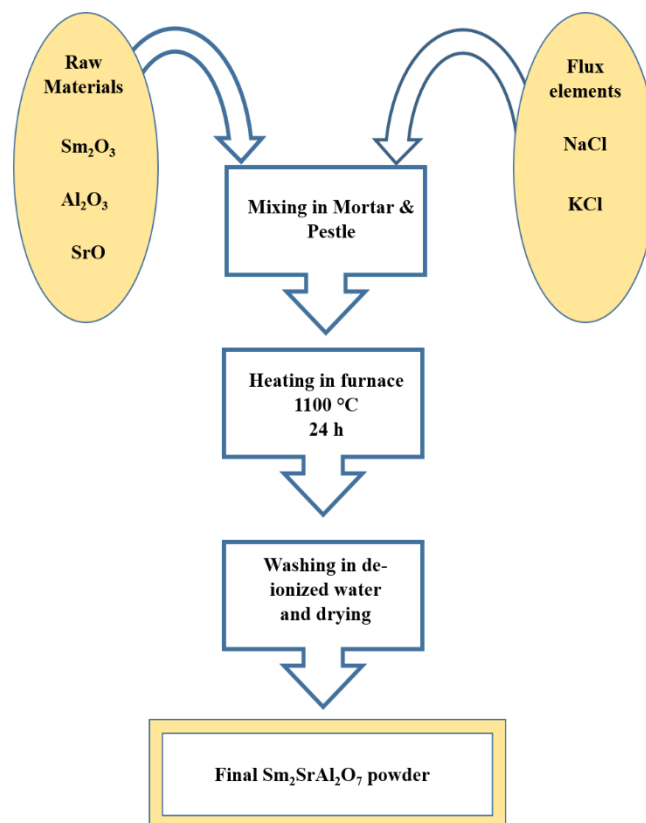


Figure 3.1 Flowchart of  $\text{Sm}_2\text{SrAl}_2\text{O}_7$  synthesis

The powders were precisely mixed in the molar ratio. The thoroughly blended raw materials were mixed with the flux constituents KCl + NaCl for about 30 minutes using a mortar and pestle, at room temperature. The mixture transferred to a crucible is heated up to 1100 °C at a rate of 6 °/min and held for 24 h in a controlled atmosphere muffle furnace. The heat-treated powder was furnace cooled to ambient temperature and cleaned with de-ionized water to remove the flux contents. Thorough washing in warm water is performed to ensure cleansing of flux. The moisture content in the obtained powder is dried away by heating in a hot air oven at 110 °C for 3 h to acquire the final high-purity SSA powder. The photographic image of the synthesized SSA powder is shown in Figure 3.2.

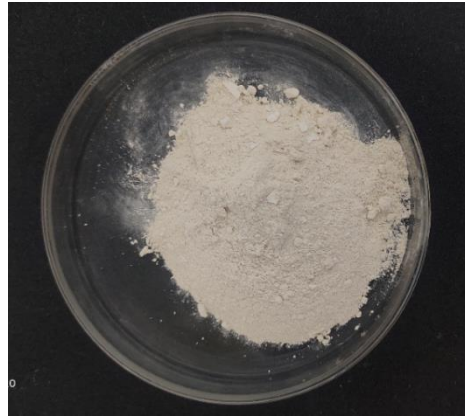


Figure 3.2 Photographic image of synthesized SSA powder

High-purity alumina powder (Make: HC Starck, 45/5 microns) was procured to prepare the composite powder for the top coat. The laboratory-synthesized SSA and the 99.99 % pure alumina powder were mixed in the required weight ratio to prepare 70 wt.%  $\text{Al}_2\text{O}_3$  - 30 wt.%  $\text{Sm}_2\text{SrAl}_2\text{O}_7$  top coat powder. Commercially available NiCrAlY powder with the composition (wt.%) given in Table 3.1 was used as the bond coat. A composition with Cr > 20 %, and Al > 5 % yield a better performance to coatings (Stecura 1985). Inconel 718 superalloy is procured to use as the substrate considering the gas turbine blade components. The chemical composition (wt.%) of the Inconel 718 substrate analyzed through optical emission spectroscopy is shown in Table 3.2.

Table 3.1 Composition (wt.%) of commercially available NiCrAlY powder used for bond coat

Element	Ni	Cr	Al	Y
wt.%	64.8	22.5	10.8	1.2

Table 3.2 Composition of Inconel 718 substrate in wt.%

Element	Ni	Cr	Fe	Nb	Mo	Al	Ti	Co	Mn
wt.%	54.69	17.61	17.70	5.26	2.83	0.22	0.9	0.36	0.24

The 5 mm thick Inconel 718 sheet was cut into pieces of dimensions 20 mm × 20 mm × 5 mm and 10 mm × 10 mm × 5 mm using electrical discharge machining (EDM). The substrate samples were thoroughly cleaned with acetone and grit blasted with alumina (grit size 60 mesh), to a surface roughness of 6-8 μm before the onset of the coating process. The thermal barrier coating was developed through Atmospheric Plasma Spraying (APS) employing a mass flow controlled plasma system AP 2700 (Metallizing Equipment Pvt Ltd, Jodhpur) equipped with an MF4 spray gun, with argon and hydrogen as primary and secondary gases. The schematic of the employed APS process is shown in Figure 3.3, and the parameters used for coating the specimen are given in Table 3.3.

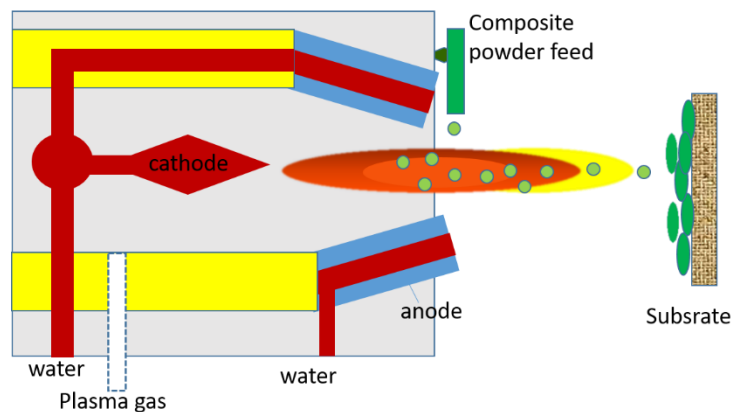


Figure 3.3 Schematic of the plasma spray setup

Table 3.3 Operating parameters used for atmospheric plasma spray coating

	Bond coat	Top coat
Coating Powder	NiCrAlY	Al <sub>2</sub> O <sub>3</sub> - SSA Powder
Coating System	APS	APS
Spray gun	MF4	MF4
Voltage	65 V	69 V
Current	500 Amp.	575 Amp.
Primary gas flow (Argon)	40 slpm <sup>1</sup>	38 slpm
Secondary gas flow (Hydrogen)	6.0 slpm	8.0 slpm
Powder feed rate	40 g/min	35 g/min
Spray distance	120 mm	75 mm

### 3.2 Laser modification of samples

The surface modification of the developed TBC specimen is carried out by deploying an Nd: YAG fiber laser. An optimum laser energy density is achieved by adjusting the parameters such as laser power, scanning speed, and focus area. A lower energy density would lead to inadequate heating, while a higher energy leads to burning, shrinkage, or ablation (Buckner et al. 2016).

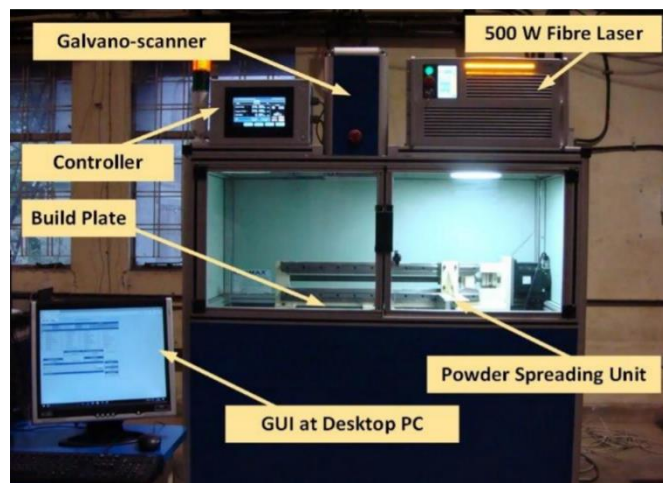


Figure 3.4 Equipment used for laser treatment of developed samples

<sup>1</sup> Standard litres per minute

Process parameters employed were identified considering minimum surface porosity, surface roughness, and absence of burn or vaporization of the surface. The laser parameters like power and scanning speed were optimized to avoid any burning marks on the surface. Each TBC material will respond differently to the laser glazing according to its adsorption properties. Trial experiments were carried out with various laser powers ranging from 30 W to 110 W, with the equipment shown in Figure 3.4.A beam diameter of 500  $\mu\text{m}$  was used to scan the surface with the laser beam.

### **3.3 Characterization of coatings**

The samples developed by atmospheric plasma spray were subjected to detailed analysis such as phase analysis by X-ray diffraction (XRD), morphology, and cross-section analysis by scanning electron microscopy (SEM), porosity, and density measurements. A detailed phase analysis and orientation mapping have been done through electron backscattered diffraction (EBSD) studies. The samples have been sectioned using Struers secotom-60 precision cutting machine to observe the cross-section. Nanoindentation measurements have also been performed on the samples using a Berkovich diamond indenter of 20 nm tip.

#### **3.3.1 Density and porosity measurements**

The density of the coatings was determined by a pycnometer of 50 mL capacity as per ASTM C-135-96. Multiple measurements have been made to ensure the accuracy of the test. Porosity analysis was performed by both image analysis and water impregnation techniques. The coatings were carefully peeled off from the substrate, and water impregnation was performed under a vacuum for 15 minutes. The porosity has been analyzed through image analysis, using Axio-vision SE64 multiphase analyzer. Multiple images have been analyzed to obtain an average value of porosity.

#### **3.3.2 Electrochemical Impedance Spectroscopy measurements**

The electrochemical impedance spectroscopy (EIS) test was performed on the samples using a Biologic SP-240 potentiostat system. A three-electrode system was used with the coated sample as the working electrode, a saturated calomel electrode as a reference and a platinum electrode as the counter electrode. An electrolyte solution

0.01 M  $K_3Fe(CN)_6/K_4Fe(CN)_6$  with higher electrochemical exchange current density was used for the test. The EIS tests were performed on a surface area of  $1\text{ cm}^2$ , with an AC amplitude of 10 mV and a frequency sweep range of  $10^{-3}\text{ Hz}$  to  $10^{-5}\text{ Hz}$ .

### **3.4 High-temperature isothermal oxidation tests**

Isothermal oxidation studies were carried out on the developed samples in as-coated and laser-treated conditions to assess the high-temperature behavior. The oxidation tests were performed at  $1100\text{ }^\circ\text{C}$  in a controlled atmosphere muffle furnace of accuracy  $\pm 1\text{ }^\circ\text{C}$ . The weight of the samples was monitored at regular intervals to track the changes during high-temperature exposure. A microbalance (Contech- CAS 234) with an accuracy of  $\pm 0.0001\text{ g}$  was used to track the weight changes during the test. The sample surface and cross-sections were analyzed to examine the oxidation mechanism and TGO formation.

### **3.5 Hot corrosion tests**

Hot corrosion tests under various conditions were performed on the samples to analyze the corrosion resistance of the developed coatings at higher temperatures. The corrosion tests were carried out at  $700\text{ }^\circ\text{C}$  and  $900\text{ }^\circ\text{C}$  in a controlled atmosphere furnace with two salt compositions 50 %wt.  $Na_2SO_4$  + 50 %wt.  $V_2O_5$  (Aviation conditions-salt 1), and 90 %wt.  $Na_2SO_4$  + 5 %wt.  $V_2O_5$  + 5 %wt.  $NaCl$  (Marine conditions-salt 2).

The required salts are weighed in proportion and thoroughly mixed in mortar and pestle with distilled water to prepare a corrosive slurry. For the aviation conditions, 10 g of the corrosive slurry was prepared with 5 g of  $Na_2SO_4$  and  $V_2O_5$ . For the marine conditions, 10 g of the corrosive slurry was prepared from 9 g of  $Na_2SO_4$ , 0.5 g of  $V_2O_5$ , and 0.5 g of  $NaCl$ . The prepared salt slurry was carefully applied to the center of the sample, using a paintbrush, leaving 2 mm space from all edges to avoid an edge effect. The applied samples were then dried in a hot air oven at  $120\text{ }^\circ\text{C}$  for 1 h and the samples were weighed to confirm the amount of salts applied to be around  $20\text{ mg/cm}^2$ . The photographic images of the samples used for hot corrosion tests are shown in Figure 3.5. The test coupons were then heated at  $700\text{ }^\circ\text{C}$  and  $900\text{ }^\circ\text{C}$  in a muffle furnace in the presence of air. The samples were observed every 10 h time interval to confirm the integrity of the coatings. Upon visual inspection, a 20 % spallation of the coating was



considered a failure, and the samples were removed (Ganvir et al. 2018; Mahade et al. 2016). The failed coatings were analyzed in SEM, XRD, and Raman spectroscopy for examining the changes in surface morphology, products formed, and the possible mechanisms undergone. The hot corrosion tests were performed on both as-coated samples (AS) and laser-treated samples (LS) to identify the influence of laser glazing on the hot corrosion resistance of the thermal barrier coating system.

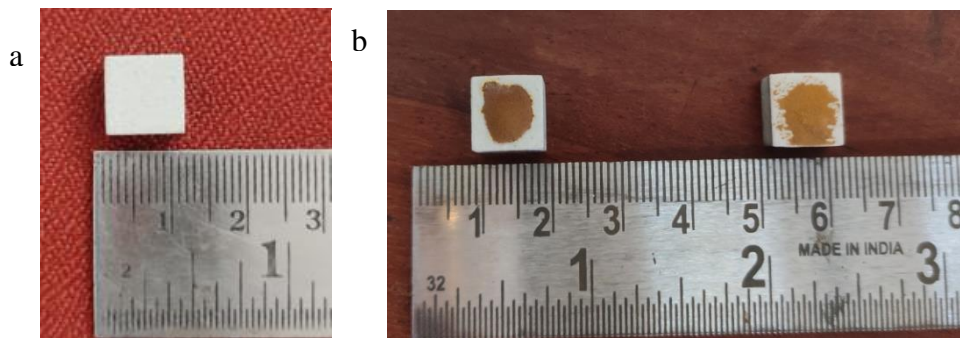


Figure 3.5 Photographic images showing a) developed samples for hot corrosion  
b) samples with corrosive salts applied on surface

### 3.6 Erosion tests

Air jet erosion tests at higher temperatures were carried out on the developed thermal barrier coatings of dimension  $20 \text{ mm} \times 20 \text{ mm} \times 5 \text{ mm}$ , at  $200 \text{ }^\circ\text{C}$  and  $800 \text{ }^\circ\text{C}$  at  $30^\circ$  and  $90^\circ$  angles according to ASTM G76-13 test standard using a Ducom air jet erosion tester (Model: TR-471-800). The schematic diagram of the test setup and the erosion test facility used is shown in Figure 3.6 and Figure 3.7. The as-coated (AS) and laser surface-treated (LS) test coupons were cleaned using acetone and tested for erosion behavior. The erosion tester was equipped with a furnace to heat the samples to the test temperature. The samples were heated to  $200 \text{ }^\circ\text{C}$  and  $800 \text{ }^\circ\text{C}$  and eroded at impingement angles of  $30^\circ$  and  $90^\circ$  using  $50 \text{ }\mu\text{m}$  alumina erodent. The hardness of alumina erodent was about  $16.9 \text{ GPa}$  (Muruges and Scattergood 1991). The parameters used for the erosion test are listed in Table 3.4. Before the onset of erosion, the heated samples were held for 15 min, allowing them to reach a uniform temperature throughout. The erosion weight loss of the specimens was measured every 5 minutes using a Shimadzu-AUX 220 precision weighing balance. The steady-state erosion rate and average erosion values were calculated according to the mentioned standard.

Table 3.4 Parameters used for air jet erosion testing

Erodent	Alumina, 50 $\mu\text{m}$
Feed rate	3 g/min
Velocity	40 m/s
Temperatures	200 $^{\circ}\text{C}$ and 800 $^{\circ}\text{C}$
Impingement angles	30 $^{\circ}$ and 90 $^{\circ}$
Nozzle dimension	1.5 mm ID
Stand-off distance	10 mm

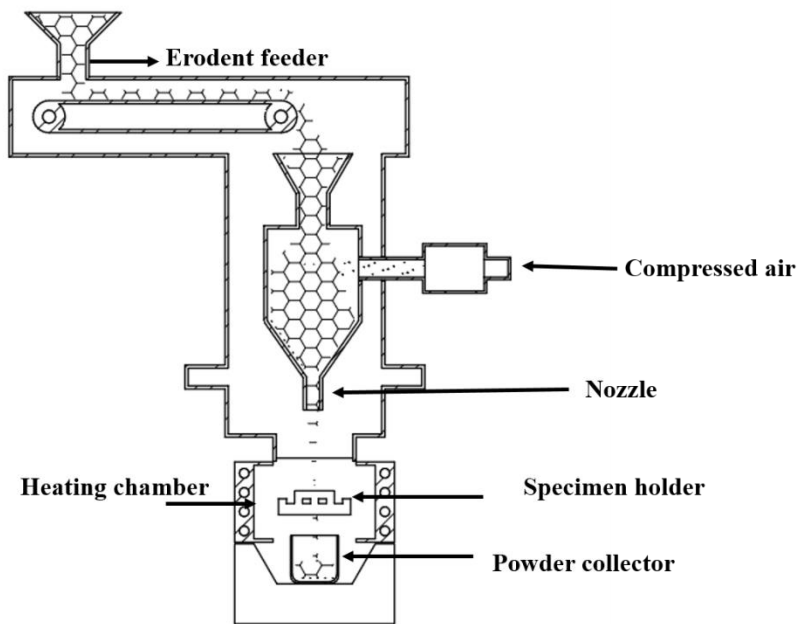


Figure 3.6 Schematic diagram of the erosion testing facility

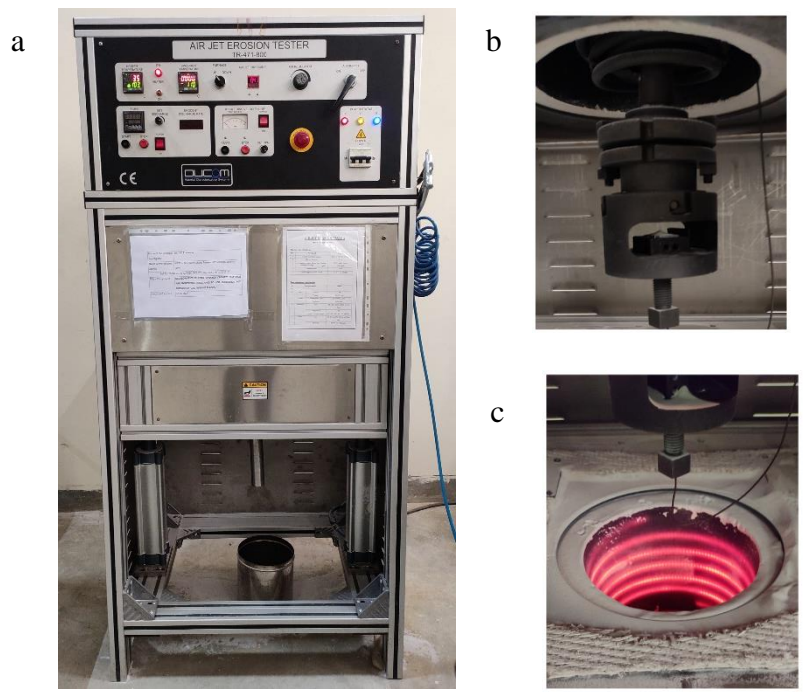


Figure 3.7 a) Air jet erosion tester, b) sample holder and c) heating setup employed for high temperature erosion testing



## Results and Discussion

### 4 Coating development and characterization of as-coated samples

A composite thermal barrier coating system with a top coat composition of 70 wt. %  $\text{Al}_2\text{O}_3$  - 30 wt. %  $\text{Sm}_2\text{SrAl}_2\text{O}_7$  was developed through atmospheric plasma spray technique. The various characteristics of the raw materials and the developed coatings are investigated in detail for a thorough understanding.

#### 4.1 Feedstock materials

An Inconel 718 superalloy was used as the substrate for thermal barrier coating development. The top coat composite powder has been prepared from laboratory-synthesized  $\text{Sm}_2\text{SrAl}_2\text{O}_7$  powder and high-purity alumina powder procured from HC Starck, USA. The feedstock powders were characterized in SEM and XRD to observe the surface morphology and phases of the powders.

##### 4.1.1 Samarium strontium aluminate

The morphology of the developed  $\text{Sm}_2\text{SrAl}_2\text{O}_7$  powder at different magnifications is shown in Figure 4.1. The SSA particles showcased a cuboidal shape with an average particle size of 30  $\mu\text{m}$ . A cuboidal shape was observed in fused and crushed powders and is susceptible to lower flowability concerns. In the developed powder, the product lumps were crushed and washed, leading to the observed particle shape. The spherical powders were preferred to ensure uninterrupted feeding and to avoid the clogging of particles upon injection. On the other hand, a non-spherical particle has a lower elastic rebounding tendency, in case of a partial or unmolten impact on the substrate (Nouri and Sola 2019).

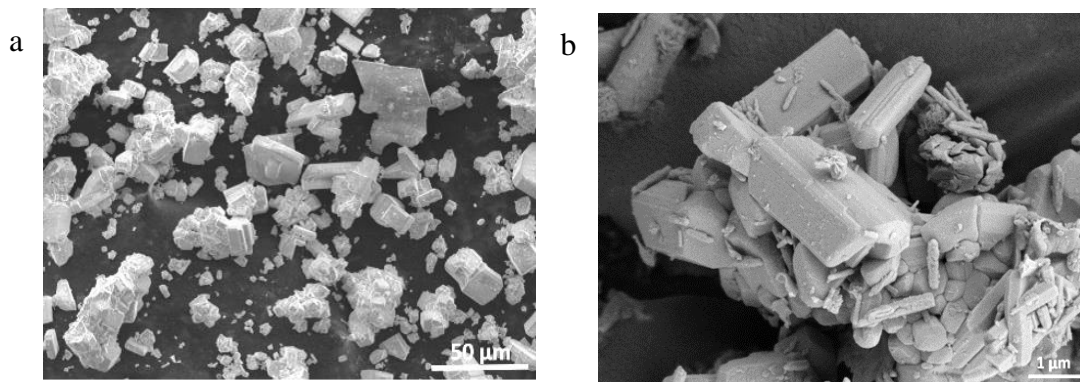


Figure 4.1 The morphology of synthesized SSA powder in a) low and b) high magnifications

The XRD pattern of the synthesized  $\text{Sm}_2\text{SrAl}_2\text{O}_7$  powder, as in Figure 4.2, showed a single-phase tetragonal structure as per the JCPDS card number 01-074-3404. The composition of the powder was confirmed and no impurity elements or phases were detected.

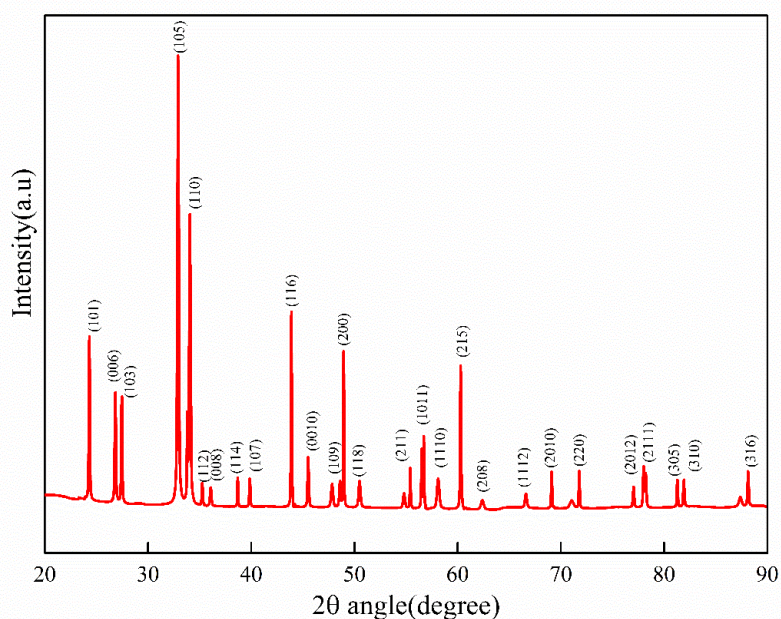


Figure 4.2 XRD pattern of the SSA powder synthesized at 1100 °C for 24 h in controlled atmosphere furnace

The crystal structure of  $\text{Sm}_2\text{SrAl}_2\text{O}_7$  viewed through VESTA software is shown in Figure 4.3. The VESTA (Visualization for Electronic Structural Analysis) is a 3D visualization software to demonstrate structural models and crystallographic morphologies. A similar structure for  $\text{RE}_2\text{SrAl}_2\text{O}_7$  compounds have been reported by other researchers (Zvereva et al. 2003). SSA possesses a tetragonal structure with

periodic stacks of double perovskite blocks of  $\text{AlO}_6$  octahedra and  $\text{SmO}_5$  polyhedra. The Sm and Sr occupy the Wyckoff positions in the structure. The compound has very weak anisotropic elastic properties and quite low directional dependence.

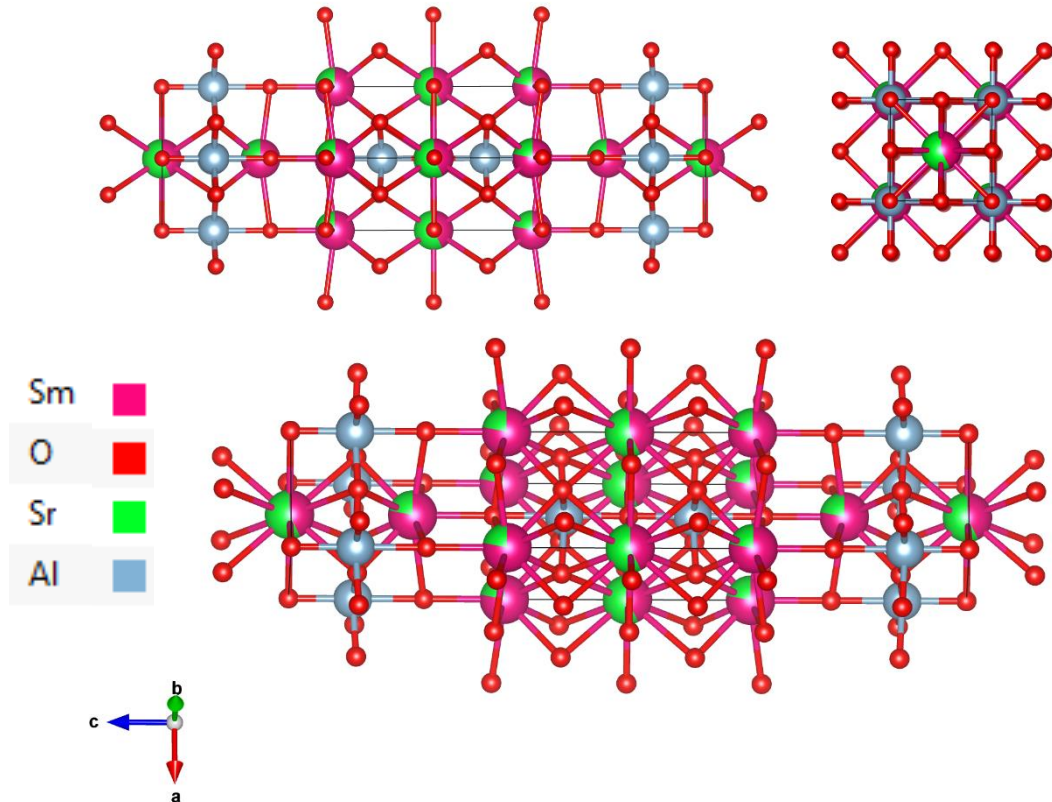


Figure 4.3 Crystal structure of samarium strontium aluminate powder developed from VESTA software

#### 4.1.2 Alumina powder

The SEM images of the alumina powder used are shown in Figure 4.4. The particles presented an average size of  $30\ \mu\text{m}$ , with a nearly uniform size distribution. The XRD spectrum of the alumina powder (Figure 4.5) showed only an alpha phase with a rhombohedral structure as per JCPDS card number 00-042-1468. No traces of any other metastable phases, such as  $\gamma\text{-Al}_2\text{O}_3$  or  $\theta\text{-Al}_2\text{O}_3$ , were observed in the XRD data. Alpha is the most stable phase of alumina with a rhombohedral structure. Figure 4.6 shows the rhombohedral crystal structure of alumina used, viewed through VESTA software.

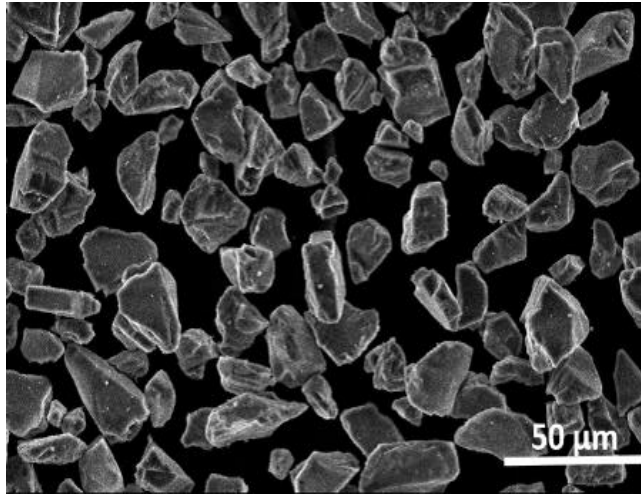


Figure 4.4 Morphology of alumina powder used in composite top coat

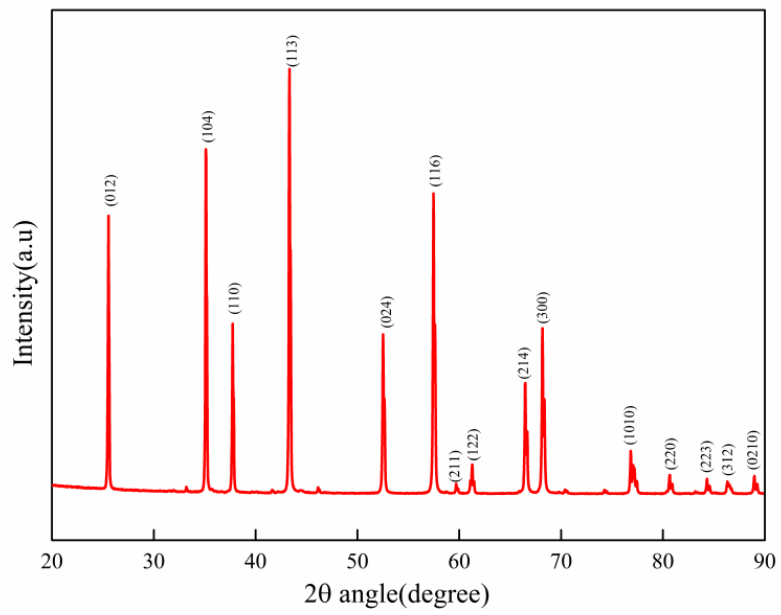


Figure 4.5 XRD spectrum of alumina powder used for composite top coat



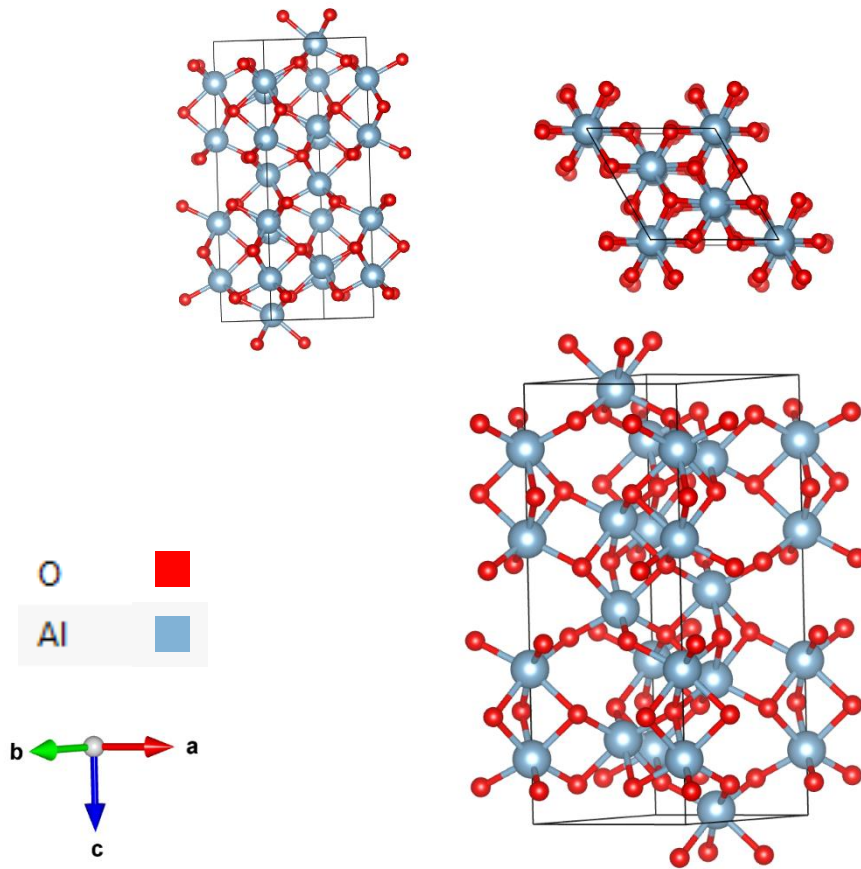


Figure 4.6 Crystal structure of alumina powder developed from VESTA software

### 4.1.3 Composite powder mixture

The composite powder for the top coat was prepared by thoroughly mixing the alumina and SSA powder in a 70:30 weight ratio. Figure 4.7 shows the distribution and EDS composition of the powder particles in the prepared mixture. Powder particle shapes and corresponding compositions have been confirmed through EDS analysis, as shown in Figure 4.7-b and Figure 4.7-c. The flowability of the feedstock powder influences the coating process and the resulting microstructure. The flowability of the composite powder mixture was found using the Hall Flowmeter Funnel test according to ASTM B-213 standard test method. The composite powder was found to flow continuously, while the pure SSA powder was not flowing through the orifice due to interparticle friction. The addition of alumina have aided flowability to the composite system.

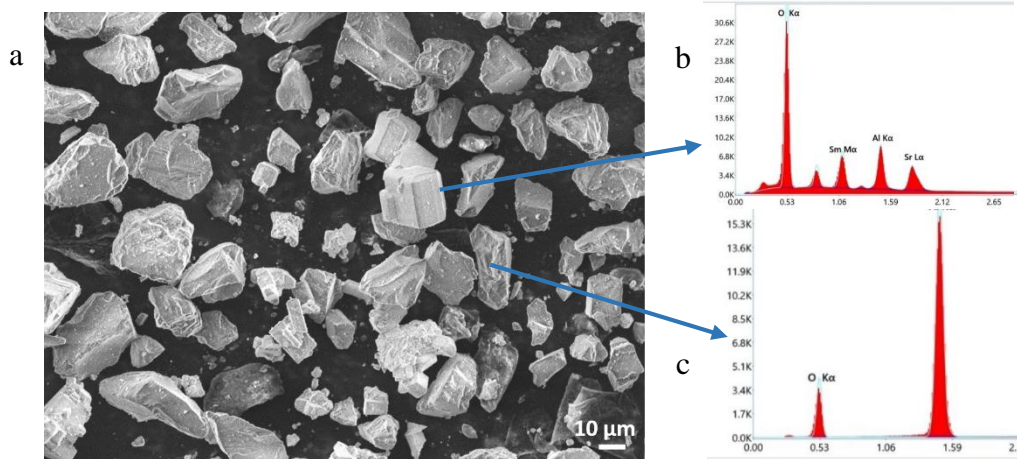


Figure 4.7 a) SEM image of the composite mixture b), c) EDS analysis of SSA and alumina particle in the composite mixture respectively

## 4.2 As-coated TBC sample

The 70 wt. %  $\text{Al}_2\text{O}_3$  - 30 wt. %  $\text{Sm}_2\text{SrAl}_2\text{O}_7$  composite thermal barrier coatings were developed using the atmospheric plasma spray technique using the parameters listed in Table 3.3. The developed coatings were analyzed in detail to examine the various characteristics of the TBC system. The density of the coatings was determined using pycnometer measurements according to ASTM C-135-96 standard. Multiple measurements were taken and the average density value was calculated as  $4.4 \text{ g/cm}^3$ . The measured value is close to the theoretical density of the composite system. The porosity of the coating was observed to be 10 % by image analysis (as per ASTM-B276) and water intrusion techniques. The surface studies of the as-sprayed coatings using a Nanovea ST-400 surface profilometer measured surface roughness of about  $6.0 \text{ } \mu\text{m}$ .

The surface examination of the as-sprayed samples showed a splat morphology with few microcracks. The morphology of the as-coated specimens observed under SEM at different magnifications is shown in Figure 4.8. The morphology of the as-coated system presented a splat structure, resulting from the flattened droplets on solidification. Upon impact on the substrate, the molten particles flatten and solidify forming disc-shaped splats. A similar morphology for pure  $\text{Al}_2\text{O}_3$  single-layer coating was reported by other researchers (Krishnamurthy et al. 2012). The overall dispersal of the molten particles was found to be even, leading to a satisfactory surface.

Additionally, no major cracks were noticed in the as-coated morphology, pointing to the integrity of the coating. The higher magnification views of the surface revealed very few microcracks on the splats. The cracks are assumed to be originated from the thermal shock-induced stress during coating. Upon cooling after spraying, the difference in thermal expansion causes residual stresses which may further lead to crack initiation (Krishnamurthy et al. 2012).

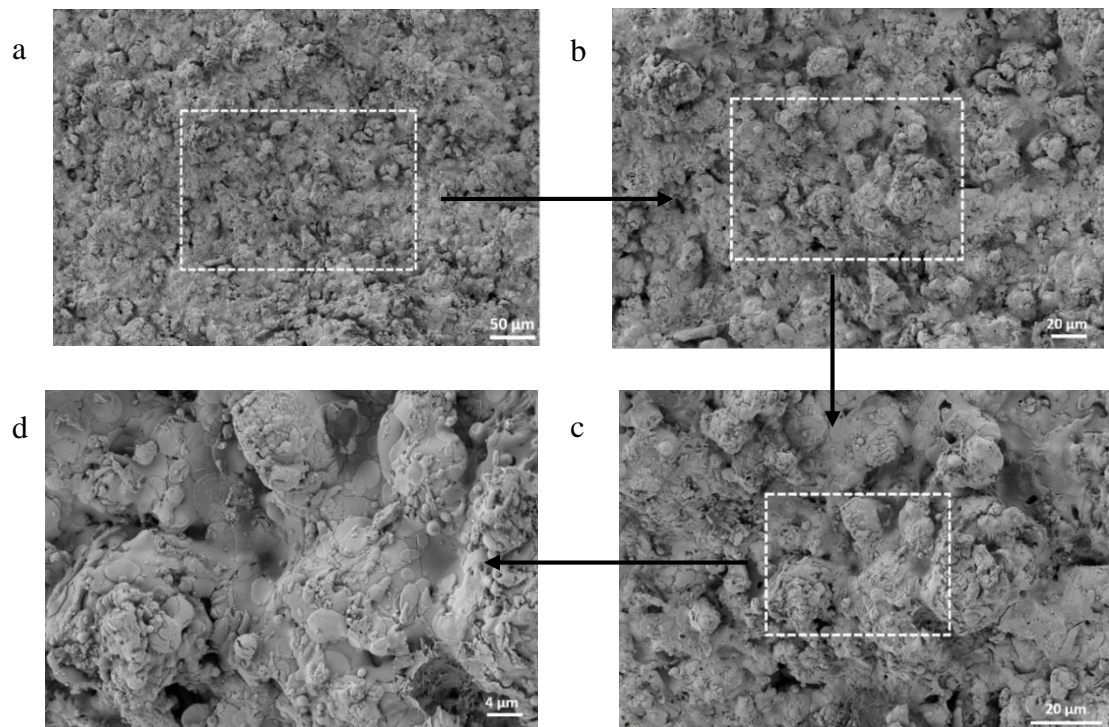


Figure 4.8 The surface of as-coated specimen viewed in SEM at different magnifications

The cross-sectional observation revealed a lamellar microstructure of the top coat. The average bond coat thickness was measured to be about 80  $\mu\text{m}$  and the top coat thickness was about 200  $\mu\text{m}$  as shown in Figure 4.9.

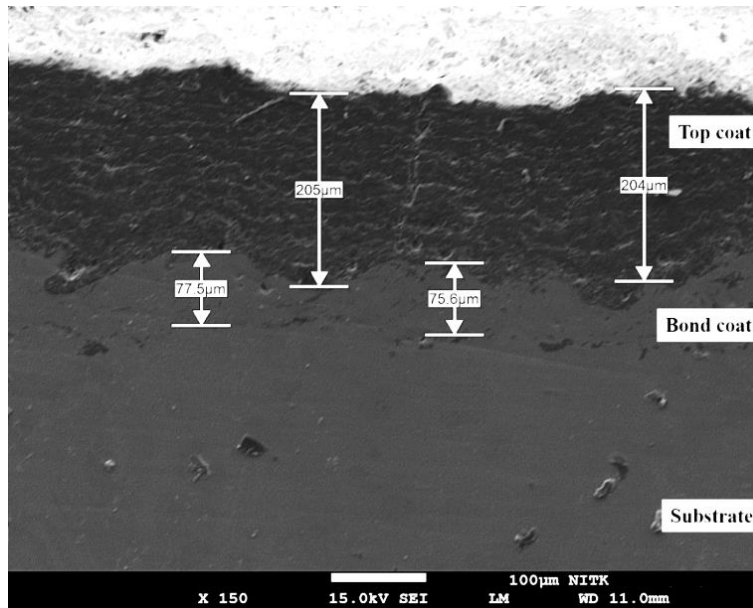


Figure 4.9 Cross-section of the developed TBC observed under SEM

Elemental mapping was performed on the as-coated surface to examine the distribution of elements within the morphology. As shown in Figure 4.10, a uniform distribution of elements Sm, Sr, Al, and O was ascertained on the surface. The composition measured in electron dispersive spectroscopy (EDS) of the cross-section in different coating layers is shown in Table 4.1.

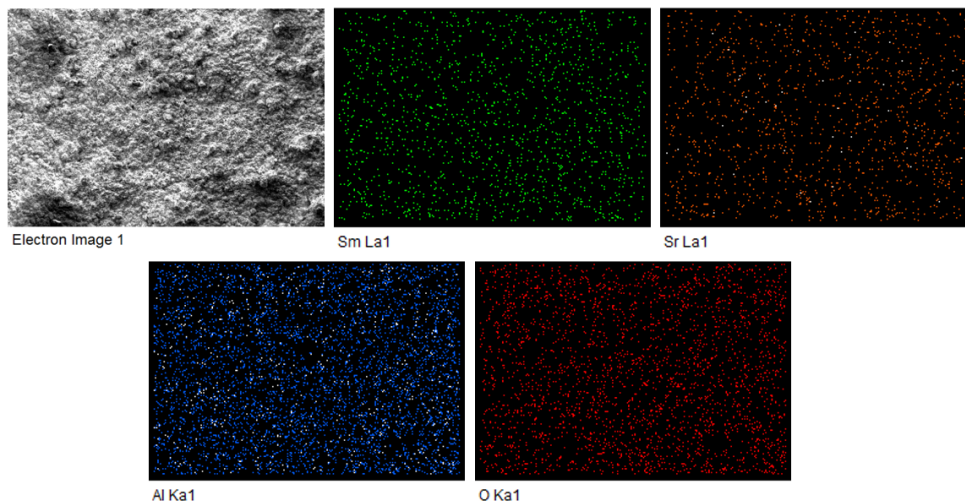


Figure 4.10 Elemental mapping of as-coated surface

Table 4.1 Cross-sectional composition of developed composite coatings (wt.%)

Top coat region	Sm	Sr	Al	O
	17.5	4.9	39.3	38.0
Bond coat region	Ni	Cr	Al	Y
	65.3	22.5	10.8	1.2

The profilometric image of the as-coated sample is shown in Figure 4.11. A surface with  $R_a = 6.0 \mu\text{m}$  consisting of peaks of unmolten particles on the surface was observed.

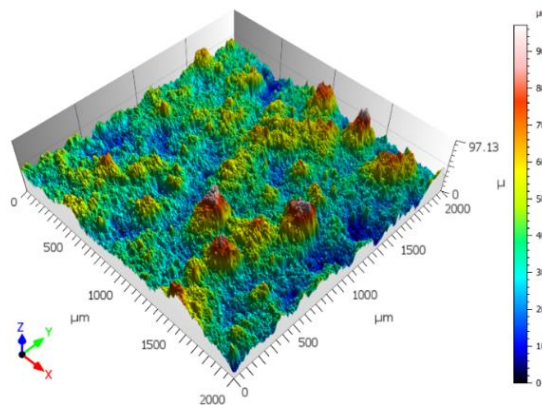
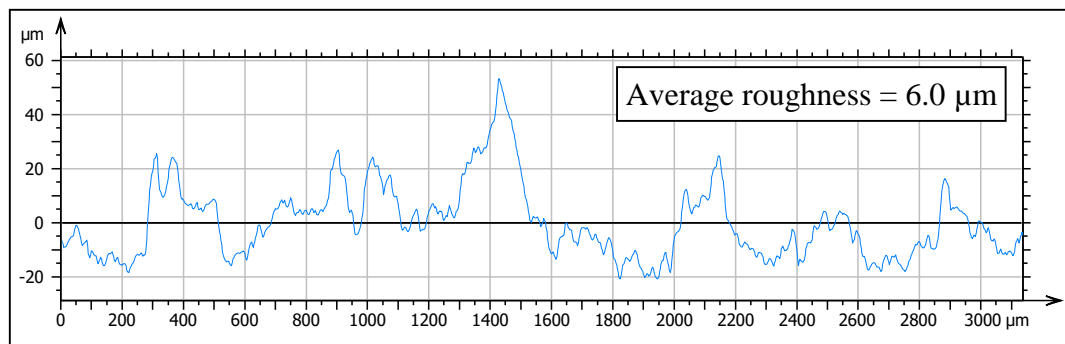


Figure 4.11 Surface roughness profile and profilometric image of as-coated sample

### *X-ray Diffraction studies*

The XRD pattern of the as-sprayed coatings is shown in Figure 4.12. The as-sprayed top coat consisted of three phases such as rhombohedral structured  $\alpha\text{-Al}_2\text{O}_3$ , cubic structured  $\gamma\text{-Al}_2\text{O}_3$ , and tetragonal  $\text{Sm}_2\text{SrAl}_2\text{O}_7$ . The SSA retained the exact phases after coating, while a major fraction of  $\alpha\text{-Al}_2\text{O}_3$  got transformed to  $\gamma\text{-Al}_2\text{O}_3$  upon spraying. Interestingly, no noticeable phase changes were observed in the SSA system, which agrees with the available literature (Baskaran and Arya 2018). The

quantification of phases in XRD showed 29.5 % of  $\text{Sm}_2\text{SrAl}_2\text{O}_7$ , 53.8 % of  $\gamma\text{-Al}_2\text{O}_3$ , and 16.7 % of  $\alpha\text{-Al}_2\text{O}_3$ . The presence of a similar dual-phase alumina was reported where the thermal spraying converted  $\alpha\text{-Al}_2\text{O}_3$  to  $\gamma\text{-Al}_2\text{O}_3$  (Krishnamurthy et al. 2012). The APS coated and detonation gun sprayed alumina also contained dual phase with  $\alpha\text{-Al}_2\text{O}_3$  and  $\gamma\text{-Al}_2\text{O}_3$ . The  $\gamma\text{-Al}_2\text{O}_3$  phase has been formed during the thermal spraying of the powder through the plasma spray technique. The gamma alumina phase forms upon a high solidification rate during coating deposition (Psyllaki et al. 2001). Upon impingement on a comparatively cold substrate, the droplets lose their kinetic energy and experience an ultra-rapid solidification. The  $\gamma\text{-Al}_2\text{O}_3$  nucleates easily from melt than  $\alpha\text{-Al}_2\text{O}_3$ . The gamma phase has a lower liquid-solid interfacial energy. So homogeneous nucleation at considerable undercooling results in the formation of gamma phase rather than alpha alumina. The formation of metastable gamma and theta phases upon rapid melting and solidification was reported by earlier researchers (Fiedler 1984; Karabaş et al. 2017; Psyllaki et al. 2001). It is claimed that the application of hydrogen as auxiliary gas tends to form a gamma phase with FCC structure (Tarasi et al. 2010).

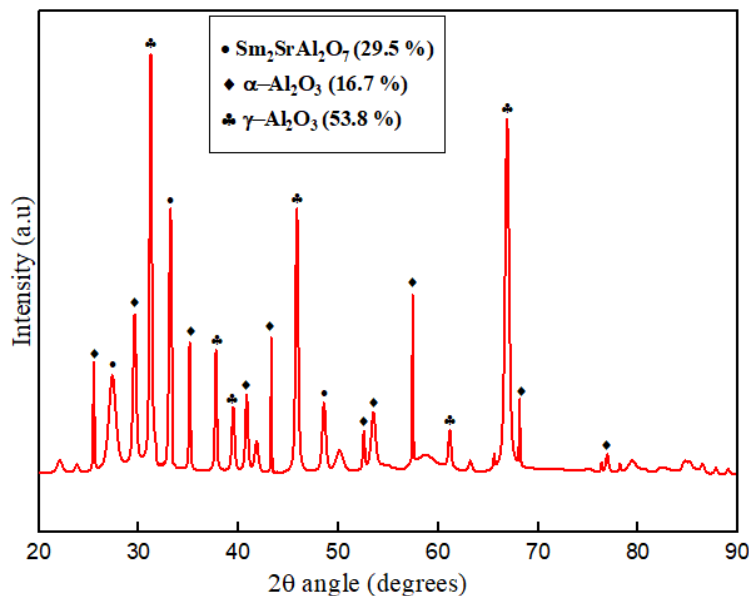


Figure 4.12 XRD pattern of the as-coated composite sample surface

In general, the alpha phase shows higher stability than the gamma alumina. Generally, an alpha phase has been reported to form when the deposits are made on preheated substrates. Reducing the distance between the gun and deposition surface, and thereby

increasing the temperature of the latter tends formation of alpha directly from the melt. The alpha phase, with high hardness and strength, offers good resistance against acid, alkali, and heat, while the gamma phase is highly wear-resistant (Busca 2014; Fiedler 1984; Karabaş et al. 2017).

#### 4.2.1 EBSD analysis of developed coatings

The electron backscatter diffraction (EBSD) of the top coat was carried out on the cross-section to analyze the phase fractions and phase distributions over the microstructure. The phase map and grain distribution, as shown in Figure 4.13 (a and b) unveiled a perfectly uniform distribution of phases  $\text{Sm}_2\text{SrAl}_2\text{O}_7$ ,  $\text{Y-Al}_2\text{O}_3$ , and  $\alpha\text{-Al}_2\text{O}_3$  (No segregations or isolations of phases were identified) upon melting and solidification during coating. The phase fractions observed were close to the values from the XRD analysis. The as-coated samples showed a finer average grain size of  $0.037\ \mu\text{m}$  (37 nm). From the distribution plot, about 98 % of the grains possessed a single size of  $0.03\ \mu\text{m}$  in the as-coated condition (Figure 4.13-b).

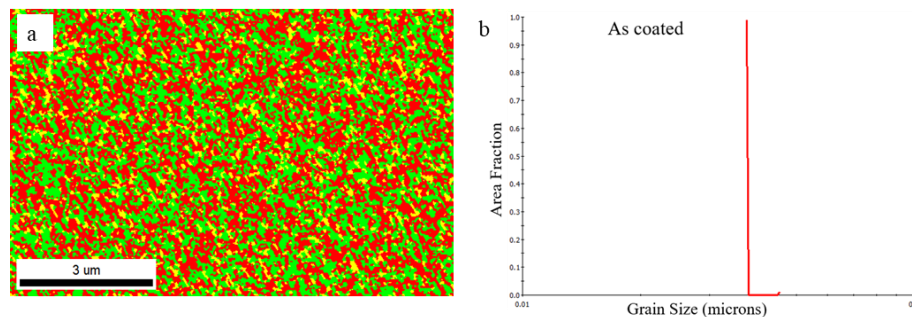


Figure 4.13 a) Phase map showing distribution of phases and b) grain size distribution of as-coated samples

Further, the inverse pole figure, as in Figure 4.14, suggests that there is no preferred orientation in the system in as-sprayed condition. Similar coating structures with random orientation are reported in atmospheric plasma sprayed and axial suspension plasma sprayed 8YSZ thermal barrier coatings (Klement et al. 2017; Tao et al. 2020).

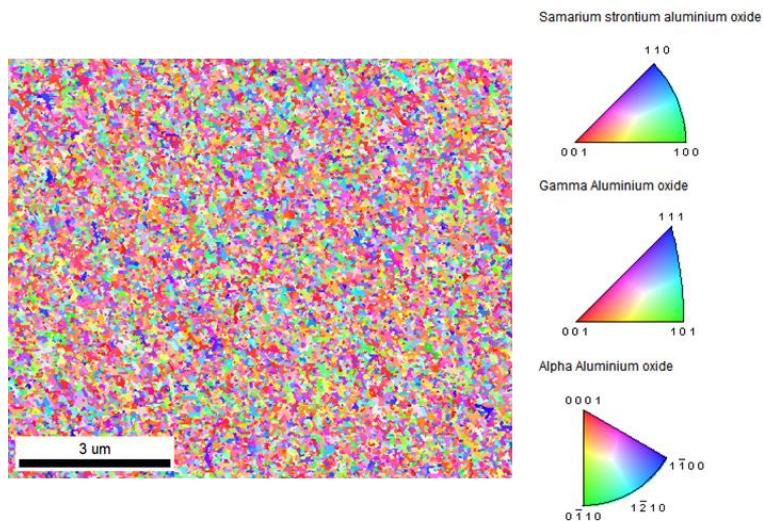


Figure 4.14 Inverse pole figure of as-coated samples

#### 4.2.2 Mechanical properties of as-coated samples

Nanoindentation tests were carried out on the as-coated samples to examine the mechanical properties of the system, using a Berkovich diamond indenter of 20 nm tip. The applied load and displacement in depth direction were constantly monitored. The load depth curves of the as-coated sample are shown in Figure 4.15. Measurements were taken on multiple locations and an average hardness of 11.5 GPa was obtained in as-coated samples. Young's modulus value of the coatings was determined to be 152 GPa. The observed values of the composite coatings were in concurrence with other conventional coating materials, which is discussed in later sections.

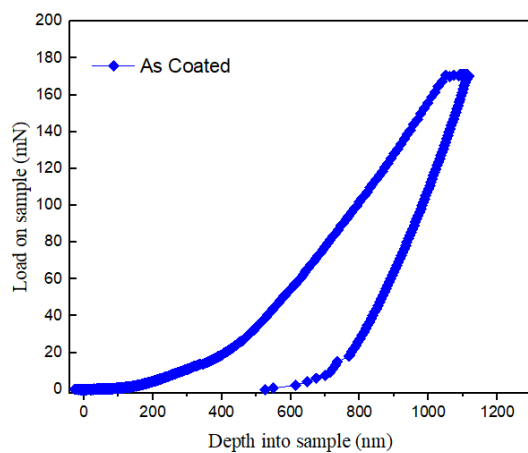


Figure 4.15 Load displacement curves for as-coated samples measure by nanoindentation



## 5 Oxidation, hot corrosion, and erosion behavior of as-coated samples

### 5.1 Isothermal oxidation behavior of as-coated samples

The developed samples were heated to 1100 °C at a heating rate of 6 °C/min and held isothermally. The samples exposed to an oxidation atmosphere at 1100 °C were examined every 30 h, to assess the surface conditions. The weight gain and surface XRD patterns were recorded to trail the oxidation mechanisms. The samples showed spallation tendencies after 150 h at 1100 °C, and the oxidation test was terminated. The cross-sectional analysis of the samples was performed in scanning electron microscopy to examine the oxide formation.

#### 5.1.1 Surface examination of oxidized samples

The surface observation of the oxidized samples in SEM (Figure 5.1) showed surface pores on the sample, which was not noticeable in visual inspection. The effect of these pores on the oxidation behavior of the samples is investigated. A higher magnification observation as shown in Figure 5.2 revealed the crack formation in the coatings upon high-temperature exposure.

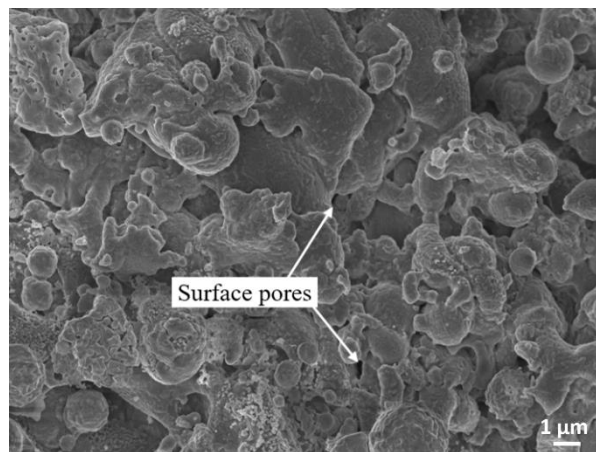


Figure 5.1 Surface image of as-coated samples after isothermal oxidation at 1100 °C for 150h

After high-temperature exposure, upon cooling to ambient temperature, the sample surface experiences tensile stress which initiates cracks on the surface (Kokini et al. 1996). The microcracks existing on the surface are reported to enlarge during high-

temperature oxidation and cycling, due to thermal expansion and contraction. Generally, in thermal sprayed TBCs, horizontal cracks, and minor vertical cracks are observed, where the horizontal cracks are often interlaminar, originating from the shrinkage of molten splats (Song et al. 2017, 2019).

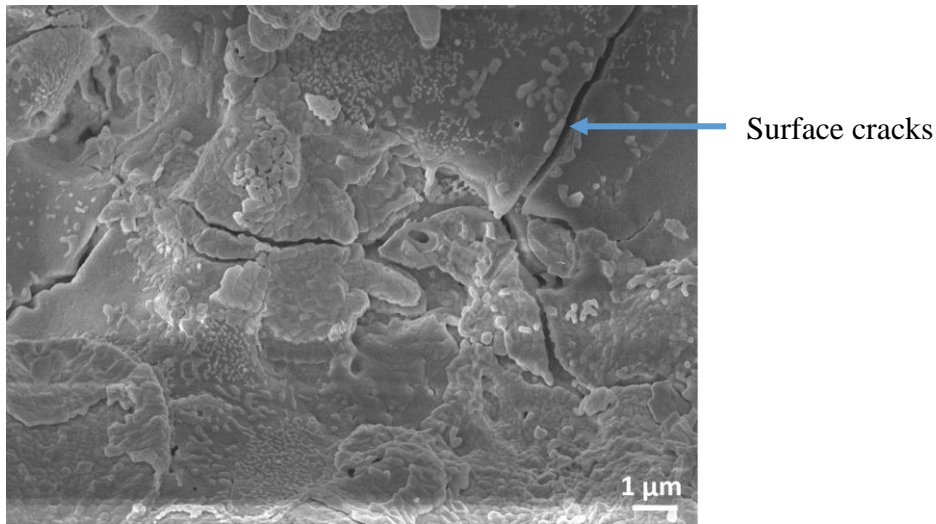


Figure 5.2 Magnified surface image of as-coated samples after oxidation test at 1100 °C for 150 h

The EDS analysis of the sample surface after oxidation (Figure 5.3) measured the compositions of Sm, Sr, Al, and O as 13.4 %, 4.2 %, 38.6 %, and 43.7 %, respectively. An increase in oxygen content can be noticed from the as-coated composition, which is attributed to the oxygen ingress and formation of oxides.

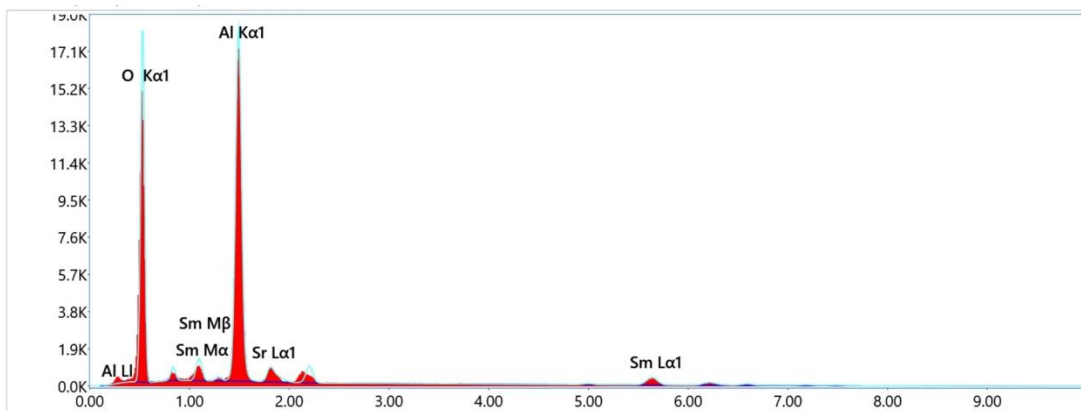
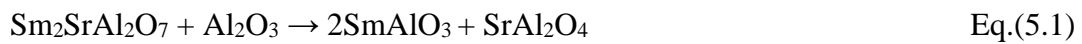


Figure 5.3 EDS analysis of the surface after exposure at 1100 °C for 150 h

The X-ray diffraction patterns of the as-coated sample surfaces were recorded after each 30 h exposure at 1100 °C, as shown in Figure 5.4. The surface XRD of the samples under different exposure times showed only a marginal difference. For all durations, the peaks of alpha alumina, gamma alumina, and SSA were observed. Identical to the as-sprayed coatings, the gamma phase dominated over the alpha phase on the oxidized surface. The rate of phase transformation from metastable phases to  $\alpha$ -Al<sub>2</sub>O<sub>3</sub> is generally lower for crystalline alumina coatings (Leushake et al. 1997).

Besides the top coat phases, the dissociation elements SmAlO<sub>3</sub>, SrAl<sub>2</sub>O<sub>4</sub>, and Sm<sub>2</sub>O<sub>3</sub> were observed on the surface. From the XRD and EDS analysis, the formation of SmAlO<sub>3</sub> and SrAl<sub>2</sub>O<sub>4</sub> upon high-temperature exposure can be assumed as per the balanced Eq.(5.1).



The compound SmAlO<sub>3</sub> can also form from the dissociation of samarium strontium aluminate in the composite top coat, as shown in Eq.(5.2).



Even though strontium oxide (SrO) possesses a high melting point (2500 °C), no peaks are detected in the XRD, proving the presence. This suggests the possible reaction of SrO with Al<sub>2</sub>O<sub>3</sub> upon continuous interaction about 12 h to form SrAl<sub>2</sub>O<sub>4</sub> as shown in Eq.(5.3).



The SrAl<sub>2</sub>O<sub>4</sub> formation as per Eq.(5.3) occurs at temperatures below and around 1100 °C. The formed SrAl<sub>2</sub>O<sub>4</sub> is stable above 1100 °C, and any further transformation requires calcination above 1250 °C. The samarium mono aluminate (SmAlO<sub>3</sub>) with a high melting point (2090 °C) was seen on all the samples.

Earlier investigations on single-layer SSA coatings reported the presence of nickel and other spinel oxides on the surface, which was not observed in the developed composite system (Baskaran and Arya 2017). The absence of these mixed oxides eliminates the chances of possible diffusion of substrate and bond coat elements to the top coat

surface. As the top coat elements and dissociation elements are mostly oxides, they resist further interaction with oxygen.

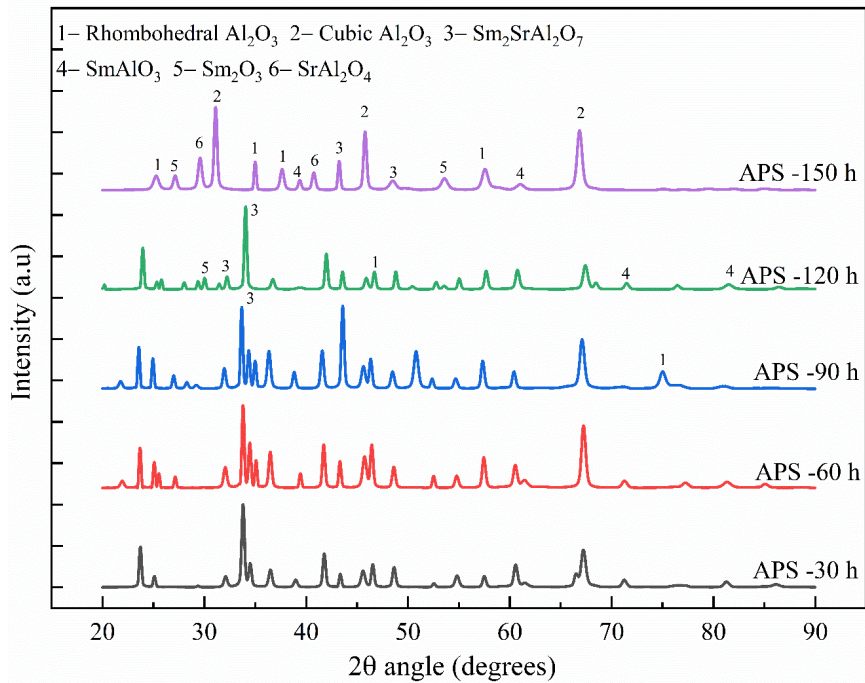


Figure 5.4 XRD patterns of as-coated samples after oxidation for different durations

### 5.1.2 Cross-section analysis and TGO growth

In thermal barrier coatings, in the presence of a bond coat, the oxygen diffused through the top coat tend to react with bond coat elements, forming the TGO layer. The extent of the reactions generally depends on the resistance of the top coat microstructure against oxygen diffusion (Huang et al. 2020).

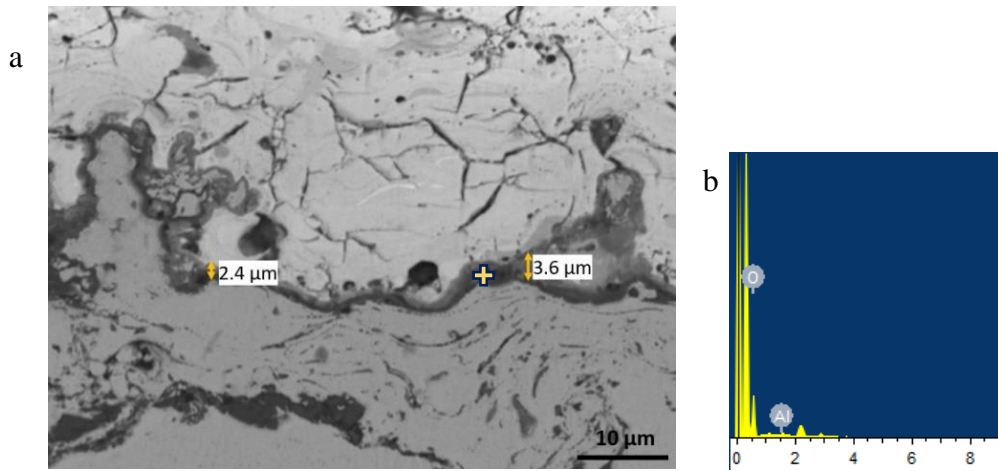


Figure 5.5 a) Cross-section of developed coatings exposed to 30 h oxidation at 1100 °C, b) EDS mapping of TGO region

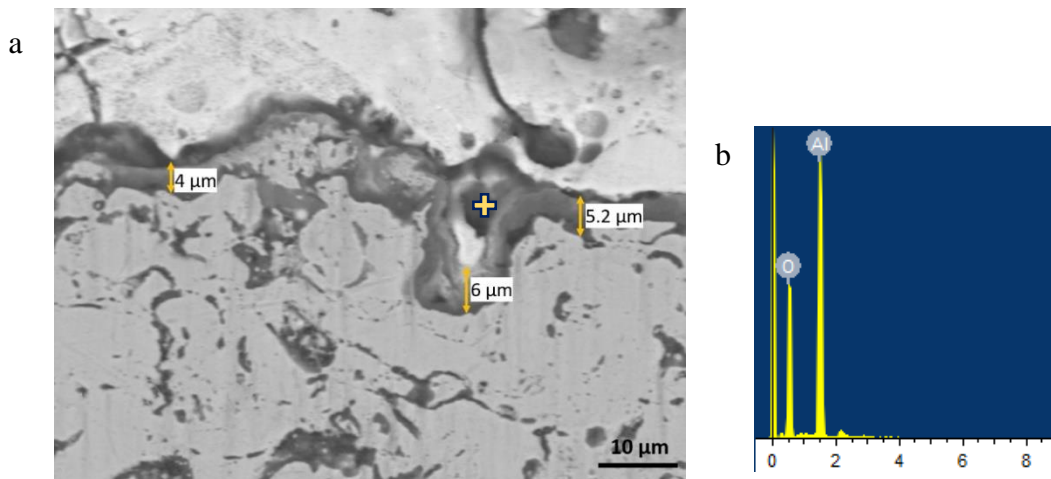


Figure 5.6 a) Cross-section of developed coatings exposed to 90 h oxidation at 1100 °C, b) EDS mapping of TGO region

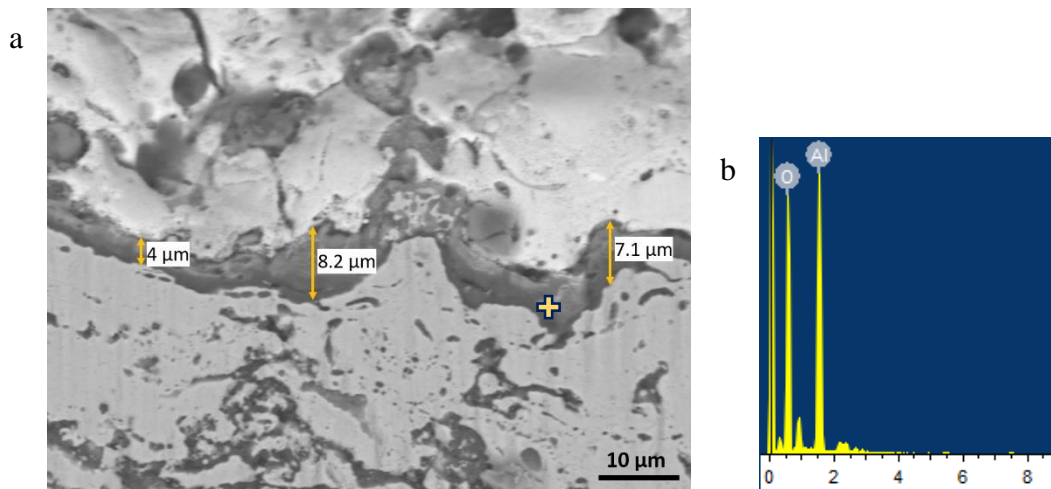


Figure 5.7 a) Cross-section of developed coatings exposed to 150 h oxidation at 1100 °C, b) EDS mapping of TGO region

The samples exposed to various durations were cross-sectioned and examined to understand the interfacial mechanisms. The cross-section of the as-coated samples after exposure to 30 h, 90 h, and 150 h durations at 1100 °C are shown in Figure 5.5, Figure 5.6, and Figure 5.7, respectively. The thermally grown oxide layer was formed at the interface through the reaction of oxygen with the metallic bond coat elements, most commonly aluminium. TGO may act as a protective barrier preventing further oxygen diffusion towards the bond coat. The cross-section analysis of samples showed a nearly continuous TGO formation at the interface. The EDS examination of the TGO layer detected the exclusive presence of Al and O, indicating a high purity of the TGO layer. The measurements of TGO layers at multiple locations were taken. The observed thickness and composition of the selected TGO regions as in the microstructure are listed in Table 5.1.

Table 5.1 Thickness and composition of the TGO region observed in as-coated samples after oxidation

Time of exposure (h)	TGO thickness (μm)	Al (wt. %)	O (wt. %)
30	3.0	53.7	46.3
90	4.8	51.9	48.1
150	6.2	49.5	50.5

It can be pointed out that the TGO thickness is increasing with increasing isothermal exposure. The average oxide thickness varied from 3  $\mu\text{m}$  to 6.2  $\mu\text{m}$  in as-coated samples after exposing them to 1100  $^{\circ}\text{C}$  for 30 h and 150 h, respectively. The growth of oxide scale thickness was accompanied by the development of stress, which upon reaching a threshold value, led to spallation. The behavior of the interface depends on the composition of the oxide scale formed. A pure  $\text{Al}_2\text{O}_3$  TGO is the most preferred oxide, because of its protective nature and nearly zero oxygen permeability (Liu et al. 2016). The least thermodynamic activity required for  $\text{Al}_2\text{O}_3$  formation makes the reaction dominant in the formation of other oxides (Nath et al. 2014). It is worth mentioning that no noticeable cracks were present within the uniform TGO. A cracked TGO layer may lead to further oxygen diffusion, resulting in further internal oxidation of bond coat elements (Saremi et al. 2008).

It is well known that the alumina addition brings down porosity, reducing oxygen infiltration through the top coat. Previous research reports reduced oxide growth with increasing alumina content in the top coat (Avci et al. 2020). Generally, a large amount of spinel oxides such as  $\text{NiO} \cdot \text{Cr}_2\text{O}_3$ , which grows rapidly, is formed at the interface. The bond coat elements, like Ni and Cr, tend to migrate to the interface when the Al concentration in the bond coat region in proximity of the interface reduces upon  $\text{Al}_2\text{O}_3$  formation. With a continuous heat treatment time,  $\text{Al}_2\text{NiO}_4$  phase spinel formation causes stress development in YSZ coatings, leading to crack formation parallel to the coating surface (Nath et al. 2014; Song et al. 2017).

Table 5.2 Composition of sample cross-section after isothermal oxidation tests for 150 h duration (wt.%)

	Oxidized samples	Sm	Sr	Al	O	
Top coat region	As-coated	12.5	4	36.9	46.5	
		Ni	Cr	Al	Y	O
Bond coat region	As-coated	60.1	20.8	8	1.1	10

The composition of different regions in cross-section after isothermal oxidation tests for 150 h duration is included in Table 5.2. In the developed system, no significant spinels were observed at the interface. This may be due to the higher alumina content in the composite top coat and the preferential oxidation of aluminium in the bond coat. The grain boundary diffusivity of oxygen increased with temperature, showing a diffusivity of  $7.241 \times 10^{-28} \text{ m}^2/\text{s}$  at 1100 °C. An activation energy requirement of 467 kJ/mole was reported for the surface diffusion of oxygen into bulk (Smialek et al. 2013). Upon continuous exposure at high temperatures, the high-purity polycrystalline alumina formed at the interface offers higher oxygen shielding effect protecting the bond coat from further oxidation (Avci et al. 2020). The samples showed spallation at the interface after 150 h of exposure near the top coat bond coat interface region, within the proximity of the TGO formed.

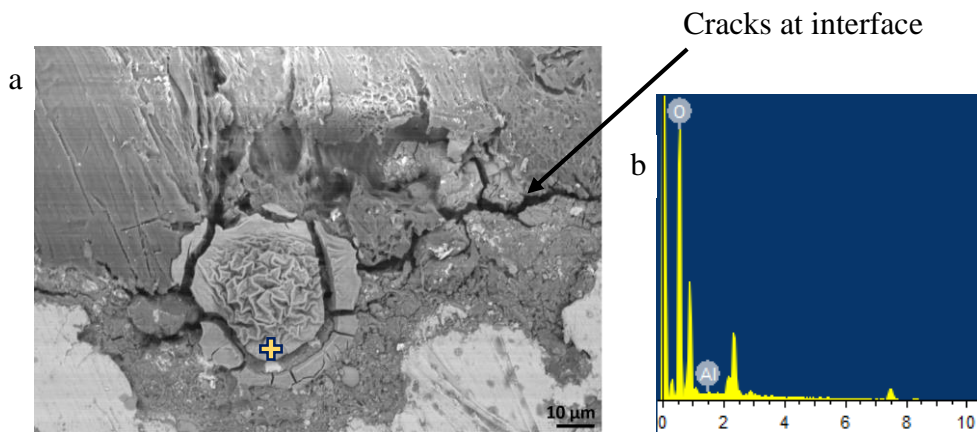


Figure 5.8 a) High magnification view of lump formation at interface of as-coated sample after oxidation tests b) EDS analysis of lump

Interestingly, as shown in Figure 5.8, an oxide lump near the interface in the top coat region was observed in the as-coated samples after 150 h of exposure at 1100 °C. With a continuous increment in TGO thickness, the stress level gets higher, suppressing further oxide layer formation. Cracks appear in the proximity, perpendicular to the TGO layer, if the cracks exceed a certain value. In the areas of lump formation, perpendicular cracks and horizontal delamination at the interface were seen. The presence of the TGO lump may have created interfacial stress in the system, leading to severe cracking in the adjacent regions. The EDS analysis of the lump showed the only presence of Al and O, pointing to alumina formation with a flower-like microstructure. No spinel oxides were



detected near the TGO lump, which otherwise develops much higher stresses. The stress developed also depends on the geometry of the oxides, along with the dependence on scale thickness (Song et al. 2017).

The minor cracks around the oxide lump would have connected to form the major crack. Various efforts have been made to prevent stress formation and subsequent spallation at the interface. Rhenium-based diffusion barriers on the substrate have shown a higher spallation resistance and the least oxide layer thermal stresses (Fu et al. 2022).

### 5.1.3 Kinetics of oxidation

In general, the bond coat undergoes oxidation through mechanisms of ionic movement of oxygen and oxygen ingress via existing pores and defects in the top coat. These oxide formations result in weight gain in the system. Figure 5.9 shows the weight gain per unit area of the samples exposed at 1100 °C for different durations. The graph can be divided into two regions, an initial region with a higher weight gain and a sluggish weight gain region followed. The higher initial weight gain is due to the easy availability of aluminium in the bond coat and the absence of any protective layer at the interface. The kinetics become sluggish, with the progress of oxidation reactions and the associated growth of the protective alumina scale. Similar trends of oxidation kinetics have been reported by single-layered and functionally graded YSZ coatings (Nath et al. 2014). The plot shows that the oxidation reaction and subsequent weight gain follow a parabolic law, as depicted by Wagner's theory.

$$\frac{\Delta m}{A} = (k_p \times t)^{1/2} \quad \text{Eq.(5.4)}$$

Where  $\frac{\Delta m}{A}$  is the weight gain per unit area after an exposure time of  $t$  (s), and  $k_p$  is the parabolic rate constant. The parabolic rate constant ( $k_p$ ) of the oxidation reaction is determined from the slope of the linear line obtained by plotting the square of weight gain per area vs exposure time as in Figure 5.10. The as-coated samples showed a parabolic rate constant of  $2.5 \text{ mg}^2\text{cm}^{-4}\text{s}^{-1}$ . The oxidation phenomenon that occurred is diffusion controlled, by oxygen diffusion through interconnected pores and cracks along the composite top coat. Earlier research on high-temperature oxidation has

reported similar parabolic behavior of coatings (Mrowec and Stoklosa 1974; Persson and Nygren 1992). From the variation in slopes, it can be seen that the oxidation weight gain becomes independent of time after 120 h of exposure. The variation in kinetics is due to a continuously decreasing oxygen permeability with exposed time. The specific permeability of oxygen in an alumina matrix increases with temperature. Also, past researches report a lower oxygen permeability in alumina than in zirconia-based coatings. In the TBC system, the direct transport of oxygen through the composite top coat dominates the ionic diffusion (Fox and Clyne 2004).

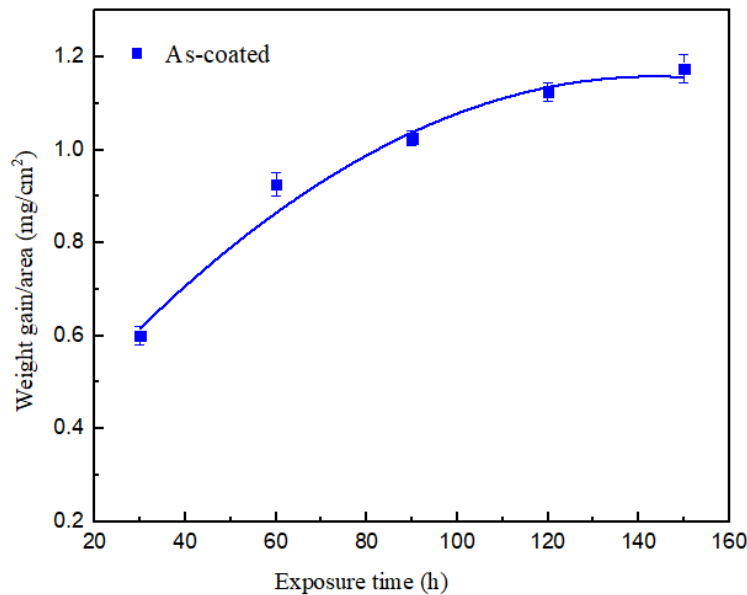


Figure 5.9 Weight gain per unit area of as-coated samples exposed to oxidation test at 1100 °C for different durations

The single-layer  $\text{Sm}_2\text{SrAl}_2\text{O}_7$  coatings showed a similar parabolic trend in weight gain when exposed to 1100 °C. The single-layer SSA offered a better performance than YSZ coatings after a pre-oxidation for 20 h at 1050 °C (Baskaran and Arya 2017). In the developed  $\text{Al}_2\text{O}_3 - \text{Sm}_2\text{SrAl}_2\text{O}_7$  composite coatings, the  $\gamma$ - $\text{Al}_2\text{O}_3$  phase with a higher porosity dominated the  $\alpha$  phase upon coating. The retention of the higher  $\alpha$ - $\text{Al}_2\text{O}_3$  phase may offer more resistance to oxidation, by its higher density than  $\gamma$ - $\text{Al}_2\text{O}_3$ . In general, gamma alumina tends to transform into stable alpha alumina. It is to be noted that no major transformation of the gamma phase to the alpha phase was detected during oxidation. The extra ions present in the system tend to hinder the

transformation from alpha to gamma. The elements identified to block the transformation include Sr, La, Ba, Ca, Y, B, Ce, Er, and Cr (Andersson 2005). In the developed system, the presence of  $\text{Sr}^{2+}$  ions may have hindered the transformation from gamma to alpha.

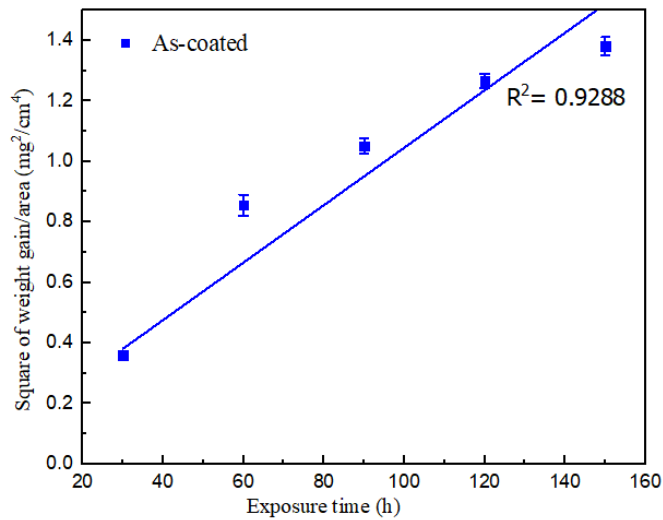


Figure 5.10 Square of weight gain per area of as-coated samples exposed to oxidation test at 1100 °C for different durations

#### 5.1.4 Electrochemical Impedance Spectroscopy (EIS) analysis of as-coated samples

The oxidation behavior and oxide formation can be clearly understood by examining the impedance response of the system. The electrochemical impedance of the developed coating system depends on microstructural factors such as open porosities, voids, and microcracks, which provides a functional path for the aqueous electrolytic solution. The resistance to electron flow is measured upon the application of an AC potential to the considered system. Figure 5.11 shows the typical EIS Nyquist plot and the equivalent circuit according to the as-coated system. The plot consists of a major portion of a semicircle. Similar plots have been reported in  $\text{Al}_2\text{O}_3/\text{YSZ}$  coatings (Amaya et al. 2009). The obtained response is fitted with the circuit elements; resistance and capacitance. The  $R_{\text{com}}$  and  $R_{\text{bc}}$  refer to the electrochemical resistance offered by the composite top coat and the metallic bond coat, respectively. Similarly, the  $C_{\text{com}}$  and  $C_{\text{bc}}$  refer to the capacitance of the composite top coat and the bond coat, respectively. As no pre-heating treatments were performed on the samples, no other elements were taken

into consideration. Only one relaxation process is observed in the as-coated samples, which is attributed to the interface charge transfer resistance at the electrolyte top coat interface. Identical behavior of as-sprayed coatings was reported by other researchers (Gomez et al. 2009). The as-coated top coat offered an impedance of 29067 Ohm.cm<sup>2</sup>. The obtained values of equivalent circuit elements calculated through fitting for as-coated samples is given in Table 5.3.

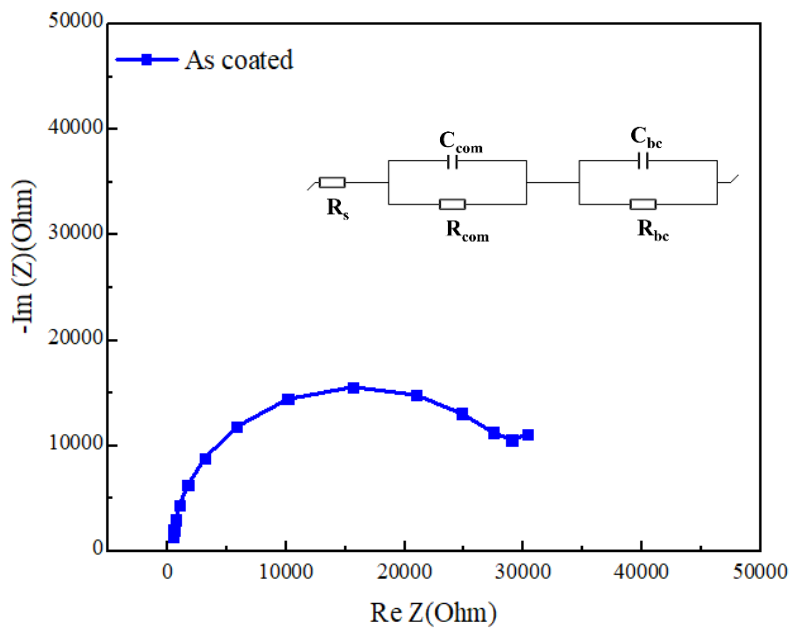


Figure 5.11 EIS Nyquist plot of as-coated samples

Table 5.3 Obtained values of equivalent circuit elements for as-coated samples

	$R_s$ (Ohm.cm <sup>2</sup> )	$C_{com}$ ( $\mu\text{F cm}^{-2}$ )	$R_{com}$ (Ohm.cm <sup>2</sup> )	$C_{bc}$ ( $\mu\text{F cm}^{-2}$ )	$R_{bc}$ (Ohm.cm <sup>2</sup> )
As-coated	480	0.242	29067	11.52	39876

## 5.2 Hot corrosion behavior of as-coated samples

Hot corrosion is one of the major failure mechanisms of thermal barrier coatings operating in high-temperature environments. The hot corrosion behavior of the developed 70 wt. %  $\text{Al}_2\text{O}_3$  - 30 wt. %  $\text{Sm}_2\text{SrAl}_2\text{O}_7$  composite thermal barrier coatings in critical aviation and marine conditions were analyzed in detail. The detailed approach to the hot corrosion test procedure is discussed in earlier sections. The hot corrosion samples were removed from the furnace after confirming failure through visual inspection. The resistances of the as-coated TBC samples (measured as h of exposure) in hot corrosion tests at 700 °C and 900 °C are shown in Figure 5.12. The observed difference in resistances of the samples in different conditions is assumed to be due to the varying interactions in each atmosphere. For a better understanding, the details of various corrosive conditions employed are summarised in Table 5.4.

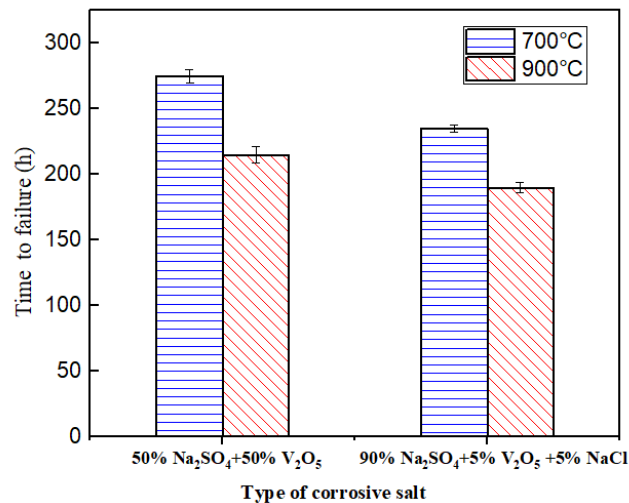


Figure 5.12 Graph showing the resistance of as-coated samples in the exposed conditions

At both temperatures, the samples exposed to 90 % wt.  $\text{Na}_2\text{SO}_4$  + 5 % wt.  $\text{V}_2\text{O}_5$  + 5 % wt. NaCl failed earlier than the samples exposed to 50 % wt.  $\text{Na}_2\text{SO}_4$  + 50 % wt.  $\text{V}_2\text{O}_5$  . A 14.5 % and 11.6 % lower resistance were observed in the samples exposed to marine conditions than in the samples at aviation conditions at 700 °C and 900 °C, respectively. The early failure in the presence of chlorides demanded a detailed examination of the failed samples. The photographs of the failed samples are shown in

Figure 5.13. In the as-coated samples, failure by partial chipping of the coatings was seen. A greenish discoloration in a few samples was noted, which is a reflection of sulphur reactions (Aust and Pons 2019). A detailed characterization of samples under each condition was performed to investigate the mechanism of failure in the developed composite thermal barrier coatings.

Table 5.4 Details of the corrosive conditions tested

Conditions simulated	Composition of corrosive salts (wt. %)			Exposed temperature
	Na <sub>2</sub> SO <sub>4</sub>	V <sub>2</sub> O <sub>5</sub>	NaCl	
Aviation (Salt-1)	50	50	0	700 °C 900 °C
Marine (Salt-2)	90	5	5	700 °C 900 °C

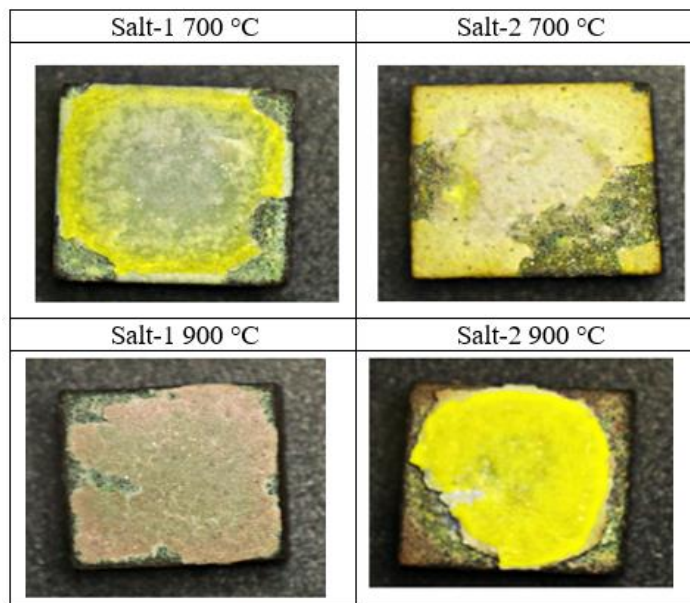


Figure 5.13 Photographs of as-coated samples after hot corrosion in various conditions

### 5.2.1 Hot corrosion of as-coated samples in 50 %wt. Na<sub>2</sub>SO<sub>4</sub> + 50 %wt. V<sub>2</sub>O<sub>5</sub> at 700 °C and 900 °C

The XRD patterns of the samples after exposure to corrosive salts were analyzed to identify the corrosion products and the underlying mechanisms of failure. It was noticed that the as-coated surface consisted of three phases,  $\alpha$ -Al<sub>2</sub>O<sub>3</sub>,  $\gamma$ -Al<sub>2</sub>O<sub>3</sub>, and Sm<sub>2</sub>SrAl<sub>2</sub>O<sub>7</sub>. Interestingly, no evidence of gamma phase was present in the surface XRD of the corroded samples. It can be assumed that the fraction of gamma phase present after plasma spraying was transformed to alpha phase upon continuous high-temperature exposure. In addition to the composite top coat peaks, new peaks appeared in the XRD of the samples after the hot corrosion test, pointing to the evolution of corrosion products amidst the test. The surface of the samples was analyzed using SEM to examine the composition and shape of the corrosion products formed under various conditions. The peeled areas presented different morphological features such as rod-like structures, cuboidal, and pyramid-like structures.

#### *Samples exposed at 700 °C*

Figure 5.14 shows the XRD pattern of the samples exposed to 50 %wt. Na<sub>2</sub>SO<sub>4</sub> + 50 %wt. V<sub>2</sub>O<sub>5</sub> at 700 °C. The surface XRD showed the presence of top coat powders Al<sub>2</sub>O<sub>3</sub>, Sm<sub>2</sub>SrAl<sub>2</sub>O<sub>7</sub> along with the corrosion products SmAlO<sub>3</sub>, SmVO<sub>4</sub>, AlVO<sub>4</sub>, SrAl<sub>2</sub>O<sub>4</sub>, and NaAlO<sub>2</sub>. A high-intensity peak of SmAlO<sub>3</sub> was observed, which is generally formed from the dissociation of Sm<sub>2</sub>SrAl<sub>2</sub>O<sub>7</sub>.

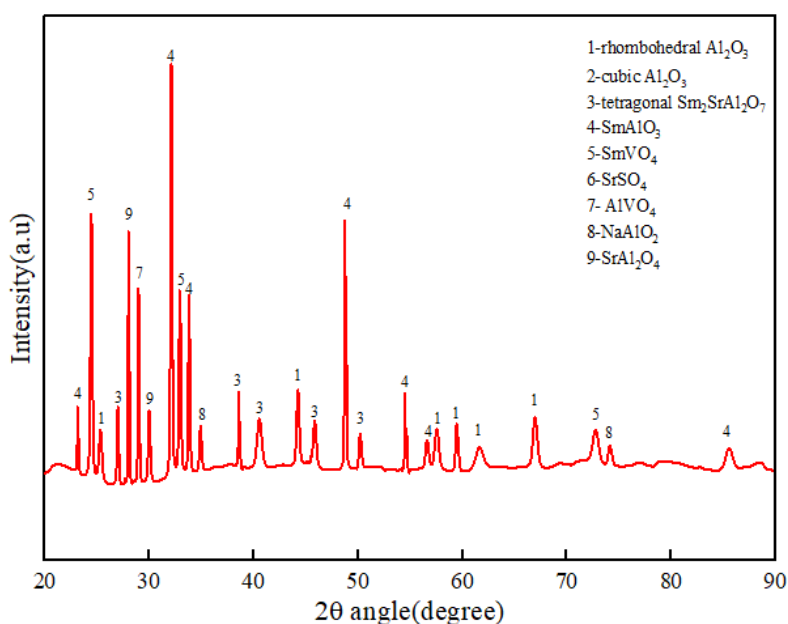


Figure 5.14 XRD pattern of as-coated sample exposed to 50 % wt  $\text{Na}_2\text{SO}_4$  + 50 % wt  $\text{V}_2\text{O}_5$  at 700 °C

The morphology of the sample exposed to 50 % wt.  $\text{Na}_2\text{SO}_4$  + 50 % wt.  $\text{V}_2\text{O}_5$  at 700 °C viewed under SEM is shown in Figure 5.15. The high magnification observations revealed the presence of  $\text{SmVO}_4$  rods. The chemical composition was analyzed using EDS on the selected area shown in Figure 5.15-b, and the obtained values are shown in Table 5.5. The  $\text{SmVO}_4$  was seen as rod-like structures, as vanadium oxides favor corrosion products with aciculate morphology. The  $\text{NaVO}_3$  formed from the reaction of  $\text{Na}_2\text{SO}_4$  and  $\text{V}_2\text{O}_5$  melts at about 610 °C and accelerates further reactions by infiltration (Jonnalagadda et al. 2017; Singh et al. 2007).

Table 5.5 Composition of the products formed on as-coated samples exposed to aviation conditions at 700 °C

	Sm	Sr	Al	O	Na	S	V	Cl
wt. %	56.4	0.00	0.00	24.50	0.00	0.00	19.10	0.00



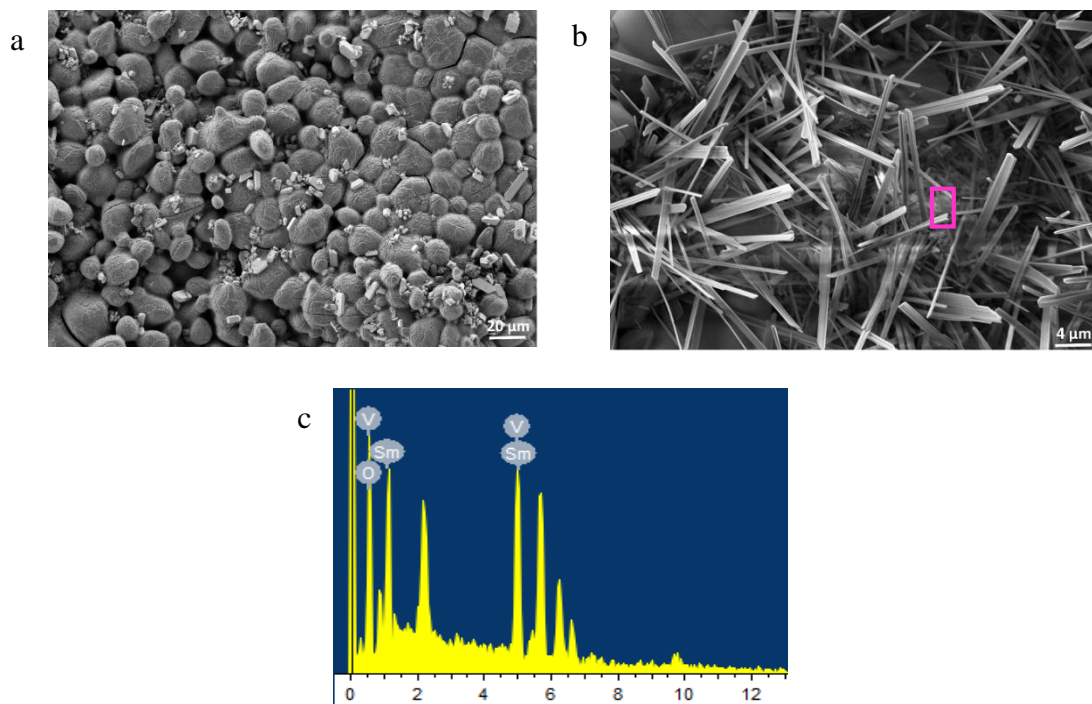


Figure 5.15 The SEM morphology of failed samples exposed to 50 % wt  $\text{Na}_2\text{SO}_4$  + 50 % wt  $\text{V}_2\text{O}_5$  at 700 °C showing  
 a) Low magnification image of corroded surface  
 b) High magnification image of the hot corrosion products formed on surface  
 c) EDS analysis of the corrosion products formed

### ***Samples at 900 °C***

The XRD pattern of the corroded surface in 50 % wt.  $\text{Na}_2\text{SO}_4$  + 50 % wt.  $\text{V}_2\text{O}_5$  at 900 °C is shown in Figure 5.16. The peaks corresponding to  $\text{Al}_2\text{O}_3$ ,  $\text{Sm}_2\text{SrAl}_2\text{O}_7$ ,  $\text{SmAlO}_3$ , and  $\text{SmVO}_4$  were observed. Interestingly, the  $\text{SmVO}_4$  peak showed the highest intensity revealing  $\text{SmVO}_4$  as the major corrosion product under the conditions exposed. It is to be noted that the compounds  $\text{AlVO}_4$ ,  $\text{NaAlO}_2$ , and  $\text{SrAl}_2\text{O}_4$  which were present at 700 °C were not seen at 900 °C. The SEM images of the samples after exposure at 50 % wt.  $\text{Na}_2\text{SO}_4$  + 50 % wt.  $\text{V}_2\text{O}_5$  at 900 °C is shown in Figure 5.17. The high-magnification images show the formation of cuboidal and pyramidal structures as corrosion products. The XRD peaks and the EDS analysis confirmed the products to be  $\text{SmVO}_4$ . The composition of the products in the marked region (Figure 5.17-b) is shown in Table 5.6. The  $\text{SmVO}_4$  was observed as a needle or rod-like structures at 700 °C, while it was larger cuboids at 900 °C. The difference in shape and size shows a higher growth of corrosion products at 900 °C, than at 700 °C. Block like  $\text{CeVO}_4$  and  $(\text{CeLa})\text{VO}_4$  is formed during vanadium-induced hot corrosion of  $\text{La}_2\text{Ce}_2\text{O}_7/\text{YSZ}$

coatings (Wang et al. 2015).

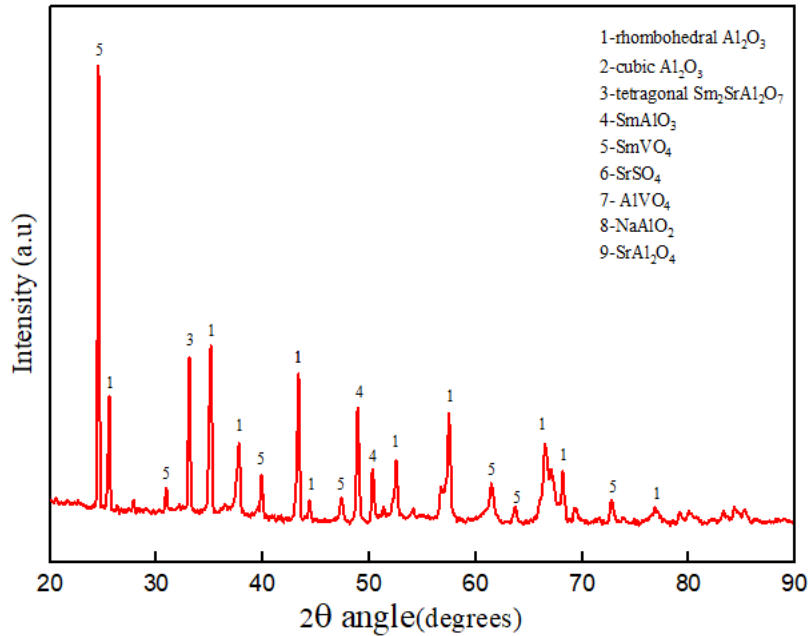


Figure 5.16 XRD pattern of sample exposed to 50 % wt  $\text{Na}_2\text{SO}_4$  + 50 % wt  $\text{V}_2\text{O}_5$  at 900 °C

In the case of aviation conditions with a higher vanadate content, at both temperatures,  $\text{SmVO}_4$  is the major corrosion product formed, which is stable up to 1440 °C. The formation of  $\text{SmVO}_4$  includes interactions of both sulphates and vanadates. Sodium sulphate and vanadium pentoxide react to form sodium metavanadate and sulphur trioxide.  $\text{SmVO}_4$  is formed when the sodium metavanadate interacts with  $\text{Sm}_2\text{O}_3$  from the top coat. Similar formation of  $\text{GdVO}_4$  and  $\text{LaVO}_4$  as random cuboids and rods, upon the reaction of gadolinium zirconate and lanthanum magnesium hexaaluminate TBC with  $\text{V}_2\text{O}_5$  was reported in other research (Jana et al. 2017; Jonnalagadda et al. 2017). The  $\text{LaVO}_4$  formation in  $\text{La}_2\text{Zr}_2\text{O}_7$  coatings occurs by a similar reaction between  $\text{La}_2\text{O}_3$  and  $\text{V}_2\text{O}_5$  (Yugeswaran et al. 2012).

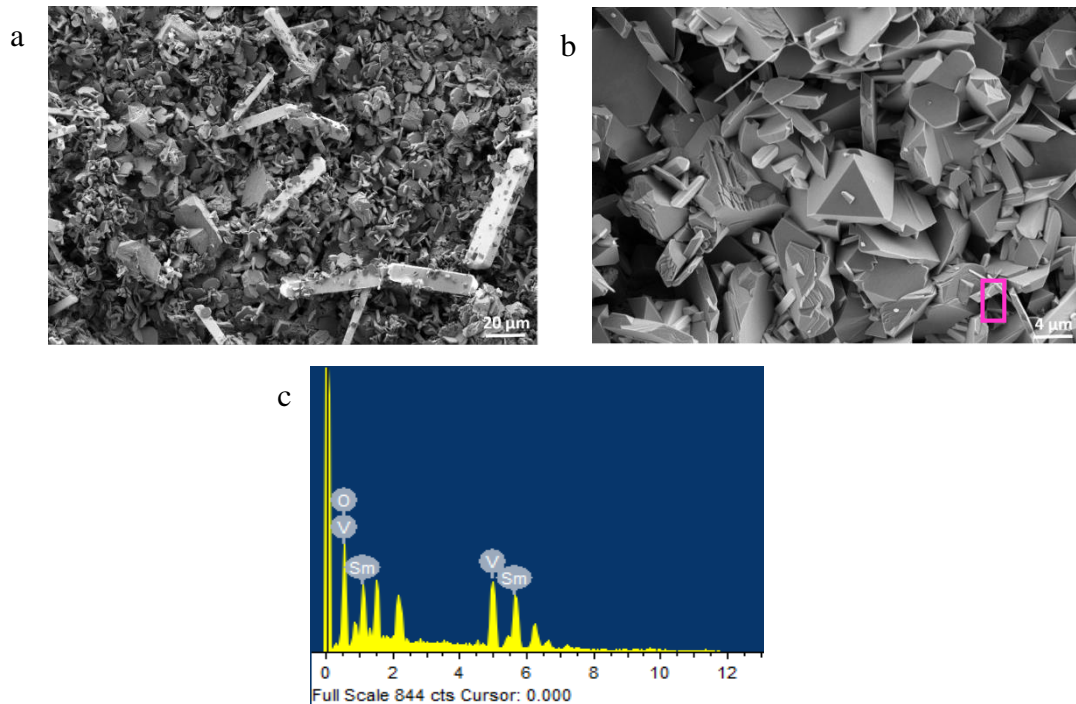


Figure 5.17 The SEM morphology of failed samples exposed to 50 % wt Na<sub>2</sub>SO<sub>4</sub> + 50 % wt V<sub>2</sub>O<sub>5</sub> at 900 °C showing  
 a) Low magnification image of corroded surface  
 b) High magnification image of the hot corrosion products formed on surface  
 c) EDS analysis of the corrosion products formed

Table 5.6 Composition of the products formed on as-coated samples exposed to aviation conditions at 900 °C

	Sm	Sr	Al	O	Na	S	V	Cl
wt. %	56.11	0.00	0.00	23.91	0.00	0.00	19.98	0.00

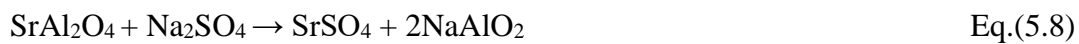
The possible mechanism of formation of SmVO<sub>4</sub> in aviation conditions is given as:



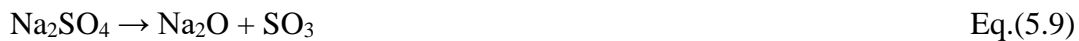
The presence of NaVO<sub>3</sub> is not generally desired in the environment. The formation of NaVO<sub>3</sub> in a conventional YSZ thermal barrier coating system has been reported to

accelerate the depletion of yttria from YSZ, by increasing the atomic mobility, causing coating failure. The significance of the corrosion mixture selected is the formation of NaVO<sub>3</sub> and its congruent melting around 610 °C (Jana et al. 2017). Conjointly, the NaVO<sub>3</sub> tends to form V<sub>2</sub>O<sub>5</sub> again with the evaporation of Na upon prolonged exposure.

In the samples that failed in aviation conditions at 700 °C, the presence of SrAl<sub>2</sub>O<sub>4</sub> also has been confirmed through XRD and EDS analysis. The SrAl<sub>2</sub>O<sub>4</sub> formed further reacts with Na<sub>2</sub>SO<sub>4</sub> to form SrSO<sub>4</sub> and 2NaAlO<sub>2</sub> as in Eq.(6.4).



The decomposition products of Na<sub>2</sub>SO<sub>4</sub> also lead to the formation of NaAlO<sub>2</sub>. The dissociation reactions of Na<sub>2</sub>SO<sub>4</sub> is already reported by researchers as shown in Eq.(5.9) (Afrasiabi et al. 2008; Baskaran and Arya 2018).



The decomposition of Na<sub>2</sub>SO<sub>4</sub> results in the formation of Na<sub>2</sub>O and SO<sub>3</sub>, in which Na<sub>2</sub>O reacts with Al<sub>2</sub>O<sub>3</sub> to form NaAlO<sub>2</sub>, which aids in slowing down further hot corrosion of alumina (Afrasiabi et al. 2008; Baskaran 2018). The formation of NaAlO<sub>2</sub> may have aided the sample's 17 % higher resistance than salt 2 at the same temperature.

In the case of aviation atmosphere considered, AlVO<sub>4</sub> is formed only at 700 °C. Generally, aluminium possesses a lower reactivity with vanadate salts. AlVO<sub>4</sub> has been formed on prolonged exposure to the abundance of aluminium, which reflects the possibility of the leaching of aluminium from the matrix. A similar formation of rod-like YVO<sub>4</sub> from yttria leaching can be observed in conventional YSZ samples (Baskaran and Arya 2018).

Figure 5.18 shows the Raman spectrum of as-coated samples after hot corrosion tests at 50 % wt. Na<sub>2</sub>SO<sub>4</sub> + 50 % wt. V<sub>2</sub>O<sub>5</sub> at 700 °C and 900 °C. In the spectrum, the high-intensity peak of SmVO<sub>4</sub> at 877 cm<sup>-1</sup>(O-Sm-O) and 814 cm<sup>-1</sup> (Sm-O) are visible.

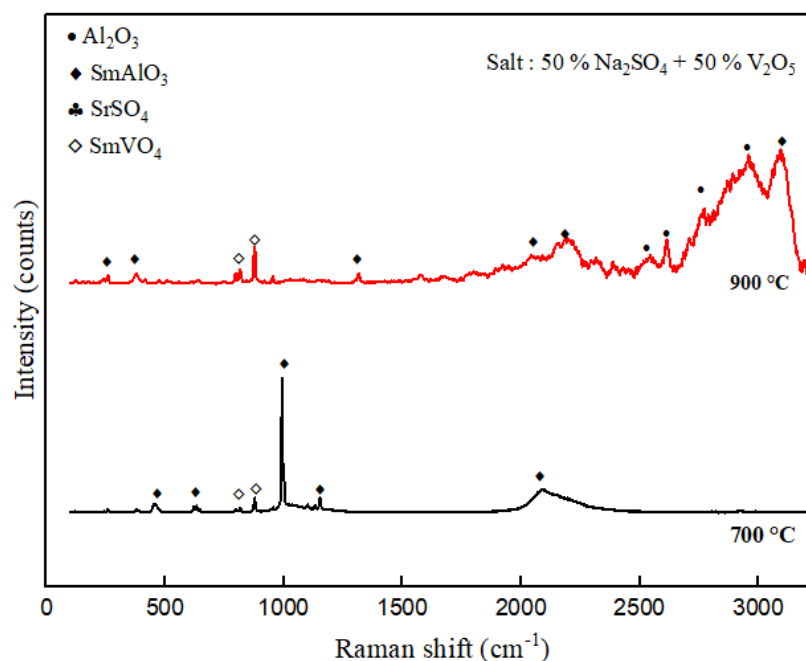


Figure 5.18 Raman spectrum of as-coated samples after hot corrosion tests at 50 % wt Na<sub>2</sub>SO<sub>4</sub> + 50 % wt V<sub>2</sub>O<sub>5</sub> at 700 °C and 900 °C

### 5.2.2 Hot corrosion of as-coated samples in 90 %wt. Na<sub>2</sub>SO<sub>4</sub> + 5 %wt. V<sub>2</sub>O<sub>5</sub> + 5 wt.% NaCl at 700 °C and 900 °C

#### *Samples at 700 °C*

From the time to failure plots, as shown in Figure 5.12, the samples exposed to marine conditions (90 % wt. Na<sub>2</sub>SO<sub>4</sub> + 5 % wt. V<sub>2</sub>O<sub>5</sub> + 5 % wt. NaCl) failed early than the samples exposed to aviation conditions. The XRD pattern of the peeled-off samples exposed to marine conditions at 700 °C is shown in Figure 5.19. The XRD showed peaks corresponding to Al<sub>2</sub>O<sub>3</sub>, SSA, SmAlO<sub>3</sub>, SmVO<sub>4</sub>, and SrSO<sub>4</sub>. SmAlO<sub>3</sub> being a dissociation product (also observed in oxidation conditions at 1100 °C), the major corrosion products are only SmVO<sub>4</sub> and SrSO<sub>4</sub>. The higher sulphate content in the marine corrosive salt may have led to the formation of SrSO<sub>4</sub>. The high magnification images of the corrosion products showed up irregularly shaped SrSO<sub>4</sub>, with composition as given in Table 5.7. The surrounding morphology revealed a relatively porous microstructure compared to other failed samples (Figure 5.20).

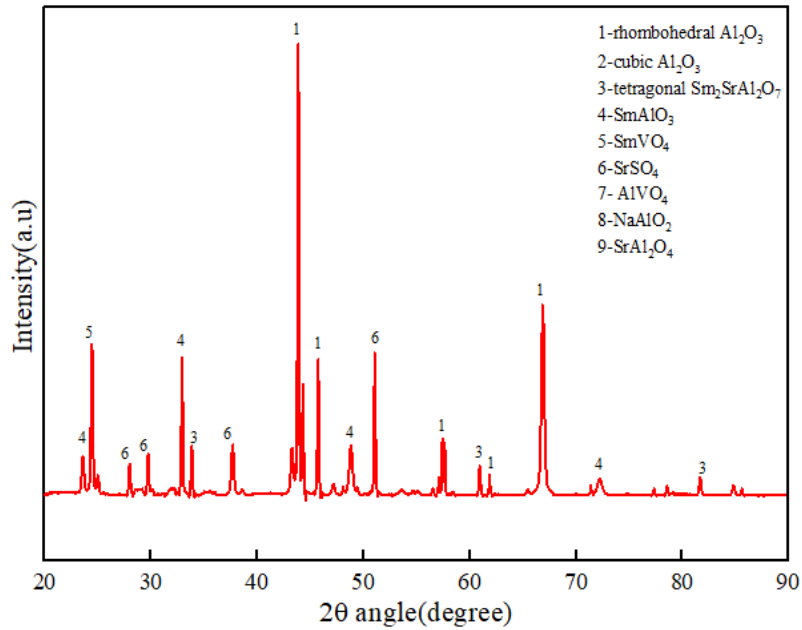


Figure 5.19 XRD pattern of sample exposed to 90 % wt  $\text{Na}_2\text{SO}_4$  + 5 % wt  $\text{V}_2\text{O}_5$  + 5 % wt  $\text{NaCl}$  at 700 °C

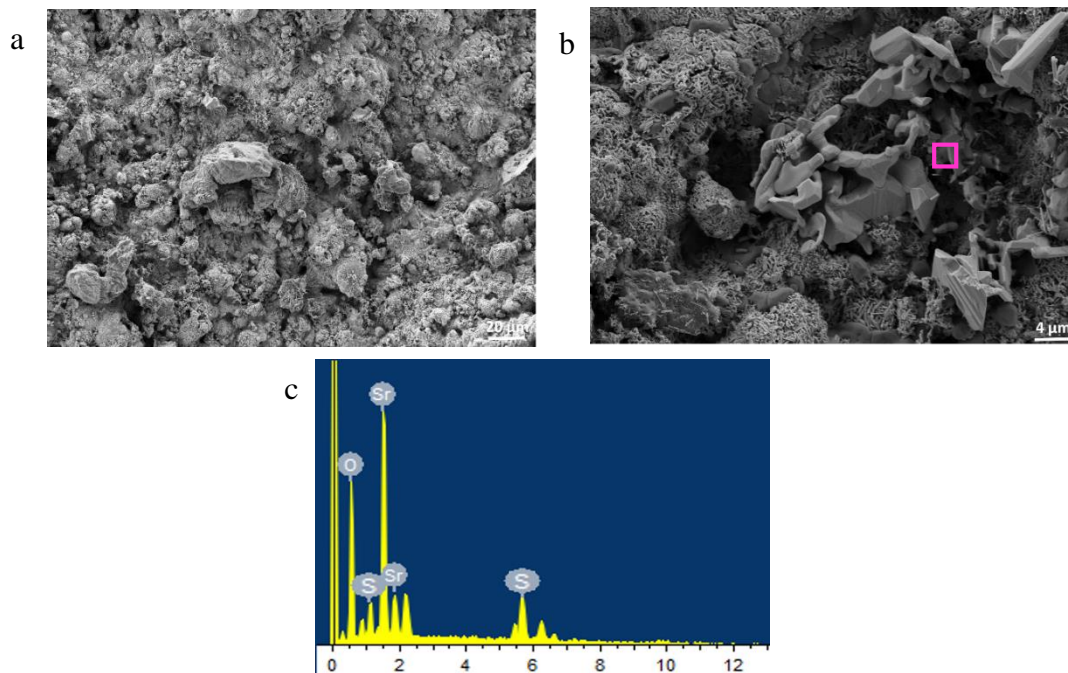


Figure 5.20 The SEM morphology of failed samples exposed to 90 % wt  $\text{Na}_2\text{SO}_4$  + 5 % wt  $\text{V}_2\text{O}_5$  + 5 % wt  $\text{NaCl}$  at 700 °C showing  
a) Low magnification image of corroded surface  
b) High magnification image of the hot corrosion products formed on surface  
c) EDS analysis of the corrosion products formed

Table 5.7 Composition of the products formed on samples exposed to marine conditions at 700 °C

Element	Sm	Sr	Al	O	Na	S	V	Cl
wt. %	0.00	47.15	0.00	35.62	0.00	17.2	0.00	0.00

### Samples at 900 °C

The XRD pattern of the failed samples in 90 % wt. Na<sub>2</sub>SO<sub>4</sub> + 5 % wt. V<sub>2</sub>O<sub>5</sub> + 5 % wt. NaCl at 900 °C is shown in Figure 5.21. Besides the top coat peaks Al<sub>2</sub>O<sub>3</sub> and SSA, corrosion-evolved SmAlO<sub>3</sub>, AlVO<sub>4</sub>, and SrSO<sub>4</sub> were detected. The high magnification SEM images, as in Figure 5.22 showed more regularly shaped SrSO<sub>4</sub> than irregularly shaped SrSO<sub>4</sub> observed in the same corrosion atmosphere at 700 °C. The measured composition of the corrosion products is given in Table 5.8. It can be noticed that under marine conditions, at both temperatures, SrSO<sub>4</sub> is formed due to the abundance of sulphate content.

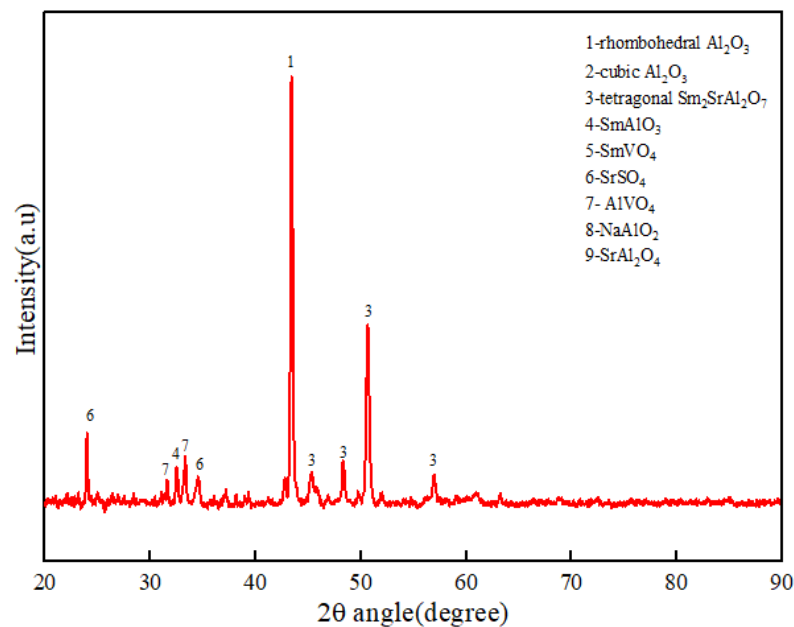


Figure 5.21 XRD pattern of sample exposed to 90 % wt Na<sub>2</sub>SO<sub>4</sub> + 5 % wt V<sub>2</sub>O<sub>5</sub> + 5 % wt NaCl at 900 °C

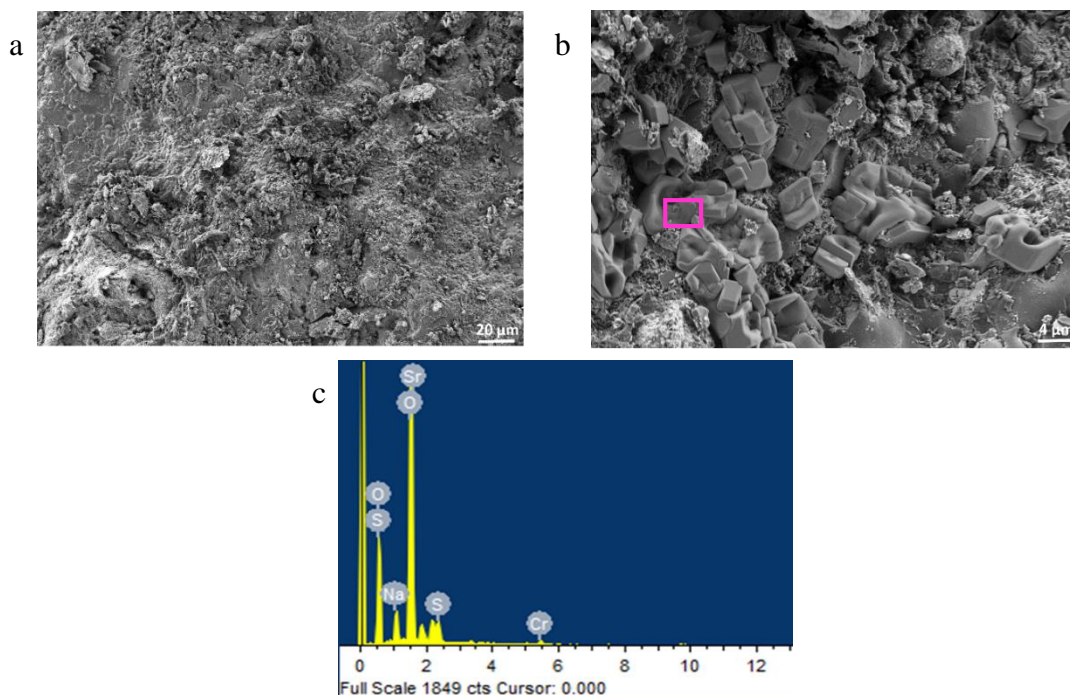


Figure 5.22 The SEM morphology of failed samples exposed to 90 % wt Na<sub>2</sub>SO<sub>4</sub> + 5 %wt V<sub>2</sub>O<sub>5</sub> + 5 %wt NaCl at 900 °C showing  
 a) Low magnification image of corroded surface  
 b) High magnification image of the hot corrosion products formed on surface  
 c) EDS analysis of the corrosion products formed

Table 5.8 Composition of the products formed on as-coated samples exposed to marine conditions at 900 °C

Element	Sm	Sr	Al	O	Na	S	V	Cl
wt. %	0.00	47.23	0.00	34.02	0.91	17.14	0.00	0.00

Comparing the corrosion products formed at different atmospheres, it can be noticed that SrSO<sub>4</sub> is formed only in marine conditions where sodium sulphate is abundant, and not in aviation atmospheres.

From the XRD patterns, it can be inferred that the SSA reacted more with the corrosive salts than the alumina matrix. The reactivity of the top coat elements depends on the ionic radius and basicity, which follows the order Sr<sup>2+</sup>>Sm<sup>3+</sup>>Al<sup>3+</sup>, which makes



SrO from decomposition more vulnerable to react with salts (Baskaran and Arya 2018). This is in agreement with the formation of SrSO<sub>4</sub> from the reaction of SrAl<sub>2</sub>O<sub>4</sub>.

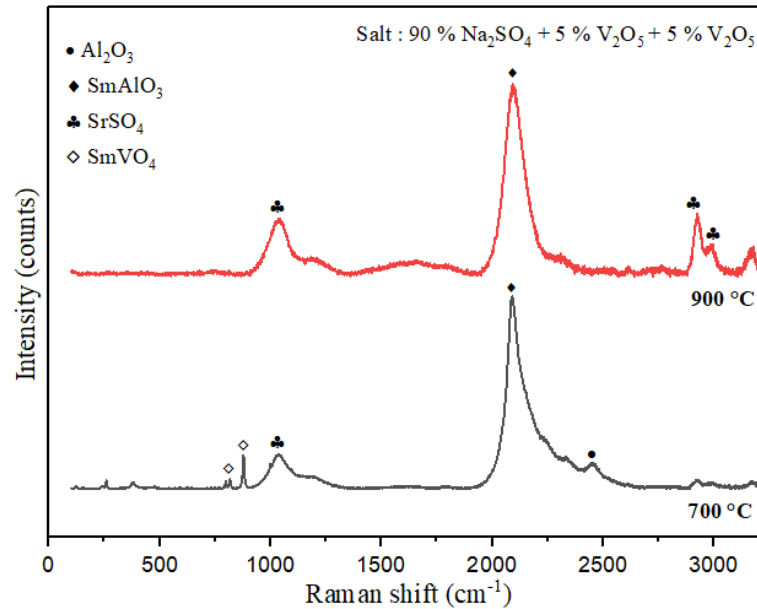


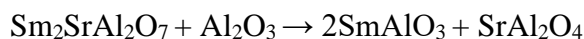
Figure 5.23 Raman spectrum of as-coated samples after hot corrosion tests at 90 wt Na<sub>2</sub>SO<sub>4</sub> + 5 wt V<sub>2</sub>O<sub>5</sub> + 5 wt NaCl at 700 °C and 900 °C

Figure 5.23 shows the Raman spectrum after hot corrosion tests, which is found to agree with the XRD patterns. Similarly, SrSO<sub>4</sub> peak at 1001cm<sup>-1</sup> was identified.

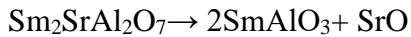
### 5.2.3 Overview of corrosion interactions

On investigating the as-coated composite thermal barrier coating samples exposed to hot corrosion conditions, it can be inferred that the composite becomes unstable in the presence of corrosive salts at higher temperatures. In the corrosive environment, Sm<sub>2</sub>SrAl<sub>2</sub>O<sub>7</sub> dissociates into less stable compounds which react further with the sulphates and vanadates. The dissociation product SmAlO<sub>3</sub> is found in every sample after hot corrosion, irrespective of the prevailing corrosion conditions.

From the XRD and EDS analysis, the composite dissociation is assumed to be according to Eq.(5.1).



SmAlO<sub>3</sub> can also form from the decomposition of Sm<sub>2</sub>SrAl<sub>2</sub>O<sub>7</sub> to SmAlO<sub>3</sub> and SrO as



Eq.(5.12)

Interestingly, the dominance of gamma alumina was not observed in any samples after hot corrosion. Alpha alumina is highly inert to chemical interactions than gamma alumina. The porous gamma alumina possesses a high surface area, which tends to increase the reactivity to corrosive salts. The reactivity of solid reactants increases with an increase in surface area. Besides, the alpha alumina bulk shows higher stability than the gamma alumina bulk (Andersson 2005; Busca 2014). The gamma alumina reacted with the corrosives, while the alpha alumina offered more resistance. The XRD patterns of the corroded surfaces did not show a major presence of gamma alumina. This sheds light on the fact that retention of the alpha phase upon thermal spraying can aid better corrosion resistance.

It was noted that  $\text{SrSO}_4$  is formed only when sulphates are abundant and not formed in aviation conditions at 700 °C and 900 °C. In the case of aviation conditions, at both temperatures, the formation of  $\text{SmVO}_4$  is predominant. This can be explained by the fact that  $\text{NaVO}_3$  formation is preferred at 30-50%  $\text{V}_2\text{O}_5$  in the  $\text{Na}_2\text{SO}_4$ - $\text{V}_2\text{O}_5$  system.  $\text{NaVO}_3$  also forms from the direct reaction of  $\text{Na}_2\text{O}$  and  $\text{V}_2\text{O}_5$ . The  $\text{NaVO}_3$  reacts with  $\text{Sm}_2\text{O}_3$  to form  $\text{SmVO}_4$ . It can be inferred that the introduction of  $\text{V}_2\text{O}_5$  into  $\text{Na}_2\text{SO}_4$  changes the overall reaction mechanism and forms corrosive products at temperatures lower than the melting point of  $\text{Na}_2\text{SO}_4$  (Yugeswaran et al. 2012).

In all the samples, no substrate or bond coat diffusion was observed, as  $\text{Al}_2\text{O}_3$  coatings are well known for mitigating migration than conventional YSZ coatings (Ramaswamy et al. 1997). Generally, the alumina layer is capable of suppressing harmful melt infiltration toward the substrate. Likewise, aluminium interacts with CMAS melt, forming Al-rich glass compositions with a very high melting point, preventing further infiltrations. Although the developed coating was dense, it is to be assumed that the microcracks at the splat boundaries and micro porosities have assisted in the penetration of corrosive salts. atmospheres failed early at 700 °C and 900 °C. This can be explained by the fact that the addition of  $\text{NaCl}$  to  $\text{Na}_2\text{SO}_4$  results in changing the environment from acidic to b

It is interesting to note that samples exposed to chloride asic, accelerating the corrosive attack due to the breakdown of the protective oxide scales (Gurrappa 1999). So, the presence of chloride ions in salt makes alumina more susceptible to cracking and spallation. Additionally, NaCl tends to form a low melting eutectic with Na<sub>2</sub>SO<sub>4</sub>. In addition, NaCl can react with SO<sub>2</sub> in the flue gas, forming Na<sub>2</sub>SO<sub>4</sub>, making the chloride atmosphere more detrimental. In the presence of vanadate melts, the oxides form an acidic solute, making the attack more rapid than in a pure sulphate melt. The early failure in chloride salts may be due to the fact that NaCl tends to form a low melting eutectic with Na<sub>2</sub>SO<sub>4</sub> (about 620 °C). Additionally, NaCl can react with SO<sub>2</sub> in the flue gas, forming Na<sub>2</sub>SO<sub>4</sub>, adding to the corrosive salts, making the chloride atmosphere more detrimental (Eliaz et al. 2002). Overall, Cl<sup>-</sup> ions has a significant effect on the corrosion behavior. Cl<sup>-</sup> induced active corrosion and breakaway of dense protective films are reported to be major failure mechanisms in high-temperature components (Sadeghi et al. 2019). Also, the higher sulphate content in marine conditions tends to induce a de-adhesion and subsequent spallation, if it infiltrates through pores into the coating(Jarvis and Carter 2002).

It is worth noting that no major cracks were noticed on the corroded surface. This does not completely eradicate the cracking possibility, as the cracks may be covered up with the corrosion products formed. In addition, no evidence of the applied corrosive salts in their original form was found in the XRD pattern and morphology observation. It can be assumed that the salts applied are completely consumed by the interactions. The study indicates that the SSA dispersion in the alumina coatings is unstable as compared to pure alumina. For enhanced life of the composite coatings, microstructural modifications are to be considered, reducing the porosity and preventing salt infiltration.

Although the developed coating was dense, it is to be assumed that the microcracks at the splat boundaries and micro porosities have assisted in the penetration of corrosives. The splats parallel to the surface hinder the easy penetration of corrosion salts into the coating. Besides, the cubic gamma-alumina formed is more porous than the rhombohedral alumina, which may have aided in the corrosion failure of the composite coatings (Chatha et al. 2012; Fiedler 1984). On the whole, it is interesting

that the  $\text{Al}_2\text{O}_3$  -  $\text{Sm}_2\text{SrAl}_2\text{O}_7$  composite rendered higher resistance than the single-layer  $\text{Sm}_2\text{SrAl}_2\text{O}_7$  TBC under similar conditions (Baskaran and Arya 2018). The dense alumina capable of suppressing harmful melt infiltration and better stability of SSA have aided the enhanced life of the system. The hot corrosion performance of the composite coating can be improved by surface modifications, which can reduce the porosity and increase the density of the coating. This can prevent melt infiltration and enhance the life of the component.

### **5.3 Solid particle erosion behavior of as-coated samples**

In gas turbine components, the impact of solid particles from the inlet stream causes progressive removal of material from components, which leads to localized damages reducing the component life (Ramachandran et al. 2013). Solid particle erosion causes thinning of components, changes in blade geometry, and overheating of components in gas turbines (Cernuschi et al. 2016). The erosion resistance of the ceramic thermal barrier coatings is generally lower than their bulk sintered ceramic form. In general, the erosion response of a TBC system depends on the impingement variables, erodent variables, and material variables. The main impingement variables include the erodent flux, velocity, and impact angle, while the erodent variables refer to the shape, size, and hardness of the erodents being impacted. The material variables include mechanical characteristics such as hardness and strength, and microstructural features such as porosities and defects (Krishnamurthy et al. 2012). The effect of factors such as impingement angle and temperature on erosion behavior of the coatings are discussed in this chapter.

#### **5.3.1 Macroscopic observation of eroded samples**

The air jet erosion test on plasma sprayed 70 wt.%  $\text{Al}_2\text{O}_3$  - 30 wt.%  $\text{Sm}_2\text{SrAl}_2\text{O}_7$  composite TBCs was performed at temperatures of 200 °C and 800 °C, at impact angles 30° and 90°. The average erosion wear increases with an increase in erodent size. Westergard reports an increase in erosion loss by a factor of 20, on increasing the erodent size from 75  $\mu\text{m}$  to 100  $\mu\text{m}$  (Westergård et al. 1998). In the present work, the impingement variables are held constant. A standard alumina erodent of 50  $\mu\text{m}$  size was used for all the tests, to analyze the effect of impact angle, temperature, and surface microstructure of the system on erosion behavior. The tests were performed at an optimum feed rate of 3 g/min, which is comparable with other researchers (Baskaran 2018). An increased erodent flux causes the spreading of the air jet, and the centreline velocity reduces rapidly deteriorating the impact (Ramachandran et al. 2013). The photographic images of the composite-coated samples after the erosion test are shown in Figure 5.24.

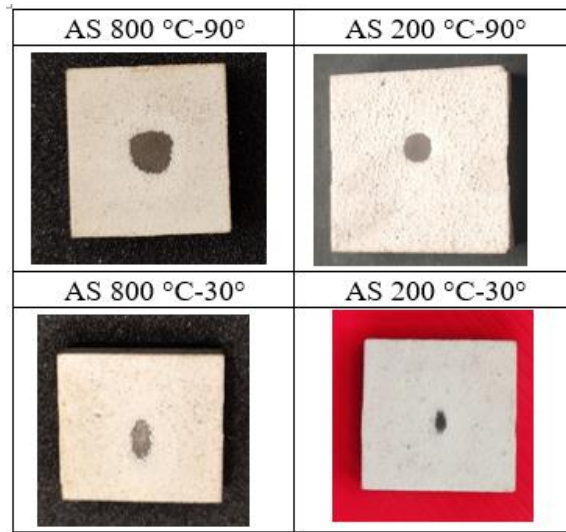


Figure 5.24 Photographic images of as-coated samples exposed to erosion under various conditions

Table 5.9 Scar dimensions of samples exposed to various conditions measured in surface profilometer

		AS-800 °C	AS-200 °C
<b>Elliptical Scar</b> (30°)	Major		
	Diameter (mm)	5.20	2.83
	Minor		
	Diameter (mm)	2.20	1.55
<b>Circular Scar</b> (90°)		AS-800 °C	AS-200 °C
	Scar Diameter (mm)	4.94	2.82

After 25 minutes of erosion at 200 °C and 800 °C, it was found that a major part of the composite top coat has been chipped off. The samples undergo a localized coating removal during the test, which appear as erosion scars. At 90°, the scars presented a nearly circular area while at 30°, a nearly elliptical area was observed. The dimensions of the scars measured using a Nanovea ST-400 surface profilometer are reported in Table 5.9. An increase in the dimension of scars is noticed on increasing the exposure

temperature at each impact angle. Considering all samples exposed at a 30° impact angle, the length of the major axis varied from 2.83 cm to 5.20 cm. In the case of a 90° impact angle, the scar diameter varied from 2.82 cm to 4.94 cm. The variations can be correlated to the exposed erosion conditions and the surface characteristics of the coatings, which are discussed in upcoming sections.

### **5.3.2 Cumulative erosion mass loss**

The repeated impact of erodents onto the target surface causes the continuous removal of material from the system. Figure 5.25 shows the cumulative mass loss of coatings against the total mass of erodent impacted at 200 °C and 800 °C. The plots reflect an overall trend of increasing weight loss on increasing erodent mass impacted. The highest mass loss in as-coated samples was observed at 800 °C at a 90° impact angle. From the graph, a general trend with a nearly linear region after an initial non-linear transient region can be noticed; a higher erosion rate followed by a steady state erosion. The initial mass loss may be due to the faster removal of surface roughness, such as protrusions on the surface, which easily get fractured and removed upon initial particle impact events. A similar trend with variation in mass loss is reported by M Presby (Presby and Harder 2021). Irrespective of the prevailing erosion conditions, an increase in mass loss after 20 min of erosion (60 g of erodent impact) was seen in a few samples, which is attributed to the flaking of particles upon crack propagation along splat interfaces leading to material removal as larger particles. A similar observation was reported by Li et al. where a sharp rise in the material loss was noted over 40 g of erodent (Fredy et al. 2022; Li et al. 2006). In general, the volume of eroded material is proportional to the cumulative mass of erodents impacted on the coating surface.

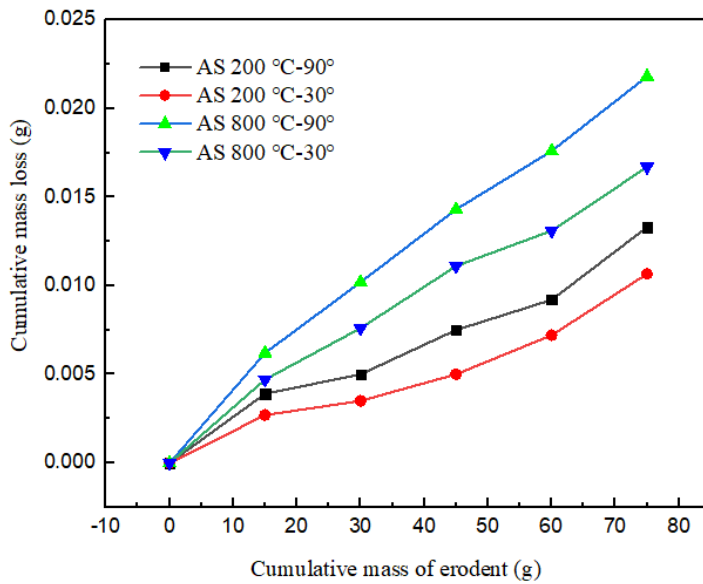


Figure 5.25 Graph showing cumulative mass loss of coating vs cumulative mass of erodents for as-coated samples subjected to various erosion conditions

### 5.3.3 Average erosion values

The average erosion values under various erosive conditions are calculated according to the ASTM G76-13 standard. The average erosion value is determined by dividing the erosion rate by the erodent feed rate and then dividing it by the coating density. The mean values of the erosion rate of different samples are used for the calculation. From Figure 5.26-b, it can be noticed that the average erosion value for as-coated samples was the highest at 800 °C at a 90° impact angle. The steady-state erosion rate (calculated from the slope of mass loss vs time plot) follows a similar pattern to average erosion (Figure 5.26-a), with the highest at 800 °C at a 90° impact angle. The

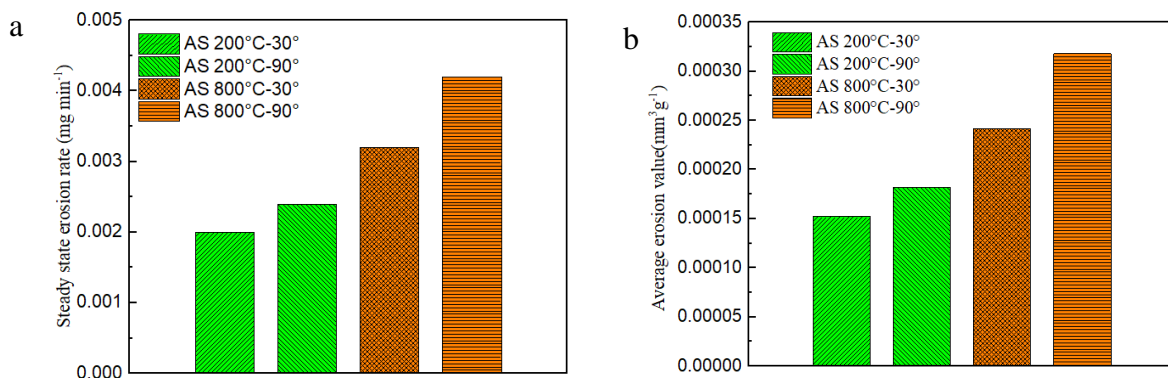


Figure 5.26 Plots showing a) steady state erosion rate and b) average erosion values of as-coated samples at different conditions



average erosion values at 200 °C and 800 °C showed a noticeable difference at the tested impact angles, proving a comparatively lower erosion resistance at higher temperatures.

From the results, the average erosion value and steady-state erosion rate calculated at each temperature are higher at 90° than at a 30° angle. Generally, the transference of kinetic energy to the target surface is maximum in a normal impact. The single-layer SSA coatings have shown a larger erosion at 30° than at 90° (Baskaran 2018). Ramm et al. report that single-layered alumina coatings have higher erosion at 90° than at smaller angles. Even though the APS ceramic coatings are anisotropic, the impact angle dependence on erosion rate is reported to be uniform throughout the surface. Moreover, the erosion mechanisms of APS sprayed coatings will vary from the same material in the bulk sintered form (Ramm et al. 1993).

### ***Effect of erodent***

As erosion damage is a collective function of individual particle impacts, the geometry of the particles is highly significant. The erodent impact creates a succession of events with crack initiation, crack propagation, and subsequent material removal. The SEM image of the erodents used is shown in Figure 5.27. It is found that the particles exhibited different shapes like nearly spherical, ellipsoidal, and angular which effectively simulate the real-time erosion environment. The ellipsoidal particles impacting on long-axis contact create higher stress and larger erosion depth than spherical particles. The ellipsoidal particles impacting the short axis create lower stress due to the larger area of contact over the target coating surface. Generally, sharp erodents tend to increase microcutting, while nearby round erodents tend to increase ploughing. As the impact orientations are purely random, the angular particles present tend to induce both the mechanisms of ploughing and microcutting. The erodents, on impact create different vertical component velocities and different contact areas in vertical directions and give rise to different magnitudes of stress (Bahadur and Badruddin 1990; Ning et al. 2022). These varying conditions imposed, create different morphological features to the erosion scars. Certain erodents, such as silica, show a pseudo-ductile behavior at higher temperatures due to softening, which is not the case

with alumina, making alumina the best candidate for erosion tests (Wellman and Nicholls 2008).

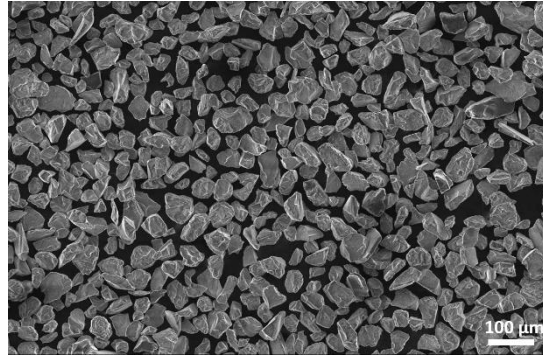


Figure 5.27 SEM image of the erodents used

#### 5.3.4 Influence of microstructural and mechanical features on erosion behavior

The tribological behavior of the coatings is highly dependent on the microstructural and mechanical properties of the system. The erosion resistance declines with an increasing porosity level. As mentioned in section 4.2, the as-coated samples showed a porosity of 10 %. The porosities in the microstructure generally aid in reducing the thermal conductivity, while it trades off the erosion performance. The porosity could bring down the effective load-bearing area upon erodent impact. In addition to being multi-axial stress concentrator sites, pores have another significant role in linking up the splat boundaries and microcracks during successive impacts and removing material as large flakes (Krishnamurthy et al. 2012).

The microstructure of the coating system must contain the least cracks and delaminations, which may otherwise initiate major cracks upon impact. Also, the partially melted particles within the coating may ease the crack propagation upon erodent impact. The more completely molten particles increase the amount of bonding between the splats and reduce the porosity of coatings, and this reflects as a higher resistance to erosion (Mahade et al. 2021; Westergård et al. 1998).

The measured hardness of the as-coated samples was 11.5 GPa which is comparable with as-coated single-layer SSA coating. The mechanical properties of as-coated samples and similar systems are compiled in Table 5.10. The measured hardness value of the composite coating was less than that of bulk alumina. The reduction may

be due to porosities in the coating and a comparatively lower hardness of  $\gamma$ - $\text{Al}_2\text{O}_3$  than  $\alpha$ - $\text{Al}_2\text{O}_3$  (Krishnamurthy et al. 2012). It is a fact that, due to the non-uniform distribution of surface asperities, there exists a factor of uncertainty in the hardness measurement of thermal spray coatings. The microhardness methods provide a localized value rather than an all-inclusive value. Generally, a practical coating will have a non-uniform distribution of porosities, voids, and cracks (Caroline 2021). The hardness and toughness will endure erosion damage even though the mechanism may be dominated by the interactions at low fracture toughness areas, cracks, and delaminations. Matikainen et al. suggest that even though there are different parameters involved, the overall hardness and strength of the coating is the determining factor for erosion resistance (Matikainen et al. 2014). In general, researchers report that TBCs with low hardness and high porosity had a lower erosion resistance (Caroline 2021; Mahade et al. 2021). Therefore, increased surface hardness can enhance erosion resistance to a certain extent irrespective of other microstructural features.

Table 5.10 Mechanical properties of the as-coated samples and similar systems

	Hardness	Young's Modulus	Reference
$\text{Al}_2\text{O}_3$ - $\text{Sm}_2\text{SrAl}_2\text{O}_7$	11.5 GPa	152 GPa	Experimental
$\text{Sm}_2\text{SrAl}_2\text{O}_7$	5 GPa	73 GPa	(Baskaran 2018)
YSZ	12.26 GPa	-	(Ramesh and Marimuthu 2020)
50% $\text{Al}_2\text{O}_3$ - 50% YSZ	12.7 GPa	-	(Saral and Toplan 2009)
$\text{Al}_2\text{O}_3$	16 GPa	-	(Lampke et al. 2011)

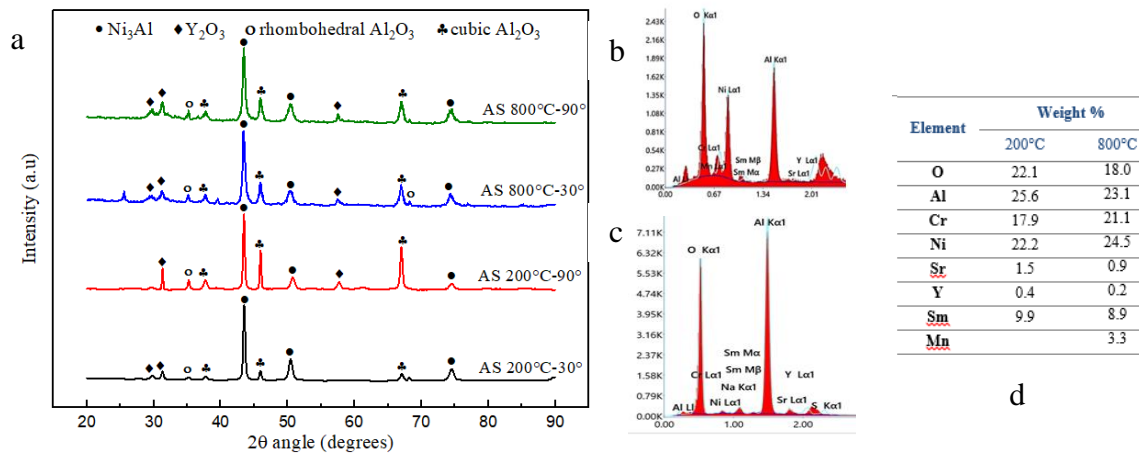


Figure 5.28 a) XRD patterns of scars of samples eroded at various conditions b) EDS composition of scar of samples exposed at 800 °C and c) 200 °C at 90° angle d) Nominal weight percentages observed in scars

### 5.3.5 Erosion mechanism

The scars on the eroded surfaces, as shown in Figure 5.24, are examined in detail to study the erosion and material removal mechanisms involved. The XRD patterns of the scar consisted peaks of both the top coat and bond coat elements, proving that a significant fraction of the top coat is removed, exposing areas of the bond coat. As shown in Figure 5.28, the XRD of eroded areas under different conditions did not show a major difference, other than the intensity variations which is due to the microstructural non-uniformity of the eroded areas. It is observed that the peak at 43.4° showed a higher FWHM (0.307) for samples at 800 °C (AS 800 °C -30°, AS 800 °C-90°) than the samples at 200 °C (AS 200 °C-90°, AS 200 °C-30°). A higher FWHM at 800 °C than 200 °C shows a higher stress at 800 °C. Intensity variations in the cubic Al<sub>2</sub>O<sub>3</sub> peaks at 45.8° can be seen, which is due to microstructural variations on the surface (Ghasemi et al. 2014).

Generally, erosion in TBCs has been attributed to individual splat debonding through lateral cracking. During coating, the partial solidification of feed particles before impact results in debonding issues. For a very high inter-splat bonding, the erosion removal mechanism may stay closer to bulk materials (Ramm et al. 1993). Ramachandran et al. report that, the erosion of APS-coated TBCs involves plastic deformation and brittle cracking in parallel (Ramachandran et al. 2013).

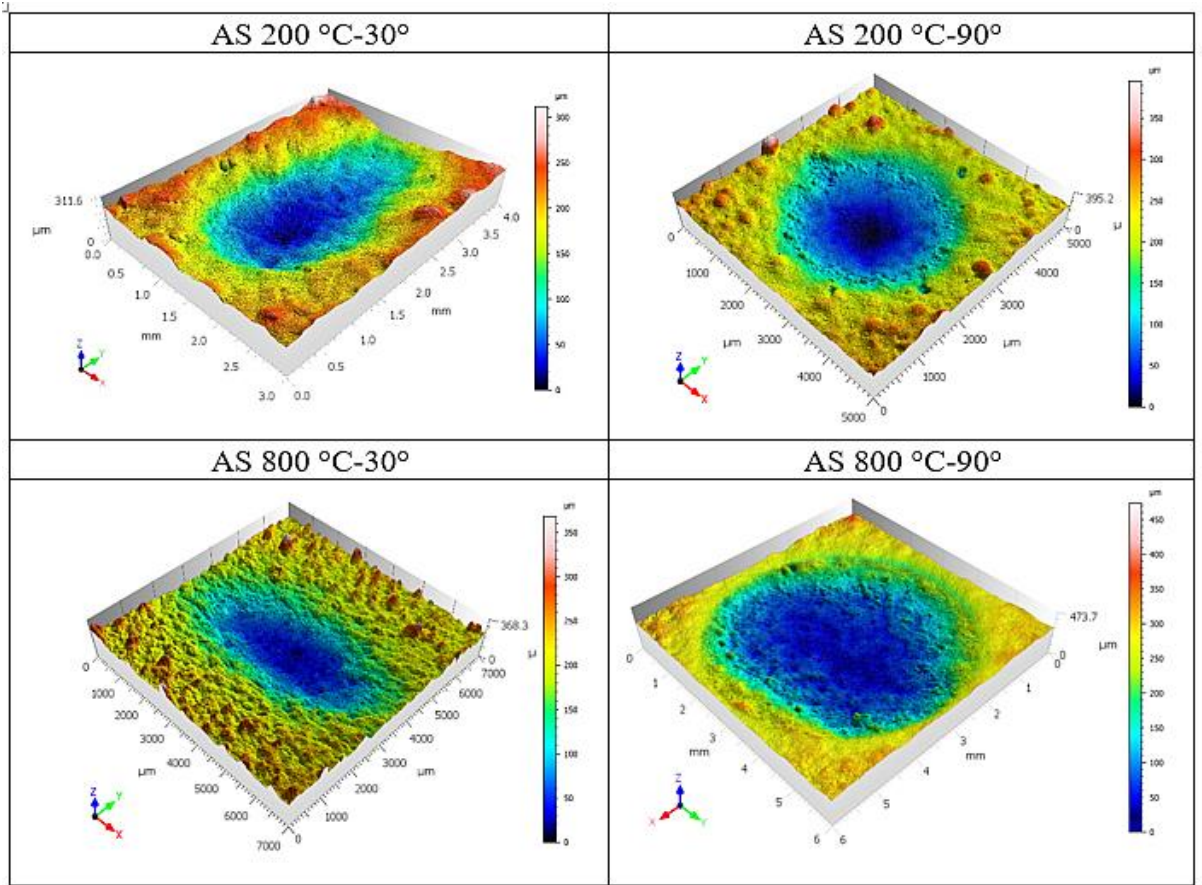


Figure 5.29 Profilometric images of erosion scars in as-coated samples subjected to erosion at different conditions

The profilometric views of the erosion scars in the as-coated samples subjected to erosion at various conditions are shown in Figure 5.29. Appreciable variations in the scar profile can be noticed in the profilometric view. The as-coated samples exposed at 800 °C and 90° showed a bigger scar, in agreement with the highest average erosion value calculated, while the smallest scar was noticed for samples at 200 °C at a 30° impact angle. Kaplan et al. 2018 have reported a similar higher amplitude of peaks and valleys after erosion at a 90° impact angle in ambient temperature conditions.

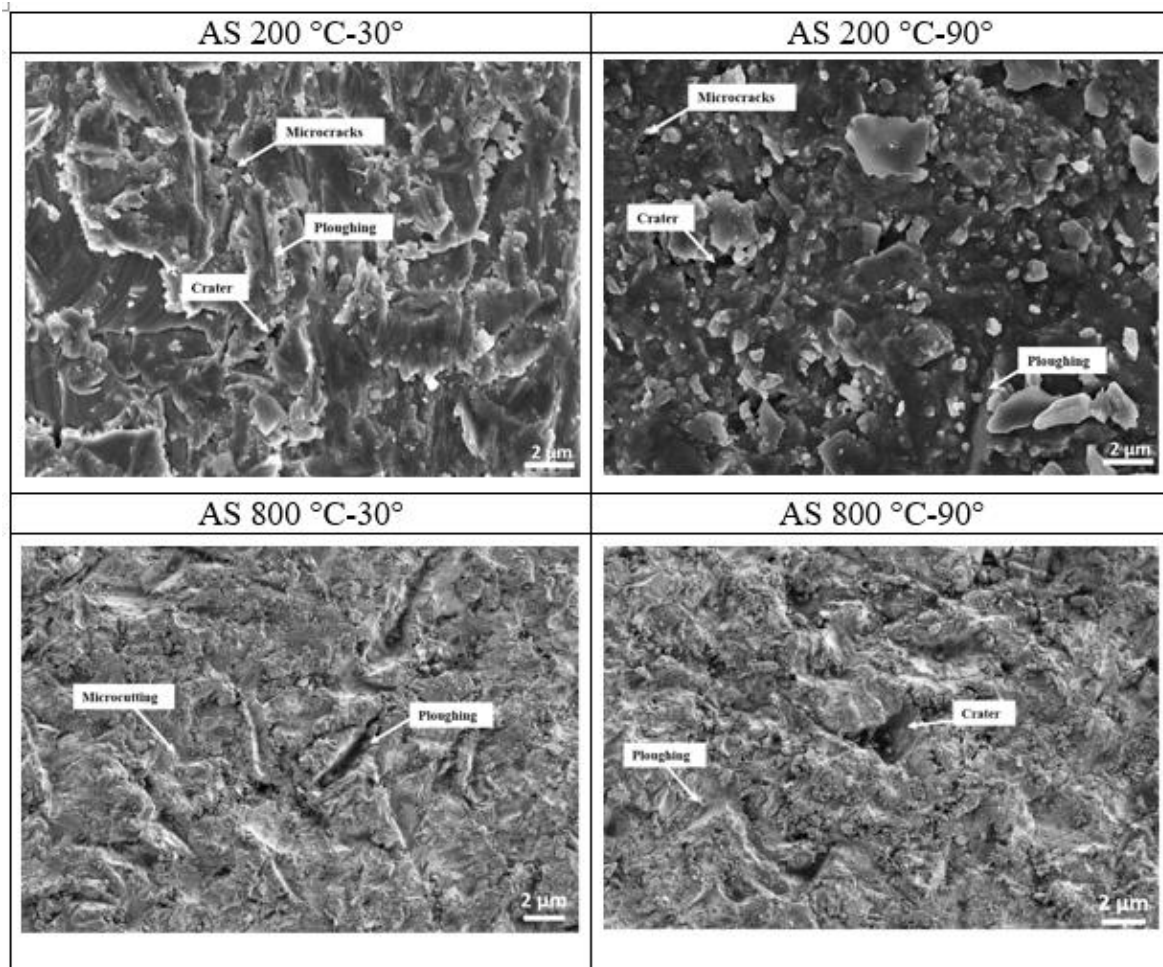


Figure 5.30 High magnification SEM images of as-coated samples exposed to various erosion conditions

As shown in Figure 5.30, in the developed composite system, the mechanism of material removal did not show remarkable variations under different conditions. At 800 °C, the samples showed deeper and longer ploughing marks, revealing a ductile mechanism involved. From the worn surfaces, it can be assumed that more material is removed by ploughing at 800 °C. Microcutting, microcracks, and grooves are also observed in the scar, pointing to the brittle mechanisms. The microcutting generally occurs as ridges, when the erodents impact at the edges of grooves. At 800 °C, deeper craters are seen at 90° than 30° impact angles. Craters are often distinguished by a central depression and peripheral lips arising from material displacement. The lips are often removed by progressive erosion. The larger craters may be due to the higher kinetic energy imparted into the heated-up coating, which allows a deeper penetration and more material removal in a bulk form (Caroline 2021; Kaplan et al. 2018).

At 200 °C, the erosion mechanisms were similar to that at 800 °C, with a lower magnitude. The degree of ploughing and material removal is lesser at 200 °C with shallow ploughing channels as compared to 800 °C. Microcracks and smaller craters are visible in the eroded area in samples exposed at 200 °C. Generally, upon erodent impact, the lamella microcracks will get connected with existing cracks, removing material as bulk. Further, in APS coatings, the lamellas are in weak contact with the underlying lamellas, which may lead to a more bulky removal (Matikainen et al. 2014). From the difference in the size of the craters at 200 °C and 800 °C, it can be inferred that at a higher temperature, the material allows a deeper penetration, which shows a sign of a higher ductility at 800 °C. Also, the longer and deeper ploughing channels contribute to the fact of higher ductility at 800 °C. In the as-coated samples, though there are mechanisms suggesting ductility, the mass monitoring did not show up any negative erosion and subsequent mass gain, eradicating the possibility of any clinging mechanisms involved in general. In the clinging mechanism, the harder erodents get adhered to the ductile target surface on high-velocity impact, reflecting as a mass gain in the system. Researchers have reported clinging mechanisms with the presence of hard alumina erodent particles adhered to the coating surface along with a shear phenomenon. The clinging mechanism is more predominant in the case of highly ductile materials (Duraipandi et al. 2021). The absence of any clinging mechanisms eradicates the possibility of higher ductile behavior of the developed system under the tested conditions. All the mechanisms of material removal identified in the as-coated samples under various erosive conditions are illustrated in Figure 5.31.

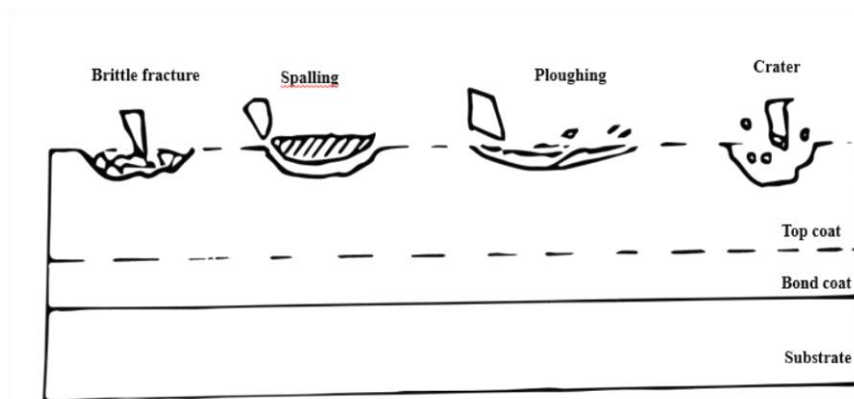


Figure 5.31 Schematic diagram of erosion mechanisms observed in the developed coating

A higher erosion at a 30° impact angle than 90° is generally a behavior of ductile materials, while brittle coatings erode more at 90°. The single-layer  $\text{Sm}_2\text{SrAl}_2\text{O}_7$  ceramic TBC reports a ductile behavior with maximum erosion at 30° than at a 90° impact angle. On the other hand, single-layer alumina coatings exhibit a brittle behavior with higher erosion damage at 90°. It is stated that introducing a ductile phase could relax the stresses by yielding and delaying cracking failure (Ramm et al. 1993; Ramesh et al. 2010). It can be assumed that the introduction of ductile  $\text{Sm}_2\text{SrAl}_2\text{O}_7$  phase to the brittle alumina altered the overall failure mechanism to a mixed mode of material removal.

The impact of hard erodents on plasma spray coatings typically involves a plastic flow of material along with brittle fracture. The erosion of alumina-titania coatings has shown that the alumina matrix in the coating tend to remove material through brittle mechanisms. The APS-sprayed  $\text{Al}_2\text{O}_3$ -  $\text{TiO}_2$  coatings offered better resistance than conventional coatings (Duraipandi et al. 2021). It is worth mentioning that the angular dependence of erosion depends not only on the material but also on the erosion conditions prevailing. So, the ductile and brittle mechanisms in the developed samples under the tested conditions may not pursue at all the possible erosive conditions. At a constant set of erosion parameters, the erosion resistance of coatings depends on the morphology, microstructural integrity, and mechanical properties of the system. Surface modifications aiming at minimum defects can provide a superior erosion resistance to the developed 70 wt.%  $\text{Al}_2\text{O}_3$  - 30 wt.%  $\text{Sm}_2\text{SrAl}_2\text{O}_7$  composite TBCs.



## 5.4 Summary of test results of as-coated sample

### Isothermal oxidation test

- The 70 wt.% alumina - 30 wt.% samarium strontium aluminate composite coatings showed a parabolic weight gain during the oxidation test at 1100 °C.
- A uniform thermally grown oxide layer of  $\text{Al}_2\text{O}_3$  was observed at the bond coat top coat interface after oxidation.
- Destabilization of top coat composite materials was detected through XRD analysis of the oxidized surface.

### Hot corrosion test

- The TBC specimens showed  $\text{SmVO}_4$ ,  $\text{SrSO}_4$ ,  $\text{SrV}_2\text{O}_6$ , and  $\text{NaAlO}_2$  as major corrosion products in the tested conditions.
- At 700 °C and 900 °C, the samples exposed to marine conditions exhibited 14.5 % and 11.6 % lower resistance than samples exposed to aviation conditions.
- It can be concluded that SSA dispersion in the composite is comparatively less resistant against molten salts, particularly chlorides.

### Solid particle erosion test

- In the developed 70 wt.% alumina - 30 wt.% samarium strontium aluminate composite coatings, a mixed mode of erosion with brittle and ductile mechanisms is ascertained under the tested conditions.
- The introduction of rare earth ceramic  $\text{Sm}_2\text{SrAl}_2\text{O}_7$  into the brittle alumina matrix reduced the brittle fracture mechanisms.
- At 200 °C and 800 °C, maximum erosion was observed at a 90° impact angle, which states that the brittle behavior dominates in the erosion failure.
- The erosion resistance of the developed coatings decreases with a rise in temperature.



## 6 Characterization of laser-treated samples

The as-coated 70 wt.%  $\text{Al}_2\text{O}_3$  - 30 wt.%  $\text{Sm}_2\text{SrAl}_2\text{O}_7$  composite top coat surfaces were treated using Nd: YAG laser, as described in section 3.2, to provide a better functional surface for the components. The laser absorption of materials is a complex phenomenon depending on both material properties and surface conditions. A laser power of 110 W at 0.6 m/min produced localized burning and evaporation on the surface of the samples. Reduced power levels were tested on samples and the surface response was noted, as shown in Figure 6.1. Visual inspection showed that power levels below 60 W do not cause any burning on the sample surface. Yet, the SEM observation of samples treated with 60 W displayed slight burning in a few areas, as shown in Figure 6.2. The high magnification view showed burnt marks with a number of pores. The microstructure observation revealed that a 40 W power at 0.5 m/min scan speed yields a better surface with minimum roughness with no burnt marks. A detailed analysis of microstructure is included in upcoming sections.

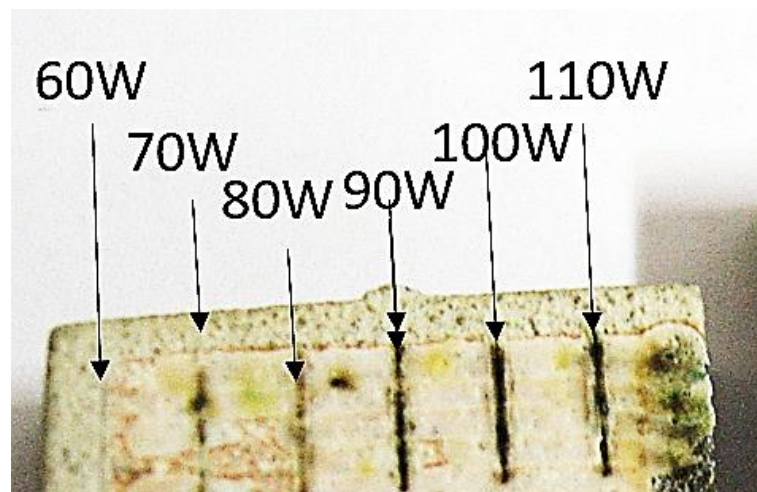


Figure 6.1 Image showing the burning marks on coating surface on exposure to laser beam with various power levels

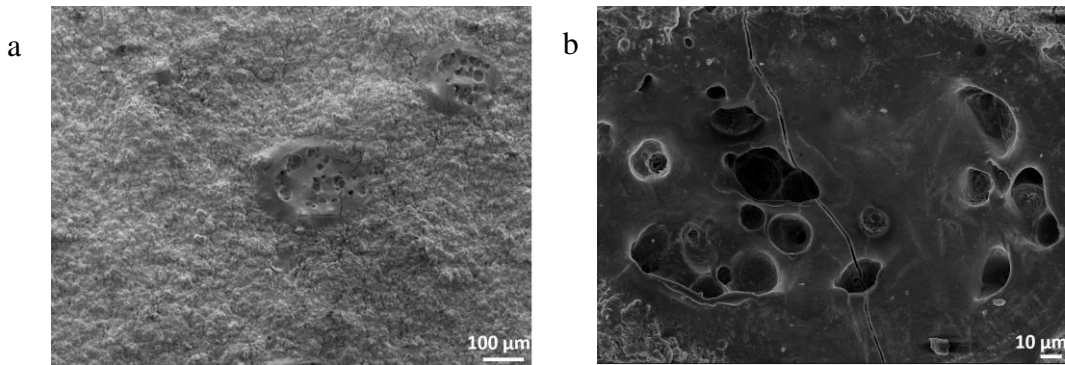


Figure 6.2 a) SEM image showing localized burning marks on samples treated with 60 W laser power, b) The high magnification view of the burned regions

The laser-treated samples showed a slightly faded appearance than the as-coated samples, as shown in Figure 6.3. The laser-treated samples are characterized in detail using XRD, SEM, and surface profilometer to investigate the changes that occurred.

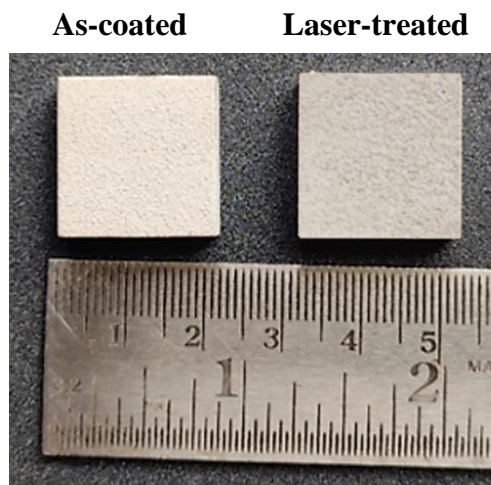


Figure 6.3 Photograph of the as-coated and laser modified samples

The surface of the laser-treated samples viewed in SEM is shown in Figure 6.4. The morphology showed a remelted surface with lower protrusions and asperities on the surface. Disc-like splats and unmolten particles were visible in the as-coated morphology. A major portion of the surface protrusions and unmolten particles have been remelted forming a smooth surface. A similar laser-modified surface with minimal defects and improved hardness was reported in other researches (Wang et al. 2014). Localized melting of surface asperities and solidified melt pools are visible on the laser-

treated surface. Very fine microcracks have been induced in the laser-treated surface, while the majority of the open porosities are sealed off. A notably higher number of open porosities was present on the as-coated surface. The laser glazing of LZ/YSZ has developed holes on glazed surfaces upon solidification, where gases in the melt pool had not enough time to escape resulting in bubble formation (Arshad et al. 2021).

The EDS analysis was carried out on the treated surface to monitor any changes in composition that occurred during the laser exposure. No noticeable difference in composition was detected after laser treatment. The measured composition is shown in Table 6.1. The distribution of the elements examined through elemental mapping (Figure 6.5) was found to be uniform declining any chances of selective segregation of elements during laser treatment.

Table 6.1 EDS composition of laser-treated surface

Elements	Sm	Sr	Al	O
Laser-treated surface (wt. %)	17.2	4.4	39.5	38.9

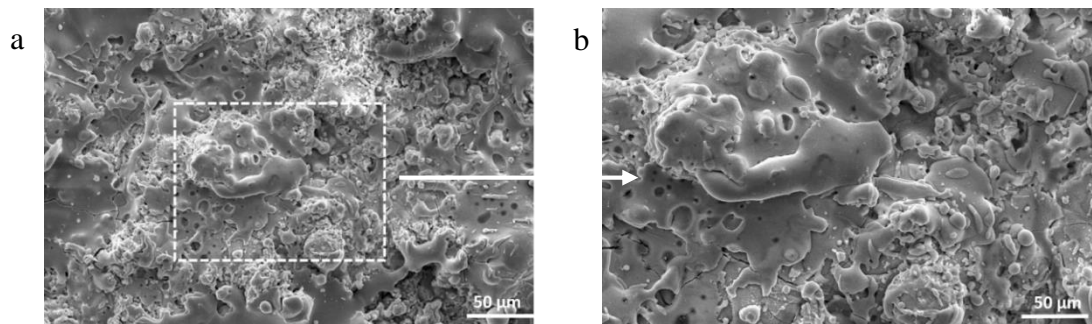


Figure 6.4 The surface of laser-treated specimen observed in SEM at different magnifications a) 500 X b) 1000 X

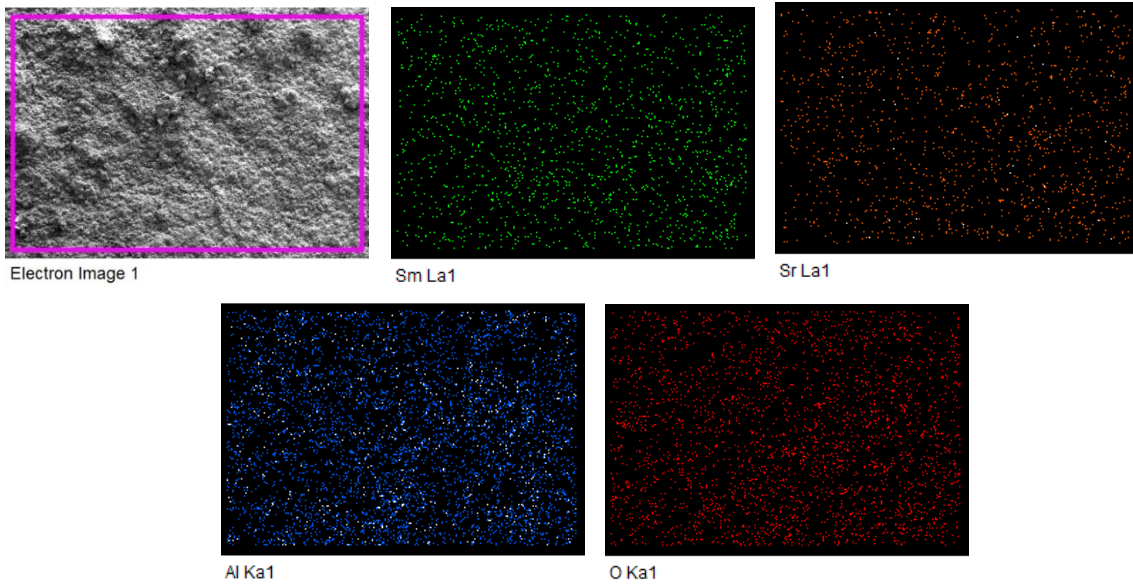


Figure 6.5 Elemental mapping of laser coated sample surface

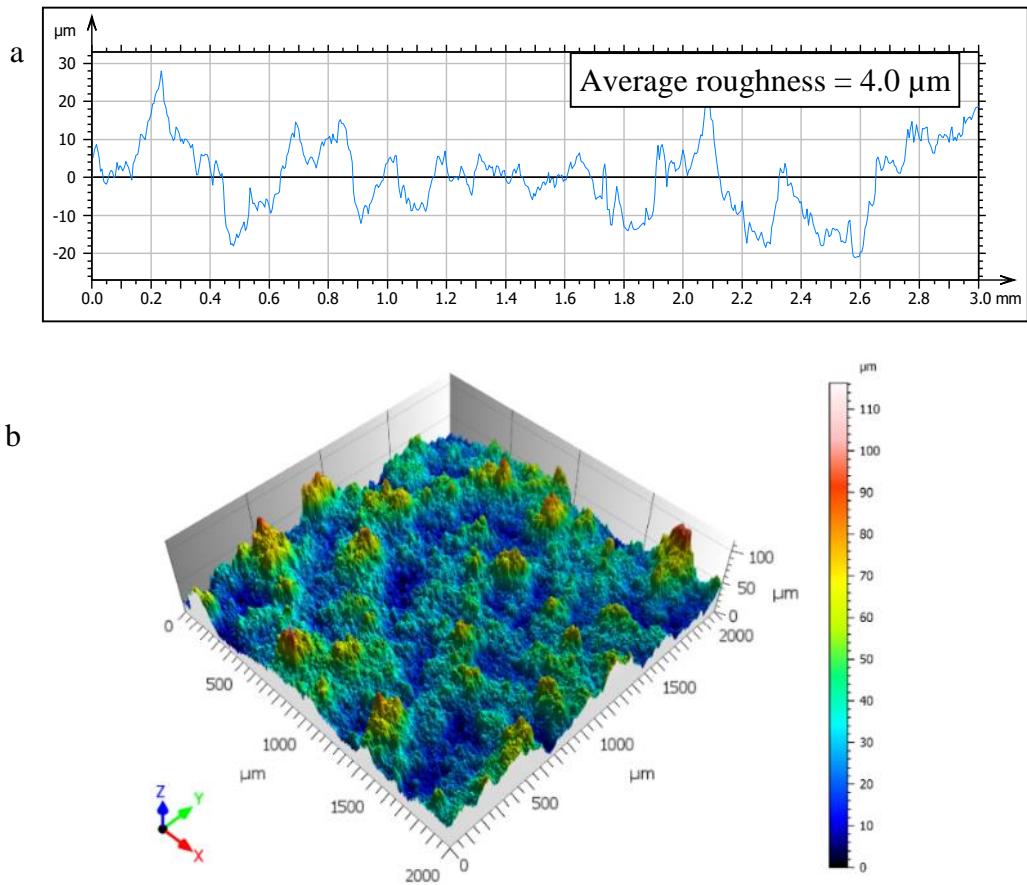


Figure 6.6 a) Surface roughness profile and b) profilometric image of laser-treated sample surface

The profilometric analysis of the laser-treated sample surface is shown in Figure 6.6. It is observed that a 33 % reduced roughness is achieved through laser treatment. The profilometric view shows peaks and valleys of lower magnitude as compared to the as-coated systems as a result of the melting of protrusions on the surface. The line scan measured a lower amplitude of roughness peaks. Similar instances of reduced roughness achieved in plasma-sprayed YSZ coatings through laser treatment have been reported (Múnez et al. 2011).

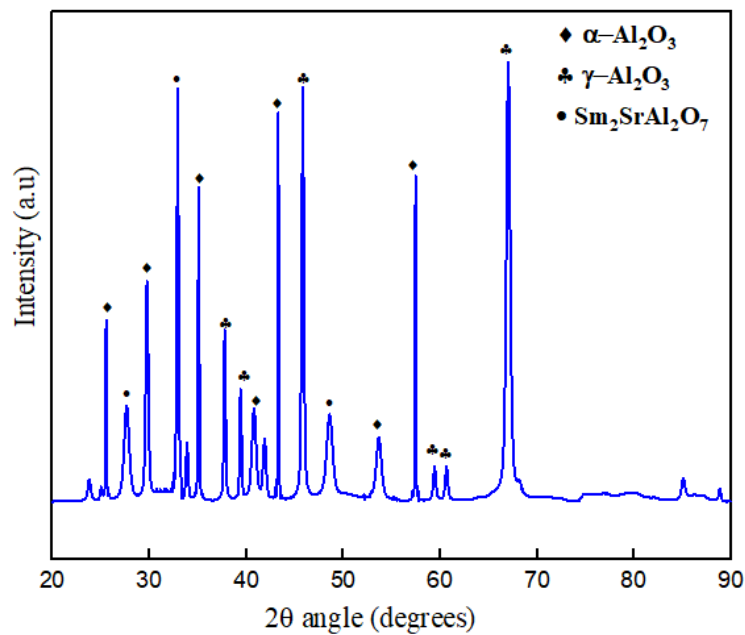


Figure 6.7 Surface XRD pattern of the laser-treated samples

The XRD pattern of the laser-treated surface is shown in Figure 6.7. The fraction of the phases present remained the same as that of as-coated systems with 29.5 % of Sm<sub>2</sub>SrAl<sub>2</sub>O<sub>7</sub>, 53.8 % of γ-Al<sub>2</sub>O<sub>3</sub>, and 16.7 % of α-Al<sub>2</sub>O<sub>3</sub>. It points to the fact that the laser glazing did not influence the phase formation in the considered system. Cases of α-Al<sub>2</sub>O<sub>3</sub> formation upon laser treatment of γ-Al<sub>2</sub>O<sub>3</sub> have been reported, which is not observed in the present study (Moriya et al. 2016). The variation in behavior may be owing to the difference in material composition and surface conditions. Intensity variations in the peaks have been identified, in reflection to the microstructural variations after remelting (Ghasemi et al. 2014; Tsai et al. 2007).

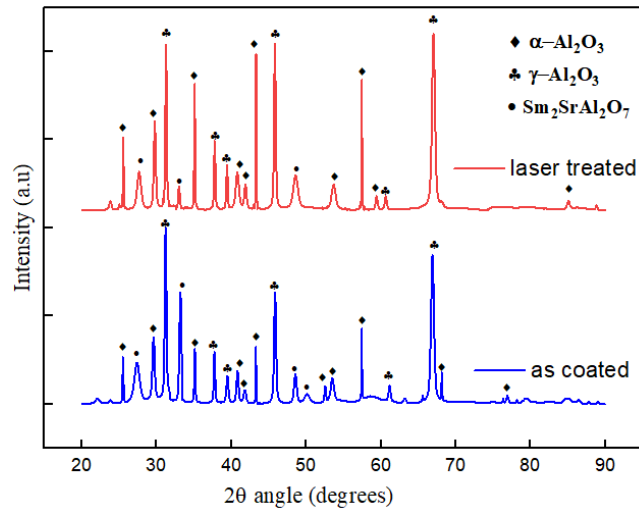


Figure 6.8 Normalized XRD patterns of as-coated and laser-treated sample surfaces

For a better comparison, the normalized XRD plots of the as-coated and laser-treated sample surfaces are shown in Figure 6.8. The SSA peak at  $32.9^\circ$  had a lower intensity after laser treatment, while the  $\alpha\text{-Al}_2\text{O}_3$  peaks at  $57.3^\circ$ ,  $43.2^\circ$ , and  $\gamma\text{-Al}_2\text{O}_3$  peaks at  $45.8^\circ$  showed a higher intensity after laser treatment. It was noticed that the laser-treated samples did not show SSA peaks at  $50.0^\circ$  and  $\alpha\text{-Al}_2\text{O}_3$  peaks at  $52.4^\circ$  and  $68.1^\circ$ . The FWHM values of the major peaks are shown in Table 6.2. Few changes in the FWHM values were noticed in peaks after laser remelting. In the case of  $\gamma\text{-Al}_2\text{O}_3$ , the FWHM values of peaks at  $31.8^\circ$  and  $66.8^\circ$  remained the same, while the peak at  $45.8^\circ$  had a decrease ( $0.307^\circ$  to  $0.256^\circ$ ). The  $\alpha\text{-Al}_2\text{O}_3$  peaks retained the FWHM values after laser treatment. The SSA peaks at  $27.3^\circ$  showed a decrease in FWHM ( $0.819^\circ$  to  $0.614^\circ$ ). Only the SSA peak at  $48.5^\circ$  had an increase in FWHM after laser treatment ( $0.409^\circ$  to  $0.716^\circ$ ). Researchers suggest that laser treatment can make significant changes in the orientation of planes within the system, as seen (Tsai et al. 2007).



Table 6.2 FWHM values of major peaks in as-coated and laser-treated samples

Phases	Position, $2\theta$ (degrees)	FWHM, $\beta$ (degrees)	
		As-coated	Laser-treated
Sm <sub>2</sub> SrAl <sub>2</sub> O <sub>7</sub>	27.3	0.819	0.614
Y-Al <sub>2</sub> O <sub>3</sub>	31.8	0.256	0.256
$\alpha$ -Al <sub>2</sub> O <sub>3</sub>	43.2	0.077	0.077
Y-Al <sub>2</sub> O <sub>3</sub>	45.8	0.307	0.256
Sm <sub>2</sub> SrAl <sub>2</sub> O <sub>7</sub>	48.5	0.409	0.716
$\alpha$ -Al <sub>2</sub> O <sub>3</sub>	57.3	0.077	0.077
Y-Al <sub>2</sub> O <sub>3</sub>	66.8	0.461	0.461

## 6.1 EBSD analysis of laser-treated samples

The EBSD phase map and grain size distribution of laser-treated samples, as in Figure 6.9, also showed similar results as that of as-coated samples. It was confirmed that the laser glazing did not cause major changes in the phase fractions within the top coat. Tao et al. (2020) suggest that a fine-grained microstructure tends to inhibit any probable phase transition during operation. The finer grains in the coating may have assisted in retaining the phases even after the laser treatment. The EBSD analysis of the as-coated samples revealed a finer average grain size of 0.037  $\mu\text{m}$  (37 nm). From the distribution plot, about 98 % of the grains exhibited a single size of 0.03 microns in the as-coated condition. The laser-modified system presented a slight increase in grain size in a fraction of grains. The grain size increases with an increase in laser exposure time. A low-viscosity melt pool formed locally may lead to a larger grain size in ceramics. The plot shows that only about 22 % of the total grains underwent a slight increase in size while the majority of grains retained the size. This can be attributed to the localized grain growth arising from localized melt pools (Liu et al. 2021; Zhang and LeBlanc 2018). Contrary observations with a decrease in grain size are also reported by researchers for YSZ coatings on steel substrate (Reza et al. 2018). The inverse pole

figure of the composite top coat, as shown in Figure 6.10, did not show any preferred orientation. The observation was identical to the as-coated surface.

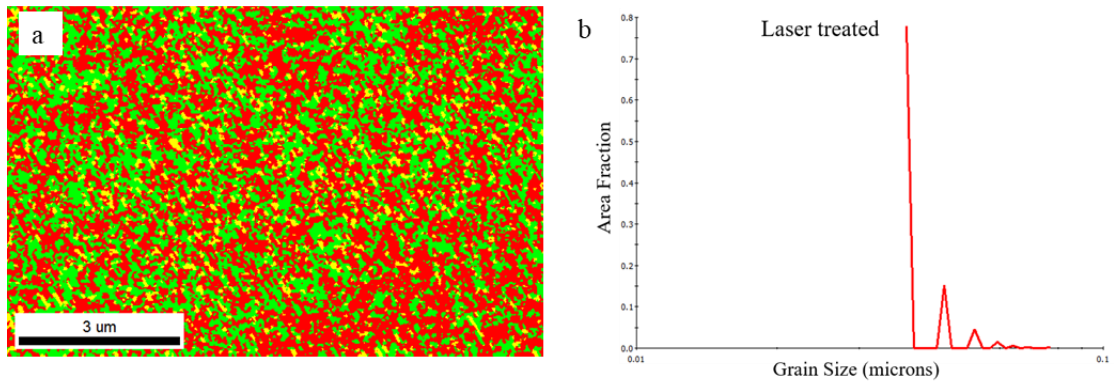


Figure 6.9 a) Phase map and b) grain size distribution of laser-treated samples

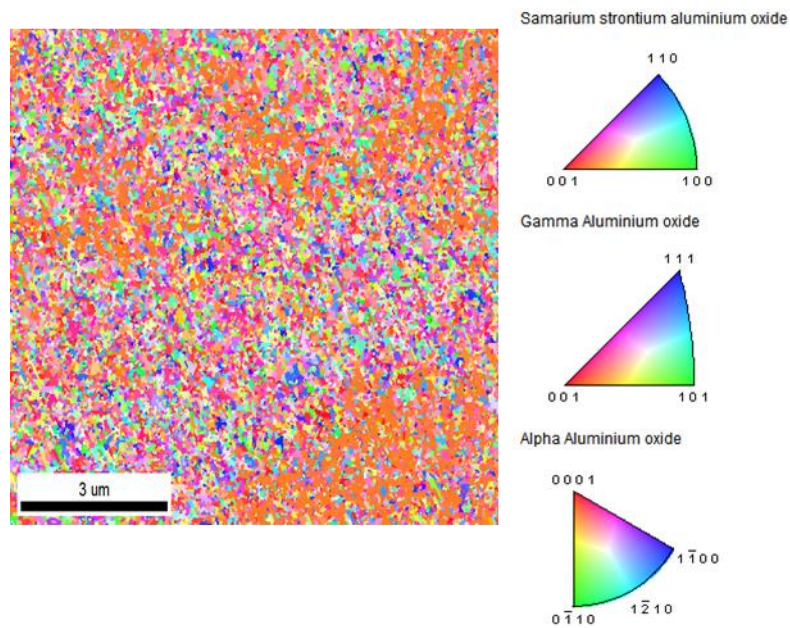


Figure 6.10 Inverse pole figure of laser-treated samples

## 6.2 Mechanical properties of laser-treated samples

The nanoindentation tests were repeated on the laser-treated samples using the same parameters to investigate the variations in the mechanical properties of the system. The measured load depth curve of the laser-treated sample is shown in Figure 6.11.

An average hardness of 12.6 GPa and an increased Young's modulus of 176 GPa were obtained in the laser-treated samples. Multiple measurements were taken and the average value is presented. The 8.7 % better hardness achieved over the as-coated samples is due to the remelting and solidification during laser exposure. A higher improvement in hardness was not obtained, as the alumina phase fractions remained the same after the laser treatment. The alpha phase of alumina being denser in structure, the retention of the alpha phase could have offered a better enhancement in hardness. The melting of protrusions and closure of surface pores are solely responsible for the improvement in hardness. The nearly 15 % increase in Young's modulus reflects the sintering of the 70 wt.%  $\text{Al}_2\text{O}_3$  - 30 wt.%  $\text{Sm}_2\text{SrAl}_2\text{O}_7$  composite coatings that occurred during laser treatment.

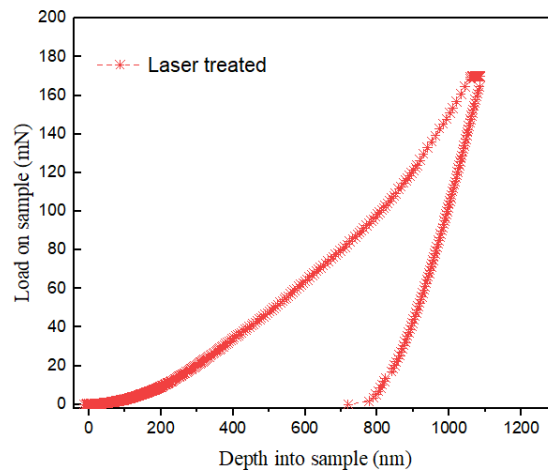


Figure 6.11 Load displacement curves for laser-treated samples measure by nanoindentation

### 6.3 Summary

- The laser-treated samples demonstrated a comparatively smooth surface and the least open porosities than the as-coated surface.
- The phase fractions and distributions of the samples remained the same even after laser exposure.
- The laser-treated samples offered a better hardness of 12.6 GPa and Young's modulus of 176 GPa.



## 7 Oxidation, hot corrosion and erosion behavior of laser-treated samples

### 7.1 Isothermal oxidation behavior of laser-treated samples

The visual inspection of the laser-treated samples after oxidation does not show distinct differences from that of oxidized as-coated samples. A high magnification observation of laser-treated samples after oxidation at 1100 °C showed the presence of surface pores, as in Figure 7.1. Generally, cracks appear on the surface after high temperature exposure, by widening of existing microcracks on the surface. As a considerable fraction of surface microcracks are sealed off during laser treatment, the probability of interconnection and enlargement of microcracks are lower in laser-treated samples. A lower magnitude of cracks and defects can be identified from the morphology of the laser-treated samples, as shown in Figure 7.2. As compared to the laser-treated samples, the as-coated samples had longer cracks on the surface after isothermal oxidation exposure. The measured EDS composition on the oxidized surface is given in Table 7.1.

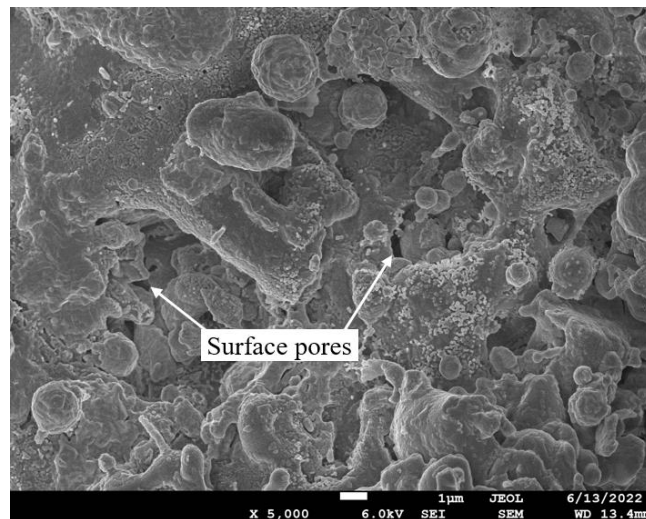


Figure 7.1 Surface image of laser-treated samples after isothermal oxidation at 1100 °C for 150 h

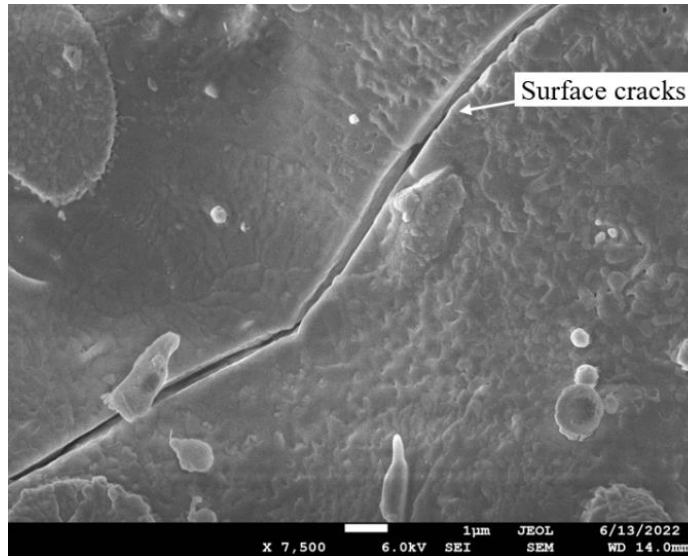
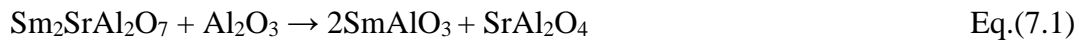


Figure 7.2 Magnified surface image of laser-treated samples after isothermal oxidation test at 1100 °C for 150 h

Table 7.1 Composition of laser-treated sample surfaces after isothermal oxidation tests

Oxidized samples (wt.%)	Sm	Sr	Al	O
Laser-treated	12.0	5.6	37.4	44.8

As inferred from the XRD patterns of the oxidized surfaces (Figure 7.3), the laser-modified samples also presented similar oxidation behavior, with the products  $\text{SmAlO}_3$  and  $\text{SrAl}_2\text{O}_4$  in the diffraction patterns. The mechanisms of dissociation and  $\text{SmAlO}_3$  formation are found to be similar to that in as-coated systems.



The XRD patterns did not show the presence of any spinel oxides on the surface.

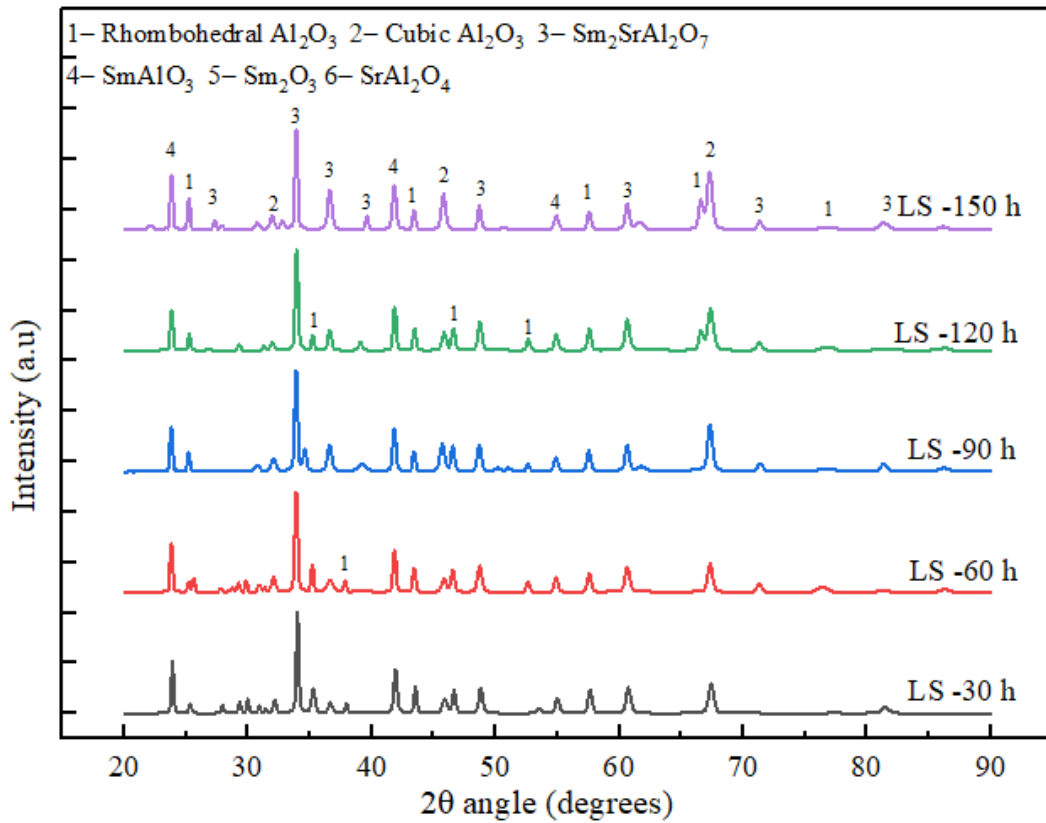


Figure 7.3 XRD patterns of laser modified samples after oxidation for different durations

### 7.1.1 Cross-sectional analysis and TGO formation

The laser treatment seals a prime fraction of the open porosities on the surface, leading to lower oxygen penetration. The lower permeability is assumed to provide a higher oxidation resistance than the as-coated samples. The sample cross-sectional analysis was performed on the oxidized samples and the weight compositions of the top coat and bond coat regions measured in EDS are given in Table 7.2.

The bond coat - top coat interface of the samples (Figure 7.4, Figure 7.5, and Figure 7.6) were viewed in SEM and the average TGO thickness was calculated from measurements at multiple locations. The average oxide thickness in laser-treated samples varied from 2.5  $\mu\text{m}$  to 5.6  $\mu\text{m}$  after exposure at 1100  $^{\circ}\text{C}$  for 30 h and 150 h, respectively. The thickness variation for as-coated samples under similar conditions was from 3  $\mu\text{m}$  to 6.2  $\mu\text{m}$ . The lower TGO growth gained can be directly correlated to the sealing of open porosities. The EDS analysis of the TGO region was measured at the regions marked in the microstructure. The composition was ascertained to be

alumina with weight percentages of Al and O as Al-51 %, O-49 % after 30 h, Al-53 %, O-47 % after 90 h, and, Al-49 %, O-51 % after 150 h of isothermal exposure at 1100 °C.

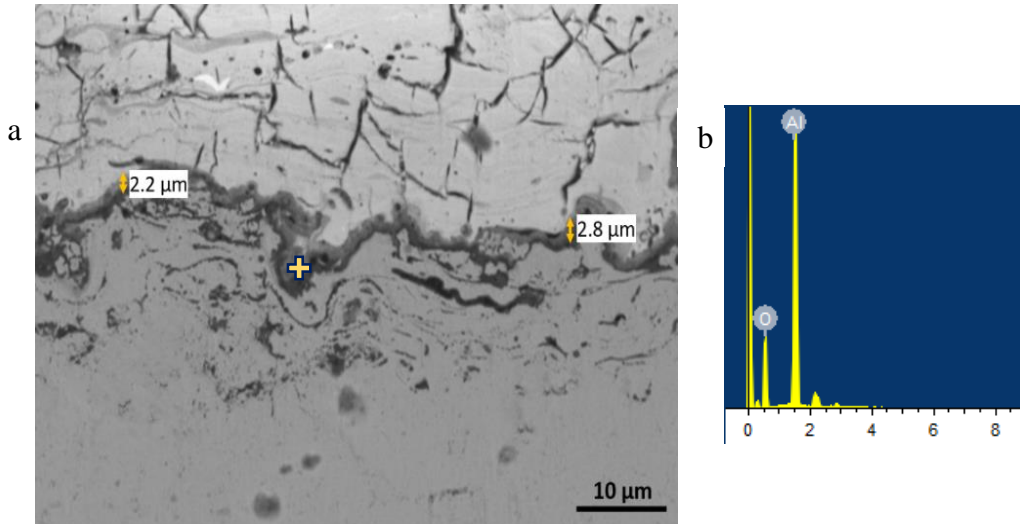


Figure 7.4 a) Cross-section of laser-treated coatings exposed to 30 h oxidation at 1100 °C b) EDS mapping of TGO region

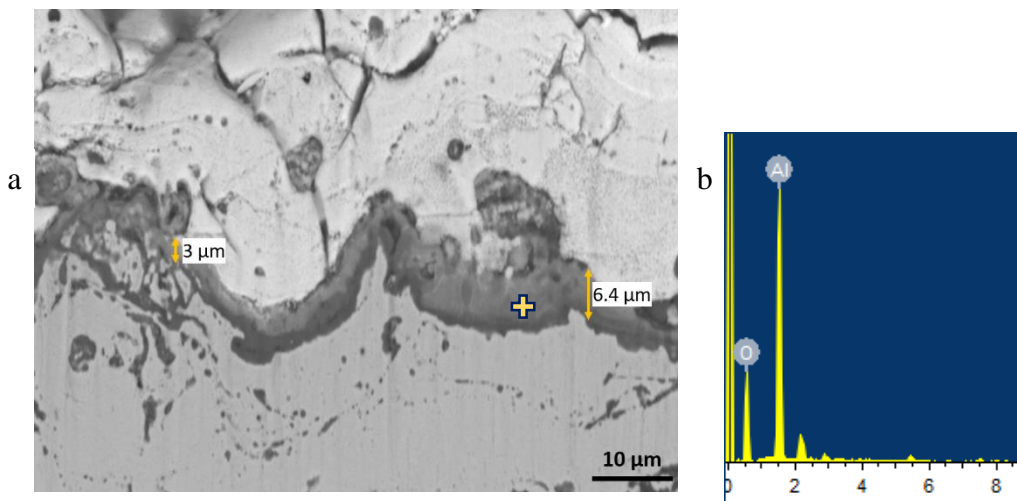


Figure 7.5 a) Cross-section of laser-treated coatings exposed to 90 h oxidation at 1100 °C b) EDS mapping of TGO region



Table 7.2 Composition of as-coated and laser-treated sample cross-section after isothermal oxidation tests

	<b>Oxidized samples</b>	<b>Sm</b>	<b>Sr</b>	<b>Al</b>	<b>O</b>	
Top coat region	As-coated	12.5	4	36.9	46.5	
	Laser-treated	13.1	3.9	37.8	45.2	
		<b>Ni</b>	<b>Cr</b>	<b>Al</b>	<b>Y</b>	<b>O</b>
Bond coat region	As-coated	60.1	20.8	8	1.1	10
	Laser-treated	62.6	21.1	7.2	1.1	8

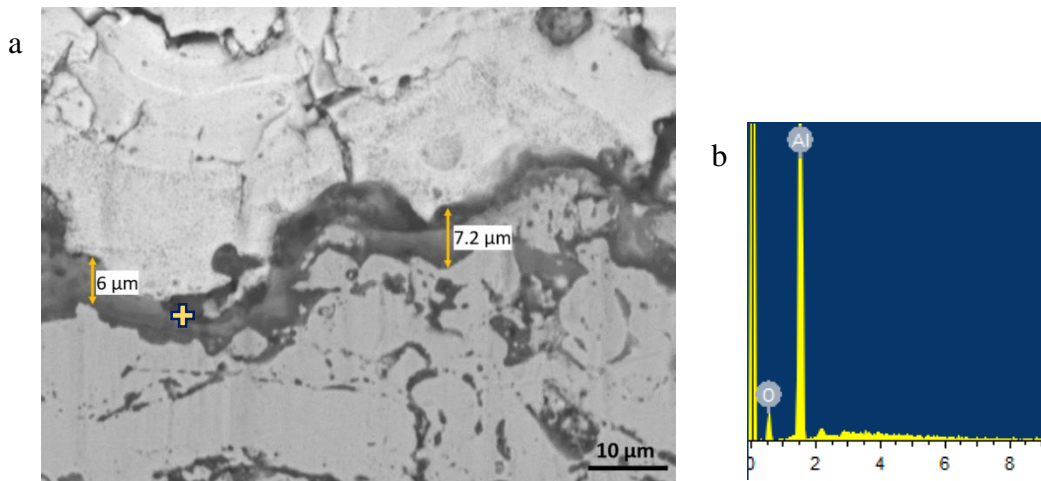


Figure 7.6 a) Cross-section of laser-treated coatings exposed to 150 h oxidation at 1100 °C b) EDS mapping of TGO region

It is worth mentioning that the bond coat - top coat interface of laser-treated samples did not show any notable cracks or lump formation. No failure regions were observed at the interface. It can be assumed that the oxidation interactions were restrained during the complete duration of the tests. Also, the absence of cracks at interface points a limited stress development in the case of laser-treated samples.

### 7.1.2 Kinetics of oxidation of laser-treated samples

The weight gain kinetics of the laser-treated samples demonstrated a parabolic behavior similar to the as-coated samples, as shown in Figure 7.7. The weight gain at every duration was lower in the case of laser-treated samples. This indicates that the laser treatment was able to provide constant, better resistance to oxidation, throughout the test duration. Further, the laser-treated samples showed a comparatively lower

parabolic rate constant ( $k_p = 2.2 \text{ mg}^2\text{cm}^{-4}\text{s}^{-1}$ ) than the as-coated samples ( $k_p = 2.5 \text{ mg}^2\text{cm}^{-4}\text{s}^{-1}$ ), calculated from the slope of the square of weight gain vs exposure time plot, as in Figure 7.8. The magnitude of interactions was higher in the as-coated samples, as higher open porosities were available for oxygen ingress.

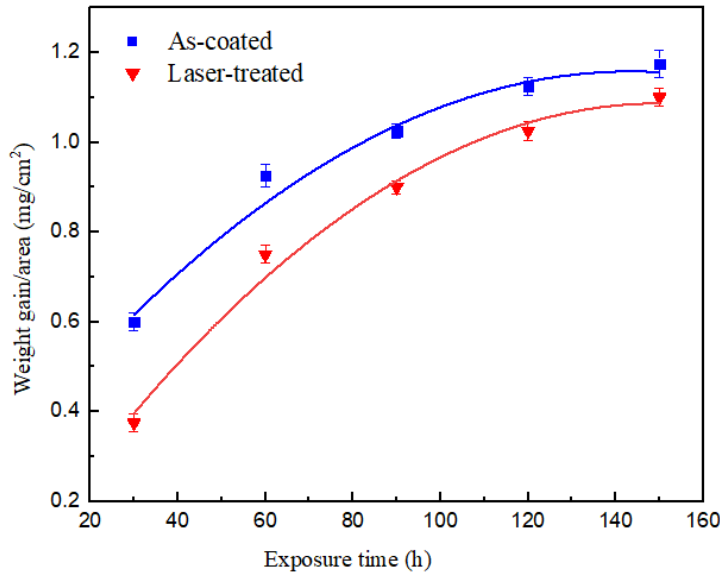


Figure 7.7 a) Weight gain per unit area of laser-treated samples b) Comparison of weight gain between as-coated and laser-treated samples

From the variation in slopes, it can be seen that in both systems, the oxidation weight gain becomes independent of time after 120 h of exposure. The variation in kinetics is due to a continuously decreasing oxygen permeability with exposed time. The specific permeability of oxygen in an alumina matrix increases with temperature. Prior researches report a lower oxygen permeability in alumina than zirconia-based coatings. In the TBC system, the direct transport of oxygen through the composite top coat dominates the ionic diffusion (Fox and Clyne 2004). This direct transfer of oxygen is slightly restricted in laser-treated samples, leading to a lower kinetics.

Tawancy (1998) investigated the performance of a platinum aluminized bond coat on a superalloy substrate, which manifested an initial rapid growth of TGO followed by a reduced rate. A breakaway oxidation with an increase in TGO thickness is reported, due to the breakdown of the non-protective oxide films formed at the interface (Tawancy 1998). The absence of such breakdown oxidation in any of the

considered samples confirms the protectiveness of alumina TGO formed at the interface.

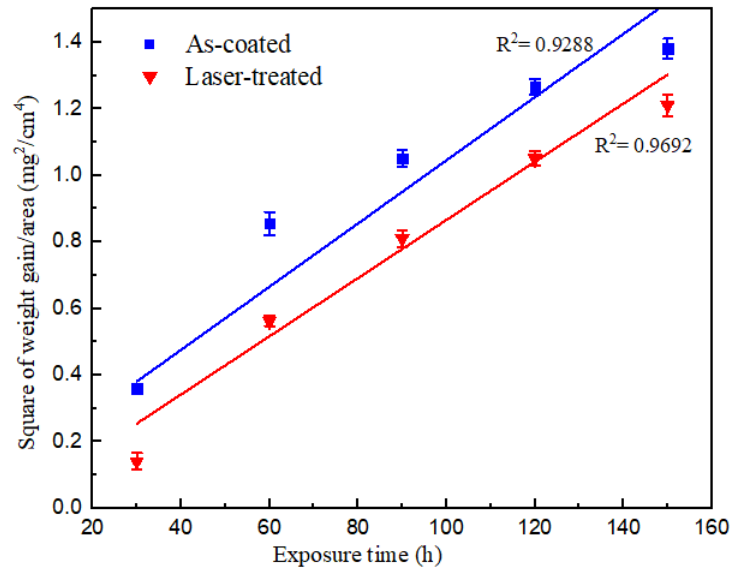


Figure 7.8 Square of weight gain per unit area plotted against time for laser-treated samples

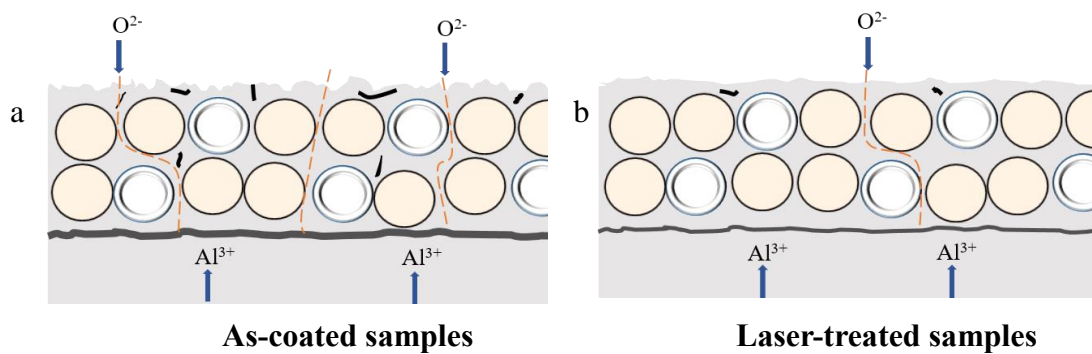


Figure 7.9 Schematic of oxidation in a) as-coated and b) laser-treated samples

Figure 7.9 compares the interaction of oxygen with the coating materials. In the case of as-coated samples (Figure 7.9-a), more open paths were available for oxygen ingress, while a major fraction of the open porosities were “patched up” in the case of laser-treated samples (Figure 7.9-b). The oxygen delivery to the interface is the rate determining step for oxide formation. The lower oxygen delivery led to a lower overall oxygen interaction and lower TGO growth. The lower weight gain and the lower TGO growth in laser-treated samples point to the fact that optimized surface modifications can enhance the oxidation behavior of the coatings.

### 7.1.3 Electrochemical Impedance Spectroscopy (EIS) analysis of laser-treated samples

The EIS test was carried out on the laser-treated samples to investigate the microstructural variations that originated from laser treatment. The EIS plot, as in Figure 7.10, revealed only a single relaxation process similar to as-coated samples. The as-coated top coat offered an impedance of 29067 Ohm.cm<sup>2</sup>, while the laser-treated coating offered a higher impedance of 46333 Ohm.cm<sup>2</sup>. The higher impedance in the laser-treated system is due to the closure of open porosities upon remelting. The values of different circuit elements calculated by fitting to the equivalent circuit are shown in Table 7.3.

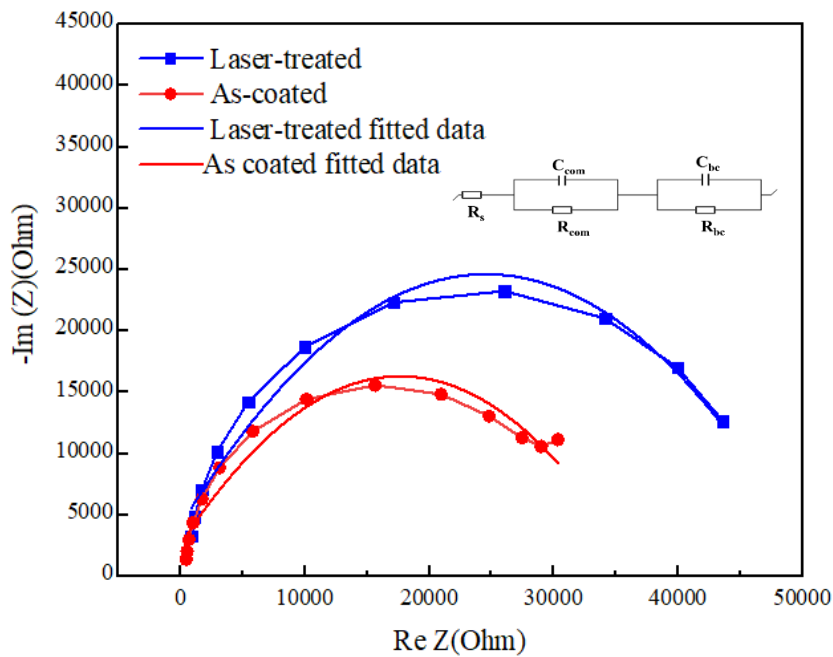


Figure 7.10 Nyquist plots for the as-coated and laser-treated samples

Table 7.3 Obtained values of equivalent circuit elements for laser-treated samples

	$R_s$ (Ohm.cm <sup>2</sup> )	$C_{com}$ ( $\mu F$ cm <sup>-2</sup> )	$R_{com}$ (Ohm.cm <sup>2</sup> )	$C_{bc}$ ( $\mu F$ cm <sup>-2</sup> )	$R_{bc}$ (Ohm.cm <sup>2</sup> )
Laser-treated	623.6	0.4017	46333	65.76	40300

The electrochemical studies prove that the surface resistance of laser-treated samples was superior to the as-coated system, which led to a better oxidation resistance as discovered.



## 7.2 Hot corrosion behavior of laser-treated samples

It is well known that, the surface microstructure of the coating plays a significant role in the hot corrosion behavior of a TBC system. In the present work, a set of samples have been treated with a laser beam as discussed in previous sections.

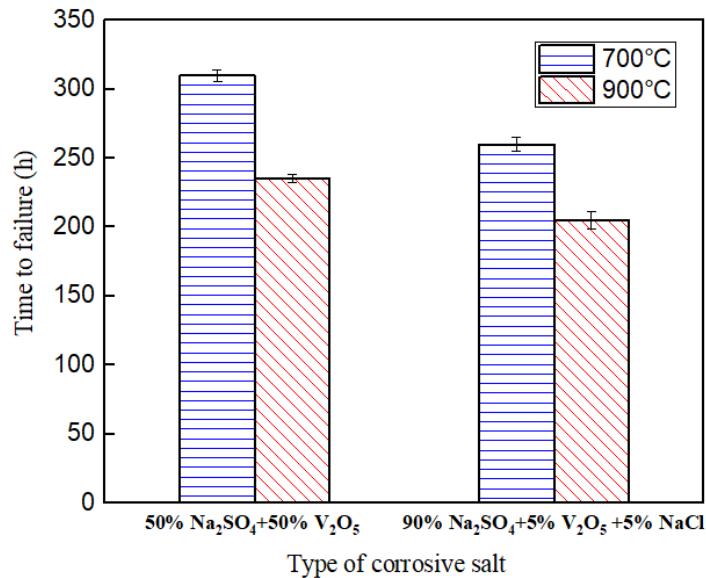


Figure 7.11 Hot corrosion resistances of laser-treated samples in different corrosive conditions

In the interest of a comparison, the laser-treated samples are subjected to the same corrosive conditions (aviation and marine) as the as-coated samples. Figure 7.11 shows the resistance of laser-treated samples in different corrosive salt conditions. It can be seen that in the case of laser-treated TBCs, at 700 °C, the samples exposed to marine conditions showed a 16.1 % lower resistance than the samples exposed to aviation conditions. Similarly, at 900 °C, a 13 % lower resistance is realized for samples in marine atmospheres. The photographs of the laser-treated samples after the hot

corrosion test are shown in Figure 7.12. In most of the conditions, coatings have been chipped off in a major surface area, similar to the as-coated samples.

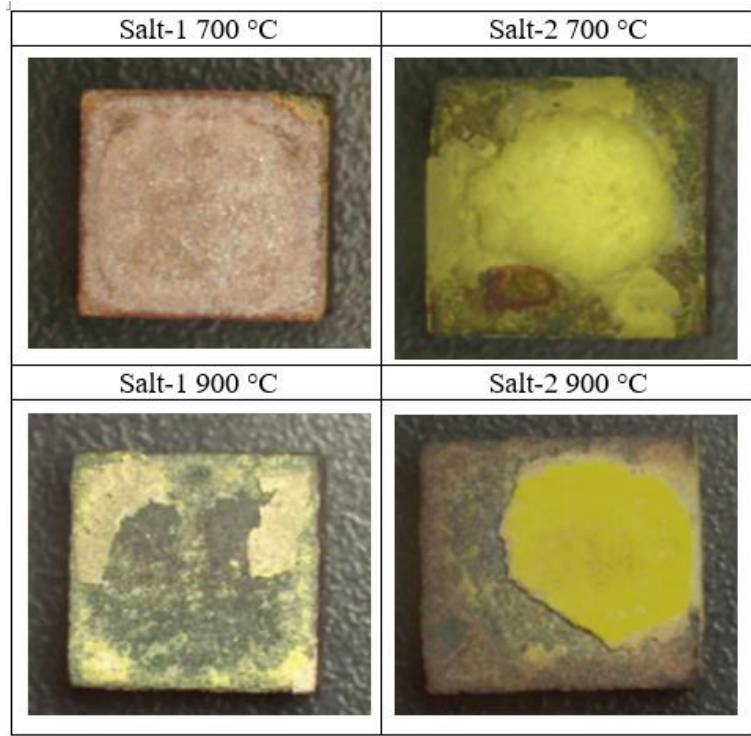


Figure 7.12 Photographs of laser-treated samples after hot corrosion in various conditions

### 7.2.1 Hot corrosion of laser-treated samples in 50 %wt. $\text{Na}_2\text{SO}_4$ + 50 %wt. $\text{V}_2\text{O}_5$ at 700 °C and 900 °C

#### *Samples at 700 °C*

The XRD pattern of the laser-treated sample exposed to aviation conditions at 700 °C is shown in Figure 7.13. The peaks corresponding to corrosion products  $\text{SmAlO}_3$ ,  $\text{SmVO}_4$ ,  $\text{AlVO}_4$ ,  $\text{SrAl}_2\text{O}_4$ , and  $\text{NaAlO}_2$  have been identified on the surface of the coating. The  $\text{SmAlO}_3$  formed from the decomposition of the top coat showcased the dominating peak in the pattern. It is worth mentioning that, the material composition being the same, the products that evolved are identical to that in the case of as-coated samples. The microstructure examination showed rod-like structures developed on the surface (Figure 7.14). The compositional analysis confirmed the rods as  $\text{SmVO}_4$  (Table



7.4). In the case of as-coated samples in the same atmosphere, needle-like structures of  $\text{SmVO}_4$  were identified instead of the rods. The mechanism of  $\text{SmVO}_4$  formation is discussed in earlier sections.

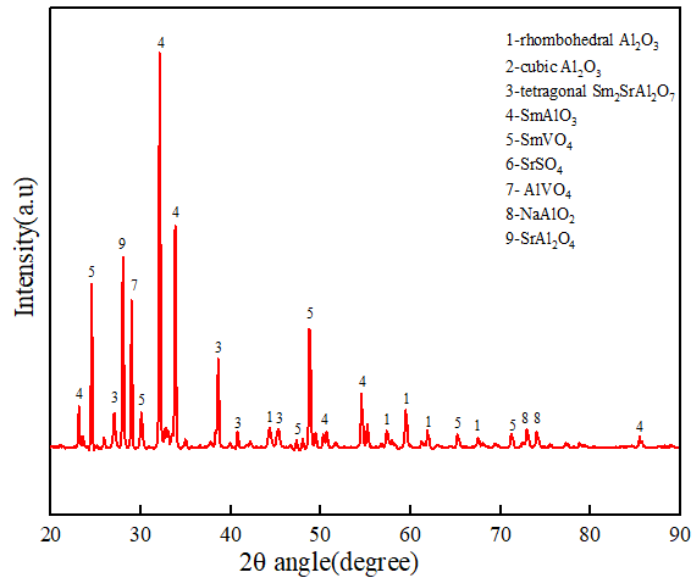


Figure 7.13 XRD pattern of laser-treated sample exposed to 50 % wt  $\text{Na}_2\text{SO}_4$  + 50 % wt  $\text{V}_2\text{O}_5$  at 700 °C

Comparing the performances, under an aviation environment with high vanadates, the laser-treated samples showed a 12.7 % higher resistance than the as-coated samples at 700 °C.

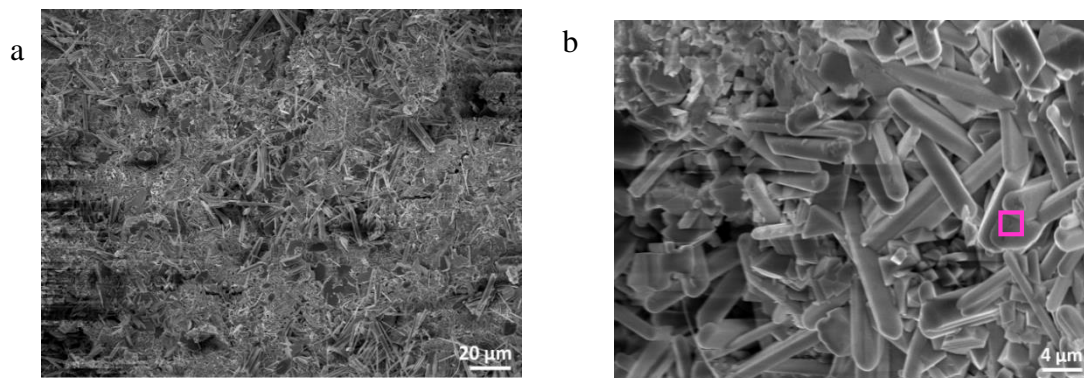


Figure 7.14 The SEM morphology of laser-treated samples exposed to 50 % wt  $\text{Na}_2\text{SO}_4$  + 50 % wt  $\text{V}_2\text{O}_5$  at 700 °C showing  
a) Low magnification image of corroded surface  
b) High magnification image of the hot corrosion products formed on surface

Table 7.4 Composition of the products formed on laser-treated samples exposed to aviation conditions at 700 °C

Element	Sm	Sr	Al	O	Na	S	V
wt. %	57.1	0.00	0.00	23.80	0.00	0.00	19.00

### Samples at 900 °C

The XRD pattern of the laser-treated sample exposed to 50 %wt. Na<sub>2</sub>SO<sub>4</sub> + 50 %wt. V<sub>2</sub>O<sub>5</sub> at 900 °C is shown in Figure 7.15. The corrosion products SmAlO<sub>3</sub>, SmVO<sub>4</sub>, AlVO<sub>4</sub>, SrAl<sub>2</sub>O<sub>4</sub>, and NaAlO<sub>2</sub> have been identified on the surface of the coating, with the SmVO<sub>4</sub> peak showing the highest intensity. Under these conditions, though the primary product SmVO<sub>4</sub> was common in both the as-coated and laser-treated samples, the laser samples contained NaAlO<sub>2</sub> and SrAl<sub>2</sub>O<sub>4</sub> which was not found in the as-coated sample.

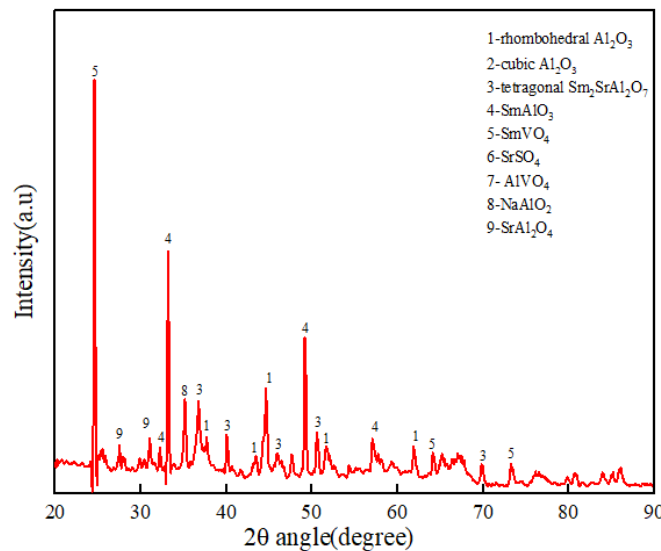


Figure 7.15 XRD pattern of laser-treated sample exposed to 50 %wt Na<sub>2</sub>SO<sub>4</sub> + 50 %wt V<sub>2</sub>O<sub>5</sub> at 900 °C

The high magnification images of the corroded surface (Figure 7.16) showed cuboidal structures of SmVO<sub>4</sub>, with the composition listed in Table 7.5. The as-coated samples in the same environment presented cuboidal and pyramidal structures with a higher size than in laser-treated samples. On a whole, the laser-treated samples

possessed a 9.3 % higher resistance than as-coated samples in aviation conditions at 900 °C.

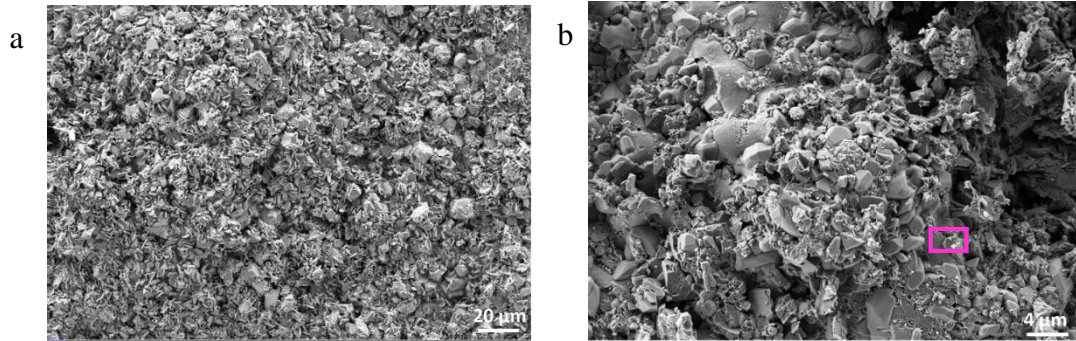


Figure 7.16 The SEM morphology of laser-treated samples exposed to 50 %wt Na<sub>2</sub>SO<sub>4</sub> + 50 %wt V<sub>2</sub>O<sub>5</sub> at 900 °C showing  
a) Low magnification image of corroded surface  
b) High magnification image of the hot corrosion products formed on surface

Table 7.5 Composition of the products formed on laser-treated samples exposed to aviation conditions at 900 °C

Element	Sm	Sr	Al	O	Na	S	V
wt. %	56.08	0.00	0.00	23.71	0.00	0.00	20.23

As in Figure 7.17, Raman spectroscopy of the corroded surfaces was examined to confirm the products formed. The peaks of SmVO<sub>4</sub> and SmAlO<sub>3</sub> were identified in the spectrum, in agreement with the XRD patterns.

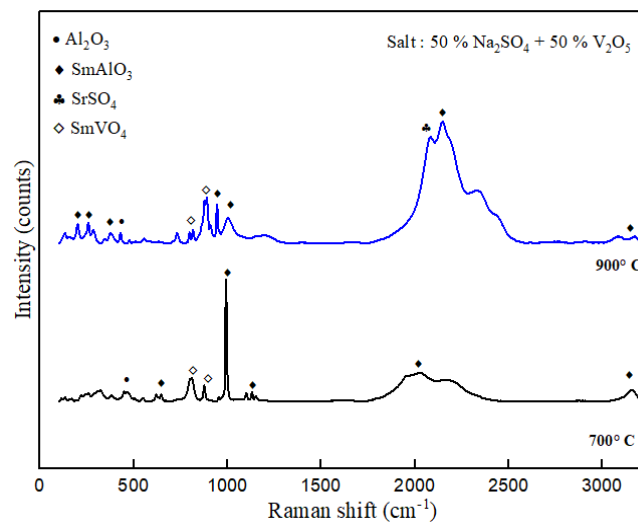


Figure 7.17 Raman spectrum of laser-treated samples after hot corrosion tests at 50 % wt. Na<sub>2</sub>SO<sub>4</sub> + 50 % wt. V<sub>2</sub>O<sub>5</sub> at 700 °C and 900 °C

## 7.2.2 Hot corrosion of laser-treated samples in 90 %wt. Na<sub>2</sub>SO<sub>4</sub> + 5 %wt. V<sub>2</sub>O<sub>5</sub> + 5 wt.% NaCl at 700 °C and 900 °C

### Samples at 700 °C

The XRD pattern of the laser-treated samples exposed to marine conditions (90 % wt. Na<sub>2</sub>SO<sub>4</sub> + 5 %wt. V<sub>2</sub>O<sub>5</sub> + 5 %wt. NaCl) at 700 °C is shown in Figure 7.18. The XRD pattern showed peaks corresponding to Al<sub>2</sub>O<sub>3</sub>, SSA, SmAlO<sub>3</sub>, SmVO<sub>4</sub>, AlVO<sub>4</sub>, NaAlO<sub>2</sub> and SrSO<sub>4</sub>. The compounds SrSO<sub>4</sub> and AlVO<sub>4</sub> presented higher intensities than the rest. Similar to the as-coated samples, the higher sulphate content in the marine corrosive salt may have led to the formation of SrSO<sub>4</sub> in this case. The high magnification images of the corrosion products showcased a mixture of rods and smaller cuboidal-shaped SrSO<sub>4</sub> (Figure 7.19). The Table 7.6 shows the composition of the corrosion products measured by EDS in the regions shown.

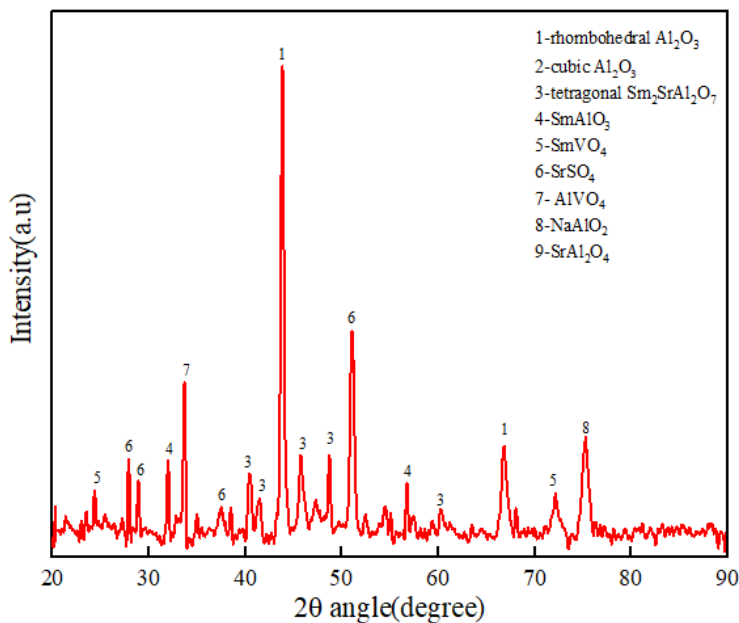


Figure 7.18 XRD pattern of laser-treated sample exposed to 90 % wt Na<sub>2</sub>SO<sub>4</sub> + 5 % wt V<sub>2</sub>O<sub>5</sub> + 5 %wt NaCl at 700 °C

Table 7.6 Composition of the products formed on laser-treated samples exposed to marine conditions at 700 °C

Element	Sm	Sr	Al	O	Na	S	V	Cl
wt. %	0.00	47.93	0.00	35.06	0.00	17.00	0.00	0.00

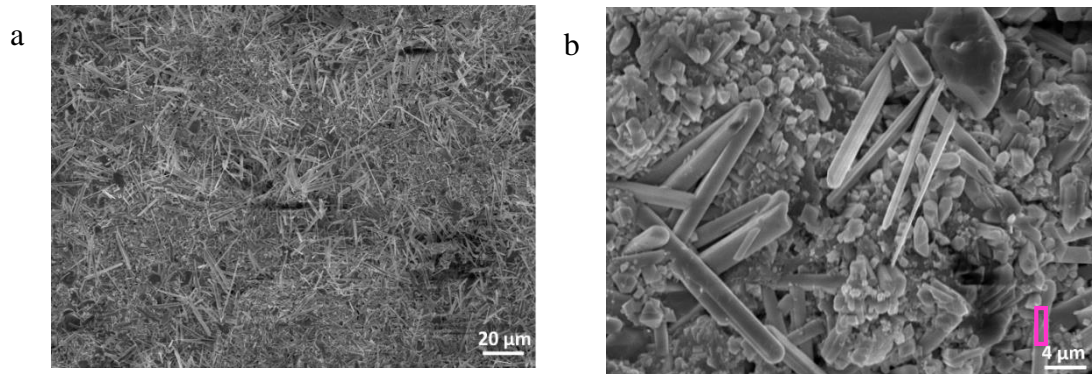


Figure 7.19 The SEM morphology of laser-treated samples exposed to 90 % wt.  $\text{Na}_2\text{SO}_4$  + 5 % wt.  $\text{V}_2\text{O}_5$  + 5 % wt.  $\text{NaCl}$  at 700 °C showing  
a) Low magnification image of corroded surface,  
b) High magnification image of the hot corrosion products formed on surface

### *Samples at 900 °C*

The XRD pattern of the laser-treated samples after hot corrosion in 90 % wt.  $\text{Na}_2\text{SO}_4$  + 5 % wt.  $\text{V}_2\text{O}_5$  + 5 % wt.  $\text{NaCl}$  at 900 °C is shown in Figure 7.20. Besides the top coat peaks  $\text{Al}_2\text{O}_3$  and SSA, corrosion-evolved  $\text{SmAlO}_3$ ,  $\text{SmVO}_4$ ,  $\text{NaAlO}_2$ , and  $\text{SrSO}_4$  were detected. The dissociation component  $\text{SmAlO}_3$  dominated the peak intensity. The high magnification SEM images showed a more damaged surface in the chloride environment. Rod-like and block-like  $\text{SrSO}_4$  have been identified in the microstructure as shown in Figure 7.21. The Table 7.7 comprises the composition of the areas marked in the corrosion products.

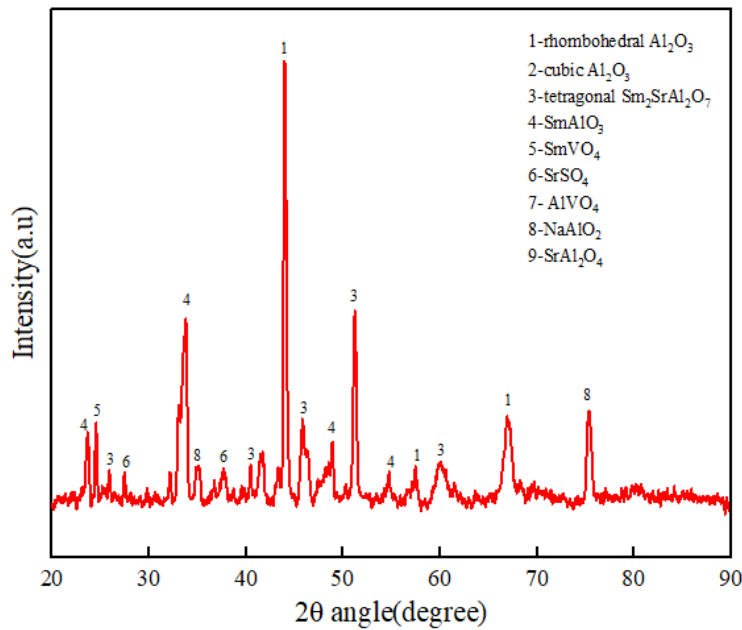


Figure 7.20 XRD pattern of laser-treated sample exposed to 90 % wt.  $\text{Na}_2\text{SO}_4$  + 5 % wt.  $\text{V}_2\text{O}_5$  + 5 % wt.  $\text{NaCl}$  at 900 °C

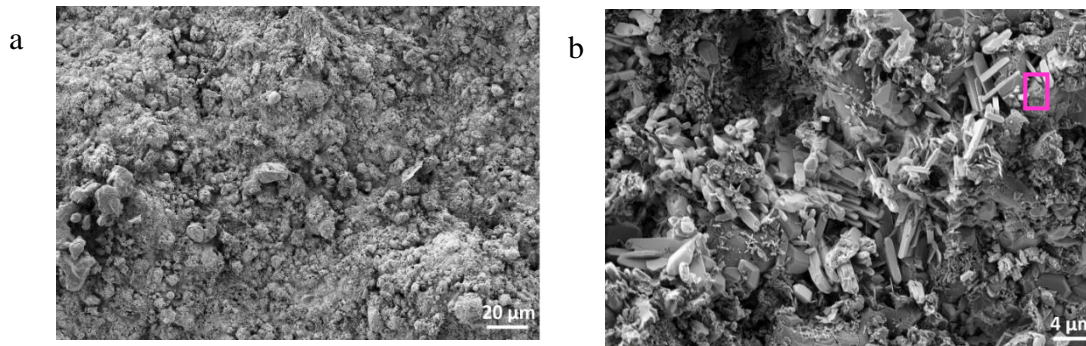


Figure 7.21 The SEM morphology of laser-treated samples exposed to 90 % wt.  $\text{Na}_2\text{SO}_4$  + 5 % wt.  $\text{V}_2\text{O}_5$  + 5 % wt.  $\text{NaCl}$  at 900 °C showing  
a) Low magnification image of corroded surface  
b) High magnification image of the hot corrosion products formed on surface

Table 7.7 Composition of the products formed on laser-treated samples exposed to marine conditions at 900 °C

Element	Sm	Sr	Al	O	Na	S	V	Cl
wt. %	0.00	47.33	0.00	34.37	0.00	18.26	0.00	0.00

The Raman spectrum of the laser-treated samples after hot corrosion is shown in Figure 7.22. It can be seen that the obtained Raman peaks were similar to that of the as-coated samples. The presence of SrSO<sub>4</sub> peaks is confirmed in agreement with EDS and XRD observations.

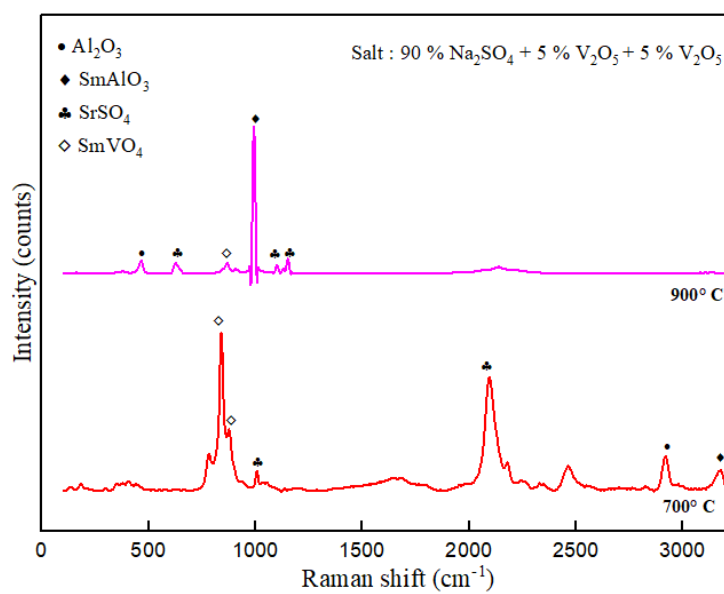


Figure 7.22 Raman spectrum of laser-treated samples after hot corrosion tests at 90 % wt Na<sub>2</sub>SO<sub>4</sub> + 5 % wt V<sub>2</sub>O<sub>5</sub> + 5 % wt NaCl at 700 °C and 900 °C

Comparing the performance of as-coated and laser-treated 70 wt.% Al<sub>2</sub>O<sub>3</sub> - 30 wt.% Sm<sub>2</sub>SrAl<sub>2</sub>O<sub>7</sub> samples, the laser-treated samples showed a better resistance to hot corrosion. At higher temperatures, the corrosive salt melt have a sufficiently low viscosity to penetrate through the open porosities and cracks on the surface of as-coated samples. The closure of porosities further led to higher hot corrosion resistance in the developed composite coatings. The laser treatment and subsequent reduction in roughness lead to a reduced specific surface area exposed to corrosive salts. Similar behavior of coatings has been reported by earlier researchers. In the case of YSZ coatings, the laser-treated samples offered a higher life with YVO<sub>4</sub> and m-ZrO<sub>2</sub> as corrosion products in laser-treated and thermal sprayed samples. In the morphology of laser-treated samples, few microcracks were present. Microcracks on laser-glazed YSZ are reported to provide an easy path for molten corrosive infiltration (Guo et al. 2020; Reza et al. 2018). On the other hand, if the cracks are completely removed, the glazed layer may tend to spall during operation, suffering from a lower strain tolerance.

Overall, the surface modification has offered a better hot corrosion resistance to the TBC system. Optimizing the laser treatment to eradicate any surface defect can lead to a better hot corrosion behavior of the composite coatings.



### 7.3 Solid particle erosion behavior of laser-treated samples

The erosion behavior of the as-coated samples under various conditions is discussed in section 5.3. The laser-treated samples are exposed to similar conditions to monitor the changes in erosion response after surface modification. The erosion tests have been carried out at 200 °C and 800 °C with erodent impact angles 30° and 90°, as in the case of as-coated samples. The parameters and erodents used are kept constant, for the interest of comparison. The eroded samples have been analyzed in detail to examine the erosion mechanisms involved.

#### 7.3.1 Macroscopic observation of eroded samples

The photographic images of the laser-treated composite coatings after the erosion test are shown in Figure 7.23. Visual inspection of the samples after 25 min of erosion presented scars with similar geometry to the as-coated samples, with nearly circular scars at 90° and elliptical scars at a 30° impact angle. A major part of the laser-treated composite layer was removed exposing the bond coat.

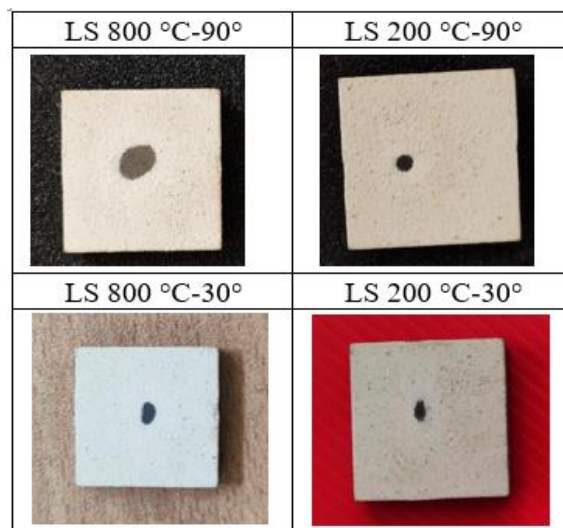


Figure 7.23 Photographic images of laser-treated samples exposed to erosion under various conditions

The dimensions of the scars measured using a surface profilometer are reported in Table 7.8. The samples exposed to 800 °C showed larger scars than the samples at 200 °C. For the samples exposed at a 30° impact angle, the length of the major axis is found to vary from 2.50 mm to 3.19 mm. In the case of 90° impact angle, the scar

diameter varied from 1.88 mm to 3.44 mm. It is noticed that in all the tested conditions, the scars in laser-treated samples were comparatively smaller than the scars produced in the as-coated samples. The variation can be correlated to the difference in surface characteristics.

Table 7.8 Scar dimensions of laser-treated samples exposed to various conditions measured in surface profilometer

		LS-800 °C	LS-200 °C
<b>Elliptical Scar</b> (30°)	Major Diameter (mm)	3.19	2.50
	Minor Diameter (mm)	2.10	1.56
<b>Circular Scar</b> (90°)	Scar Diameter (mm)	3.44	1.88

### 7.3.2 Cumulative erosion mass loss and average erosion values

The cumulative mass loss against the cumulative mass of erodent impacted on the laser-treated samples at 200 °C and 800 °C is shown in Figure 7.24. As discussed in earlier section 5.3.2, under constant erosion conditions, the cumulative weight loss increases with erosion time and the mass of erodents impacted. The mass monitoring of laser-treated samples also showed an overall trend of increasing weight loss on increasing erodent mass impacted. The highest mass loss was found at 800 °C at a 90° impact angle.

Figure 7.25 shows the comparison of cumulative weight loss in laser-treated and as-coated samples. It is to be noted that the weight loss plot followed a parallel pattern with a higher erosion rate followed by a steady state erosion. The as-coated surface comprised of open porosities and unmolten particles, which are sealed and melted in the case of laser-treated samples. This may have led to a lower erosion weight loss in the case of laser-treated samples than the as-coated samples in all conditions tested. The poorly bonded particles and lamellas on the surface are the first ones to be removed by erosion. These features get fractured easily and are removed upon initial particle impact

events (Presby and Harder 2021). As the surface asperities and protrusions have been melted, the initial weight loss of the laser-treated samples is lower than the initial weight loss in as-coated samples. The weight loss curves for the first 5 min of erosion (15 g of erodent) for all the samples are shown in Figure 7.25-b. It can be noticed that the slope of the initial region, is always lower for laser-treated samples than for as-coated samples exposed to the same conditions. The slope of the initial regions, calculated through OriginLab software is mentioned in Table 7.9.

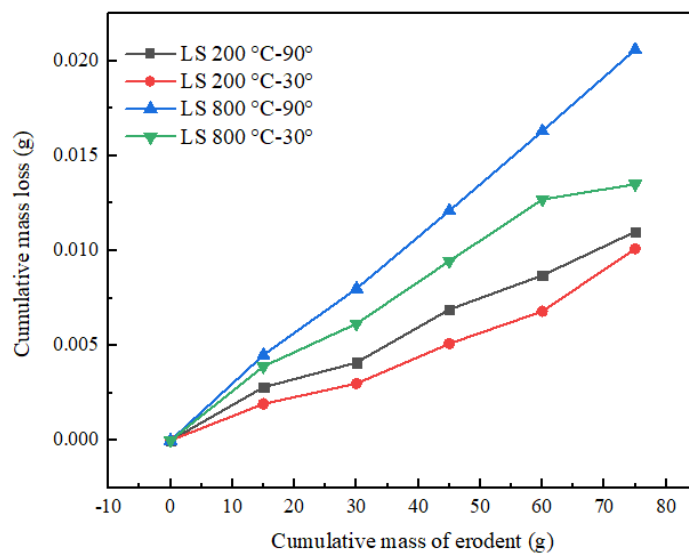


Figure 7.24 Graph showing cumulative mass loss of coating vs cumulative mass of erodents for laser-treated samples exposed at 200 °C and 800 °C

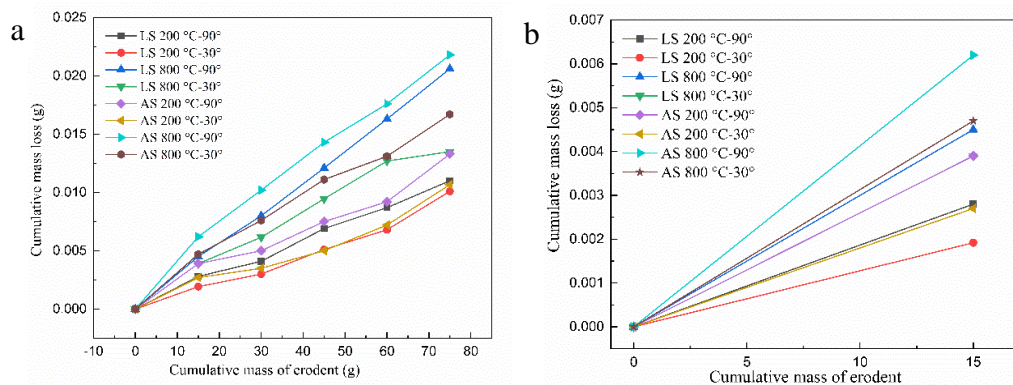


Figure 7.25 a) Comparison of cumulative mass loss in as-coated and laser-treated samples b) Initial weight loss of as-coated and laser-treated samples

Table 7.9 Initial slope of cumulative weight loss plot in as-coated and laser-treated samples

Erosion Conditions	Initial slope ( $\times 10^{-4}$ )	
	As-coated samples	Laser-treated samples
200 °C- 30°	1.80	1.28
200 °C- 90°	2.60	1.86
800 °C- 30°	3.13	2.60
800 °C- 90°	4.13	3.00

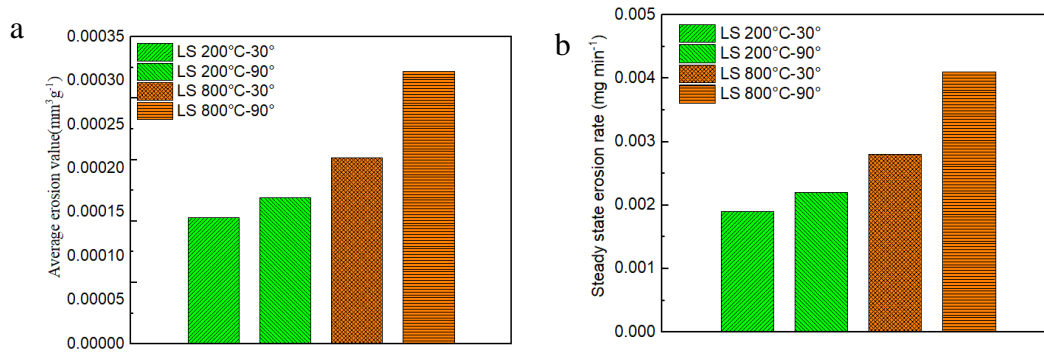


Figure 7.26 Plots showing a) average erosion values and b) steady state erosion rate of laser-treated samples at different conditions

The average erosion values of laser-treated samples under various erosion conditions are calculated according to the ASTM standard specified (Figure 7.26). The average erosion value for laser-treated samples was the highest at 800 °C at a 90° impact angle. The steady-state erosion rate follows a similar pattern to average erosion, with the highest at 800 °C at a 90° impact angle and lowest in samples at 200 °C and 30° impact angle. The average erosion value and steady-state erosion rate calculated at each temperature are higher at 90° than at a 30° angle, due to the higher energy in a normal impact.

### 7.3.3 Microstructural changes and erosion response of laser-treated samples

The erosion response of a coating is dependent on the microstructural properties of the system. It is reported that a columnar structured EB-PVD coating possesses 10-fold higher erosion resistance than the lamellar structured APS coating. In the case of

plasma sprayed coatings, the cracks may easily propagate around the splat boundaries through a network of cracks and pores leading to material removal (Caroline 2021). Also, the open porosities in the morphology have a significant role in erosion behavior. The laser-treated samples showed a better erosion resistance than the as-coated system due to the sealing of porosities upon re-melting. The laser remelting may contribute to the closing of the existing microcracks on the surface. In ceramic coatings, the quenching stress is often relieved by splat microcracking. These flaws degrade the erosion resistance, paving the way for chipping of the coating upon erodent impact (Ramm et al. 1993). In the considered systems, the morphology of the laser-treated samples had only very fine microcracks as shown in earlier sections. The presence of segmented cracks in laser-treated YSZ TBC has been reported (Tsai et al. 2007).

The surface profilometric images of the laser-treated and as-coated sample surfaces are shown in the previous sections. The as-coated surface possessed a surface roughness of 6.0  $\mu\text{m}$ , while the laser-modified surface showed a 33 % lower roughness of 4.0  $\mu\text{m}$ . The primary erosion response of the coating system is highly dependent on the initial surface roughness of the coating, which is due to semi-molten on unmolten particles. The more completely molten particles enhance the intersplat bonding, reduces porosity, and improve roughness. A reduced roughness reduces the effective area of contact with the abrasive particle jet (Wang et al. 2014). During laser glazing, many protrusions or unmelted particles on the surface may remelt, forming a smoother surface. It is evident that at 200 °C and 800 °C, the samples with a higher roughness had a higher erosion at both 30° and 90°. The poorly bonded unmolten particles, surface protuberances and asperities on the as-coated surface are rapidly fractured and removed by the onset of erosion (Presby and Harder 2021).

The laser-treated samples achieved a 8.7 % better hardness of 12.6 GPa, by virtue of remelting and solidification. Up to 3 fold improvement in hardness is reported by researchers on optimizing the laser modification (Tsai et al. 2007). As mentioned in section 6.2, a higher improvement in hardness was not achieved, as the alumina phase fractions remained the same after laser treatment. The improvement obtained is completely due to the sintering from the melting of protrusions and closure of surface

pores. It is to be noted that besides the material hardness, the indentation on plasma sprayed coating depends on the lamellar microstructure, splats, and porosities.

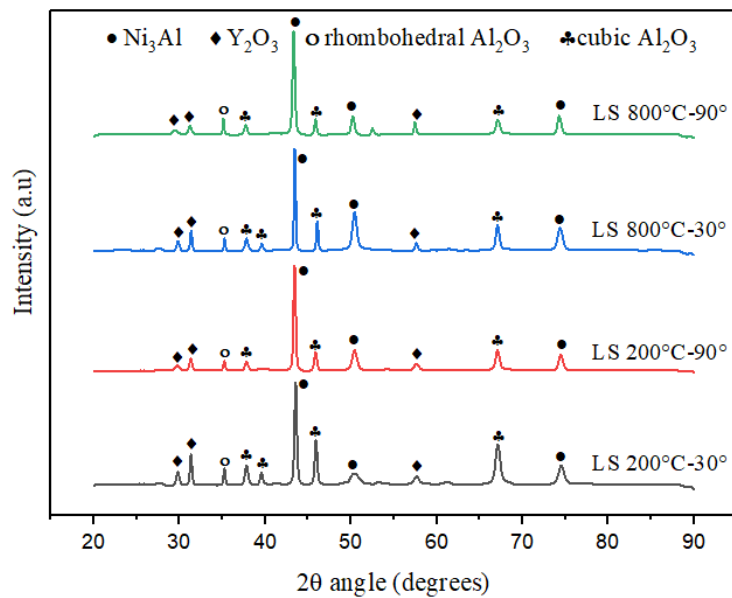


Figure 7.27 XRD patterns of scars in laser-treated samples eroded at various conditions

From the visual observation of samples, bond coat was visible in the scar areas. The XRD pattern of the scar areas (Figure 7.27) presented peaks of both top and bond coat elements, which was similar to the as-coated samples. Only minor variations in the intensity and width of the peaks were identified between the samples. A higher FWHM value for the peak at 43.4° was seen for samples at 800 °C than the samples at 200 °C. The lowest FWHM value (0.154) was in the laser-treated samples at 800 °C at 30° impact angle. So a higher stress development at high temperatures can be confirmed in the case of laser-treated samples also.

The profilometric views of the eroded areas in laser-treated samples are shown in Figure 7.28. At both impact angles, the samples at higher temperatures showed larger scar areas. The order of the scar area remained the same as that of the laser-treated samples with the maximum area of scar at 800 °C and 90° while the lowest area was at 200 °C and 30° impact angle. The overall profile of the scars was in reflection to the average erosion values calculated.

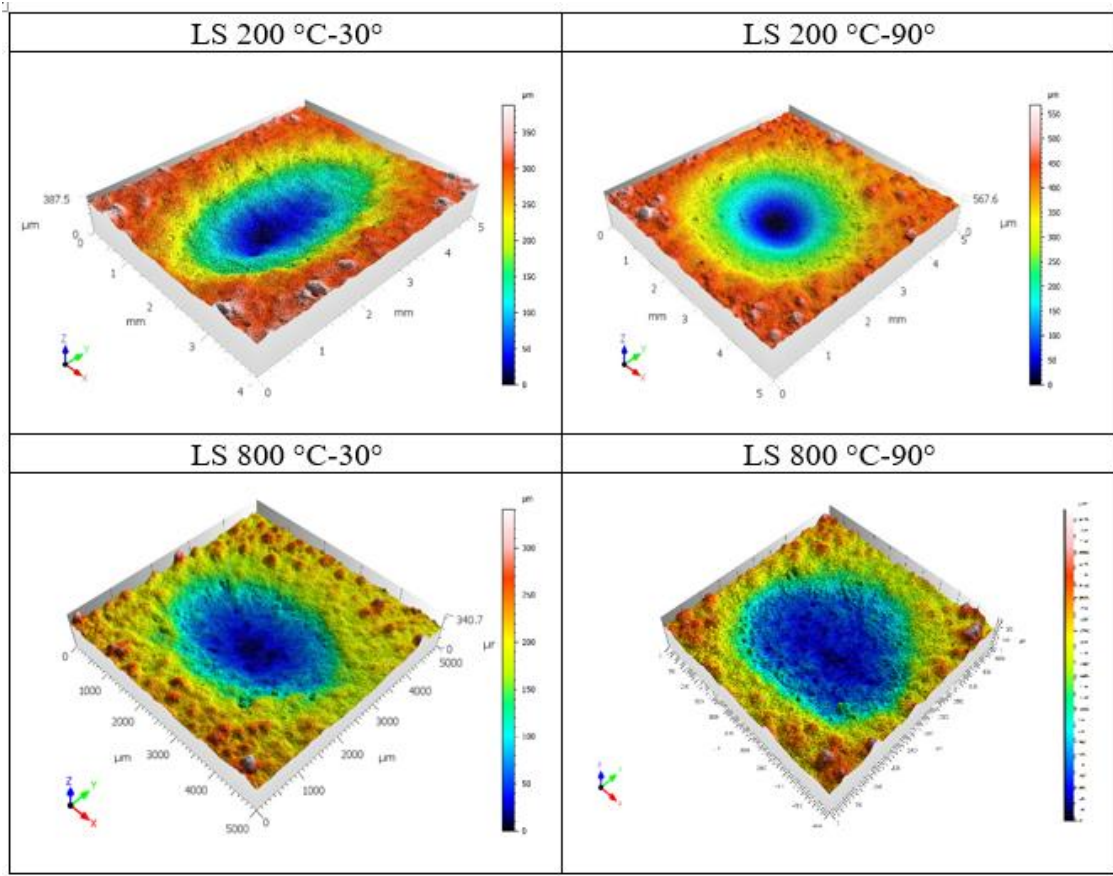


Figure 7.28 Profilometric view of eroded areas in laser-treated samples

The microstructures of the erosion scars examined are shown in Figure 7.29. The microstructure showed similar mechanisms of material removal such as crater, microcutting, and ploughing. At 800 °C, larger ploughing marks were noticed at 30° impact while deeper craters are present at 90°. Shallow craters and ploughing marks were visible in scars of samples exposed to 200 °C. The magnitude of removal mechanisms at every conditions or the damage to the microstructure was slightly lower than that in the case of as-coated samples. At higher temperature, the material allowed a deeper impact. Also, a higher ductility is observed at higher temperature, even though any clinging of erodents in the target microstructure was not detected, even in laser-treated samples. A comparison of the as-coated and laser-treated samples shows that there are no remarkable differences in the failure mechanisms between the two. Figure 7.30 shows the overall mechanisms and magnitudes noticed in as-coated and laser-treated samples at 800 °C at 90°.

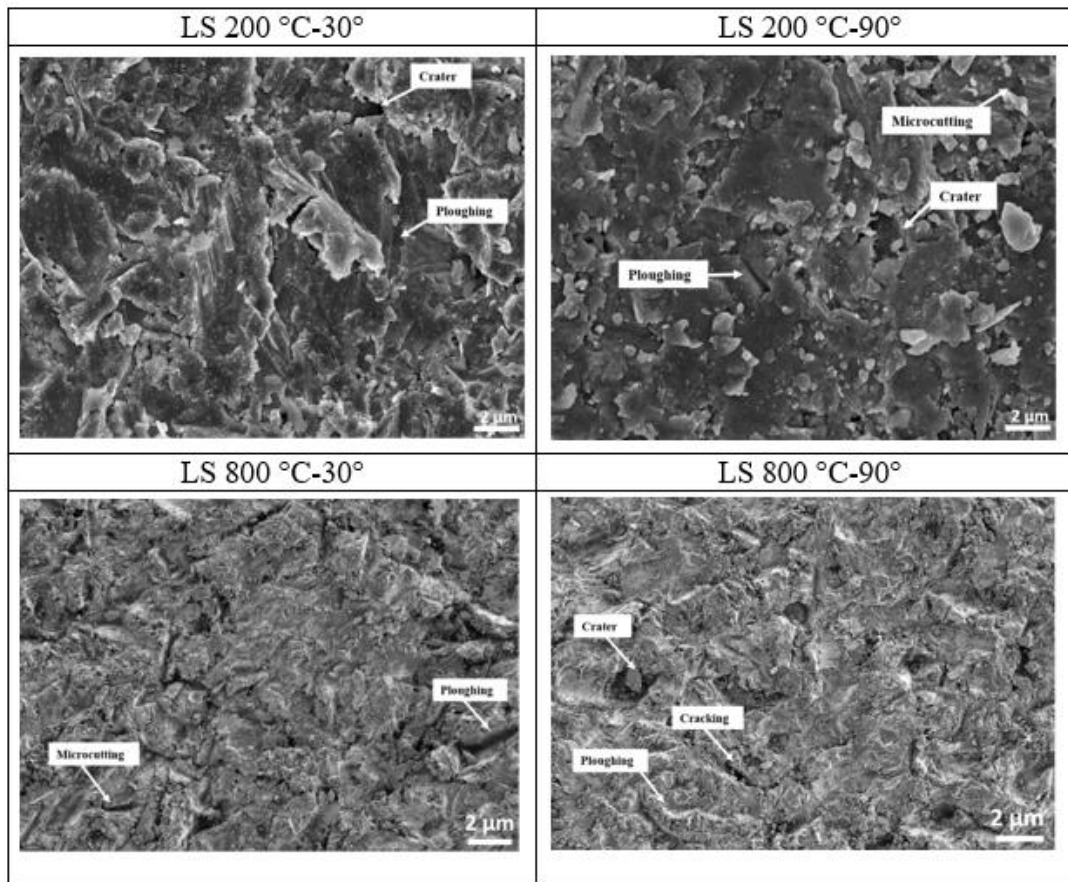


Figure 7.29 High magnification SEM images of laser-treated samples exposed to various erosion conditions

Instances of complete spallation removal of laser-glazed layer have been reported in coatings upon erosion (Tsai et al. 2007). Such spallation tendencies are not observed in the considered laser-treated samples. Tsai reports a one-third erosion in laser-treated YSZ samples than the APS-coated samples at 30°, 45°, and 90°. According to the average erosion values and steady-state erosion rate of the considered 70 wt.% Al<sub>2</sub>O<sub>3</sub> - 30 wt.% Sm<sub>2</sub>SrAl<sub>2</sub>O<sub>7</sub> TBCs, the laser-treated samples show a 7 % lower erosion than the as-coated samples. The laser-modified coating, with better surface roughness and lesser porosities, resist erosion slightly better than the as-coated samples. The comparatively dense layer after re-solidification offers increased resistance to impact. This looks into the possibility of optimizing the laser treatment on the composite samples, considering multiple factors such as reduction in porosity, reduction in surface roughness, and cracking tendencies, to offer a higher degree of resistance to the system.



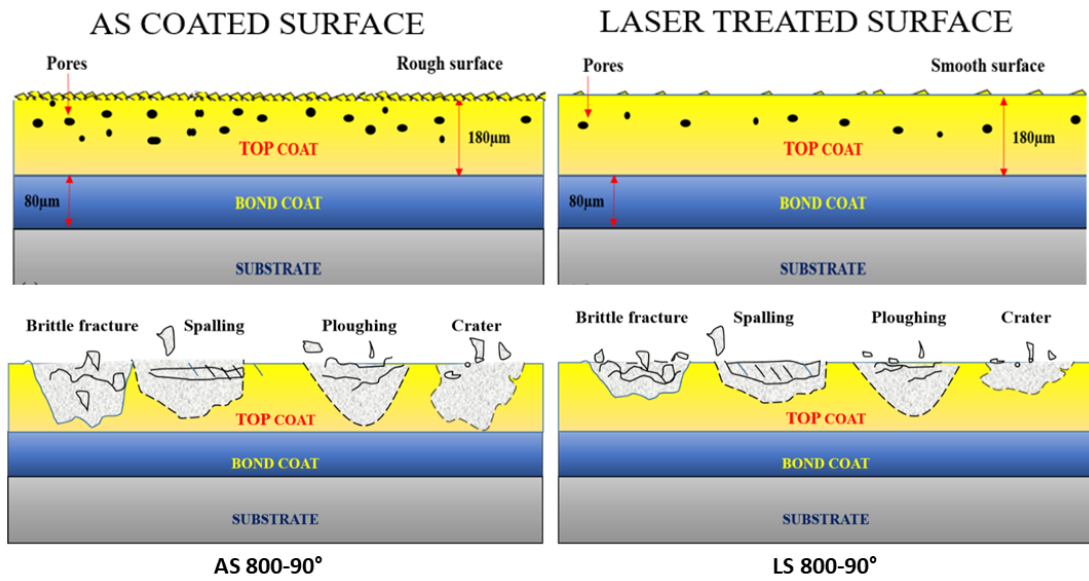


Figure 7.30 Schematic diagram of erosion mechanisms observed in as-coated and laser-treated samples at 800 °C (not in scale)

## 7.4 Summary of test results of laser-treated sample

### **Isothermal oxidation test**

- In the laser-treated 70 wt.% Al<sub>2</sub>O<sub>3</sub> - 30 wt.% Sm<sub>2</sub>SrAl<sub>2</sub>O<sub>7</sub> composite TBCs, a nearly continuous alumina TGO is identified at the interface after oxidation at 1100 °C.
- The TGO thickness increases with exposure time from 30 h to 150 h at 1100 °C.
- No major spinel oxides were formed on the surface or interface of the samples after oxidation.
- The laser-treated systems showed a comparatively lower weight gain and a lower average TGO thickness than as-coated samples.
- The as-coated and laser-treated samples exhibited similar oxidation kinetics following the parabolic law.

### **Hot corrosion test**

- The laser-treated samples showed a higher hot corrosion resistance than the as-coated samples under marine and aviation conditions.
- SmVO<sub>4</sub> and SrSO<sub>4</sub> were the major corrosion products under the aviation and marine test conditions.

### **Solid particle erosion test**

- On average, the laser-treated samples achieved a 7 % higher erosion resistance than the as-coated samples, due to the closure of porosities and an improvement in hardness.
- The laser-treated samples showed a mixed mode of removal with brittle and ductile mechanisms involved.

## 8 Conclusions

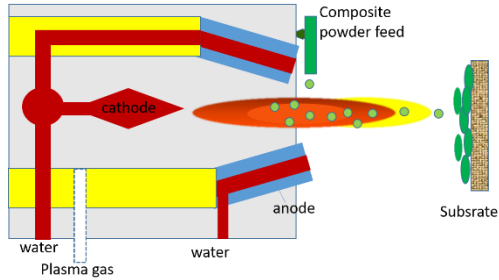
The composite thermal barrier coating system with top coat composition  $\text{Al}_2\text{O}_3 - \text{Sm}_2\text{SrAl}_2\text{O}_7$  has been prepared by atmospheric plasma spraying employing the SSA powder synthesized through molten salt synthesis technique. For the sake of comparison, the samples were treated with an Nd: YAG laser beam to improve the surface properties. The performance of the developed coatings in high temperature oxidation, hot corrosion, and erosion atmospheres were examined and the following conclusions were derived.

- The isothermal oxidation tests at 1100 °C showed that the developed coatings follows a parabolic law of oxidation weight gain with a continuous alumina TGO at the interface.
- The hot corrosion resistance of the samples was inferior in the case of marine atmospheres than that in case of aviation atmospheres.
- The interaction of the composite coatings with aviation and marine conditions resulted in the formation of  $\text{SmVO}_4$  and  $\text{SrSO}_4$  on the surface.
- The erosion resistance of the samples tends to decline with an increase in temperature.
- The samples showed a mixed mode of material removal with brittle and ductile mechanisms.
- The laser treatment resulted in a smooth surface with lesser open porosities and unmolten particles on the surface. Only trivial difference in phases were noted between the as-coated and laser-treated systems. An improved hardness is achieved by laser treatment.
- The oxidation of laser-treated samples showed similar mechanism with a lower parabolic rate constant and lower oxide growth at interface.
- The hot corrosion resistance of the samples were increased after laser treatment by virtue of the closure of open porosities.
- The laser-treated samples showed a better solid particle erosion resistance than the as-coated samples

## 8.1 Scope for future works

- Development of other  $\text{Ln}_2\text{SrAl}_2\text{O}_7$  materials and the feasibility in TBC applications can be performed.
- Performance of multi-layer systems with  $\text{Sm}_2\text{SrAl}_2\text{O}_7$  and conventional materials such as YSZ, alumina can be examined.
- Researches on ensuring a uniform melting in laser treatment by addition of binders can be performed.

# Graphical illustration of performed work



**Synthesis of samarium strontium aluminate (SSA) powder**

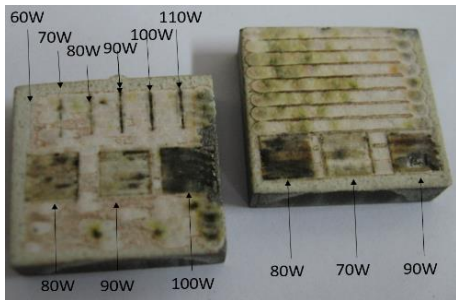


**Preparation of alumina + SSA composite top coat powder**

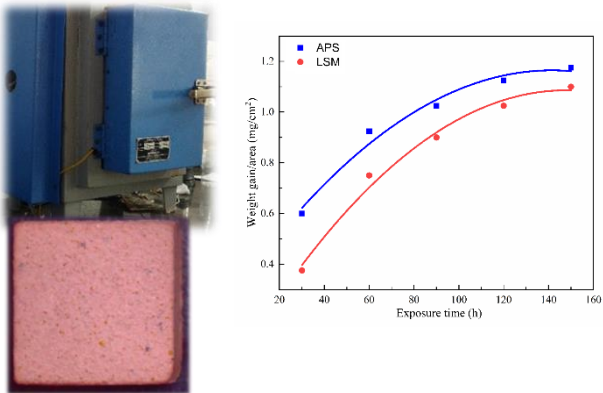
**Coating development by atmospheric plasma spray**

**Laser modification of surface**

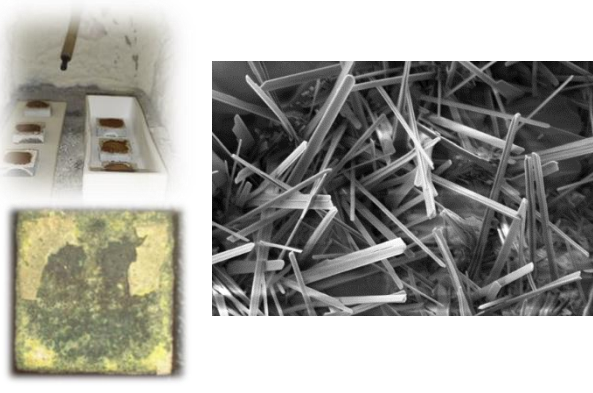
**Characterization of developed samples**



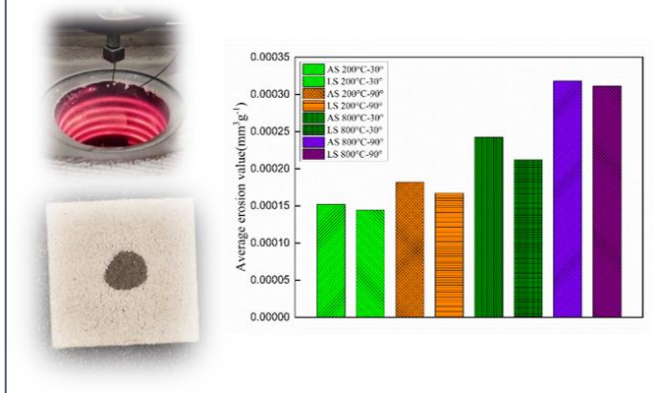
**Isothermal oxidation test**  
Temperature: 1100 °C



**Hot corrosion test**  
Temperature: 700 °C and 900 °C



**High temperature erosion test**  
Temperature: 200 °C and 800 °C





## References

- Afrasiabi, A., Saremi, M., and Kobayashi, A. (2008). "A comparative study on hot corrosion resistance of three types of thermal barrier coatings : YSZ , YSZ + Al<sub>2</sub>O<sub>3</sub> and YSZ / Al<sub>2</sub>O<sub>3</sub>." *Mater. Sci. Eng. A*, 478, 264–269.
- Ahmaniemi, S., Vuoristo, P., and Mäntylä, T. (2004). "Mechanical and elastic properties of modified thick thermal barrier coatings." *Mater. Sci. Eng. A*, 366(1), 175–182.
- Akca, E., and Gürsel, A. (2015). "A Review on Superalloys and IN718 Nickel-Based INCONEL Superalloy." *Period. Eng. Nat. Sci.*, 3(1).
- Alexander, H., Breuer, D., and Technologies, C. S. (2020). *Shot Peening and Thermal Spray Coatings : Complementary Surface Treatments*.
- Alqallaf, J., Ali, N., Teixeira, J. A., and Addali, A. (2020). "Solid particle erosion behaviour and protective coatings for gas turbine compressor blades-A review." *Processes*, (8).
- Amaya, C., Aperador, W., Caicedo, J. C., Espinoza-Beltrán, F. J., Muñoz-Saldaña, J., Zambrano, G., and Prieto, P. (2009). "Corrosion study of Alumina/Yttria-Stabilized Zirconia (Al<sub>2</sub>O<sub>3</sub>/YSZ) nanostructured Thermal Barrier Coatings (TBC) exposed to high temperature treatment." *Corros. Sci.*, 51(12), 2994–2999.
- Amin, S., and Panchal, H. (2016). "A Review on Thermal Spray Coating Processes." *Int. J. Curr. Trends Eng. Res.*, 2(4), 556–563.
- Andersson, J. M. (2005). "Controlling the Formation and Stability of Alumina Phases." *Thesis*, Linköping University.
- Arshad, A., Yajid, M. A. M., and Idris, M. H. (2021). "Microstructural characterization of modified plasma spray LZ/YSZ thermal barrier coating by laser glazing." *Mater. Today Proc.*, 39, 941–946.
- ASM Aerospace specification Metals Inc. (2014). *ASM Material datasheet*.
- Aust, J., and Pons, D. (2019). "Taxonomy of gas turbine blade defects." *Aerospace*, 6(5).

- Avci, A., Akdogan Eker, A., and Karabas, M. (2020). "An investigation of oxidation, hot corrosion, and thermal shock behavior of atmospheric plasma sprayed YSZ- Al<sub>2</sub>O<sub>3</sub> composite thermal barrier coatings." *Int. J. Mater. Res.*, (111), 1–14.
- Bahadur, S., and Badruddin, R. (1990). "Erodent particle characterization and the effect of particle size and shape on erosion." *Wear*, 138(1–2), 189–208.
- Bajpai, P., Das, A., Bhattacharya, P., Madayi, S., Kulkarni, K., and Omar, S. (2015). "Hot Corrosion of Stabilized Zirconia Thermal Barrier Coatings and the Role of Mg Inhibitor." *J. Am. Ceram. Soc.*, 98(8), 2655–2661.
- Baskaran, T. (2018). "Synthesis and development of Sm<sub>2</sub>SrAl<sub>2</sub>O<sub>7</sub> based air plasma sprayed ceramic thermal barrier coatings: oxidation, hot corrosion and high temperature erosion study.", Thesis, National Institute of Technology, Karnataka.
- Baskaran, T., and Arya, S. B. (2017). "Role of thermally grown oxide and oxidation resistance of samarium strontium aluminate based air plasma sprayed ceramic thermal barrier coatings." *Surf. Coat. Technol.*, 326, 299–309.
- Baskaran, T., and Arya, S. B. (2018). "Hot corrosion resistance of air plasma sprayed ceramic Sm<sub>2</sub>SrAl<sub>2</sub>O<sub>7</sub> (SSA) thermal barrier coatings in simulated gas turbine environments." *Ceram. Int.*, 44(15), 17695–17708.
- Buckner, C. A., Lafrenie, R. M., Dénonnée, J. A., (2016). "Processing Parameters for Selective Laser Sintering or Melting of Oxide Ceramics." *Addit. Manuf. High-performance Met. Alloy. - Model. Optim. Liq.*, INTECH open science, 13.
- Busca, G. (2014). "The surface of transitional aluminas: A critical review." *Catal. Today*, 226, 2–13.
- Caroline, W. (2021). "Erosion Behaviour of Thermal Barrier Coatings." Linköping University.
- Cemal, M., Cevik, S., Uzunonat, Y., and Diltemiz, F. (2012). "ALLVAC 718 Plus™ Superalloy for Aircraft Engine Applications." *Recent Adv. Aircr. Technol.*
- Cernuschi, F., Guardamagna, C., Capelli, S., Lorenzoni, L., Mack, D. E., and Moscatelli, A. (2016). "Solid particle erosion of standard and advanced thermal barrier



coatings.” *Wear*, 348–349, 43–51.

Chatha, S. S., Sidhu, H. S., and Sidhu, B. S. (2012). “High temperature hot corrosion behaviour of NiCr and Cr<sub>3</sub>C<sub>2</sub>-NiCr coatings on T91 boiler steel in an aggressive environment at 750°C.” *Surf. Coatings Technol.*, 206(19–20), 3839–3850.

Chen, Z., and Dong, Z. (2015). “Isothermal oxidation behavior of a thermal barrier coating prepared using EB-PVD.” *Surf. Interface Anal.*, 47(3), 377–383.

Daroonparvar, M., Azizi, M., Yajid, M., Yusof, N. M., and Bakhsheshi-rad, H. R. (2014). “Effect of Y<sub>2</sub>O<sub>3</sub> stabilized ZrO<sub>2</sub> coating with tri-model structure on bi-layered thermally grown oxide evolution in nano thermal barrier coating systems at elevated temperatures.” *J. Rare Earths*, 32(1), 57–77.

Daroonparvar, M., Yajid, M. A. M., Yusof, N. M., Farahany, S., Hussain, M. S., Bakhsheshi-Rad, H. R., Valefi, Z., and Abdolahi, A. (2013). “Improvement of thermally grown oxide layer in thermal barrier coating systems with nano alumina as third layer.” *Trans. Nonferrous Met. Soc. China (English Ed.)*, 23(5), 1322–1333.

Doleker, K. M., and Karaoglanli, A. C. (2017). “Comparison of oxidation behavior of YSZ and Gd<sub>2</sub>Zr<sub>2</sub>O<sub>7</sub> thermal barrier coatings (TBCs).” *Surf. Coatings Technol.*, 318(December 2016), 198–207.

Dorfman, M. R. (2012). “Thermal Spray Coatings.” *Chapter 19, handbook. Environ. Degrad. Mater. Second Ed.*, Elsevier Inc., 569–596.

Duraipandi, C., Khan M, A., Winowlin, J. J. T., Ghazaly, N. M., and Mashinini, P. M. (2021). “Solid particle erosion studies of thermally deposited alumina-titania coatings on an aluminum alloy.” *Int. J. Miner. Metall. Mater.*, 28(7), 1186–1193.

Eliaz, N., Shemesh, G., and Latanision, R. M. (2002). “Hot corrosion in gas turbine components.” *Eng. Fail. Anal.*, 9(1), 31–43.

Eskandarany, M. S. (2020). “Utilization of ball-milled powders for surface protective coating.” *Mech. Alloy.*, 309–334.

Feng, J., Xiao, B., Zhou, R., Pan, W., and Clarke, D. R. (2012). “Anisotropic elastic and thermal properties of the double perovskite slab-rock salt layer Ln<sub>2</sub>SrAl<sub>2</sub>O<sub>7</sub> (Ln =

La, Nd, Sm, Eu, Gd or Dy) natural superlattice structure.” *Acta Mater.*, 60(8), 3380–3392.

Fiedler, H. C. (1984). “The effect of structure on the thermal conductivity of plasma sprayed alumina.” *Mater. Res. Symp. Proc.*, 173–180.

Fox, A. C., and Clyne, T. W. (2004). “Oxygen transport by gas permeation through the zirconia layer in plasma sprayed thermal barrier coatings.” *Surf. Coatings Technol.*, 184(2–3), 311–321.

Fredy James J, Arya, S. B., and Tailor, S. (2022). “Erosion behavior of  $\text{Al}_2\text{O}_3 + \text{Sm}_2\text{SrAl}_2\text{O}_7$  composite thermal barrier coatings.” *Mater. Today Proc.*, 66, 3853–3858.

Fu, L. B., Zhang, W. L., Li, S. M., Li, Y. T., Li, W., Sun, J., Wang, T. G., Jiang, S. M., Gong, J., and Sun, C. (2022). “Oxidation behavior of NiCrAlYSi coatings with Re-based diffusion barriers on two superalloys.” *Corros. Sci.*, 198.

Furrer, D., and Fecht, H. (1999). “Ni-based superalloys for turbine discs.” *Jom*, 51(1), 14–17.

Ganvir, A., Vaidhyanathan, V., Markocsan, N., Gupta, M., Pala, Z., and Lukac, F. (2018). “Failure analysis of thermally cycled columnar thermal barrier coatings produced by high-velocity-air fuel and axial-suspension-plasma spraying: A design perspective.” *Ceram. Int.*, 44(3), 3161–3172.

Ghasemi, R., Shoja-Razavi, R., Mozafarinia, R., and Jamali, H. (2014). “The influence of laser treatment on thermal shock resistance of plasma-sprayed nanostructured yttria stabilized zirconia thermal barrier coatings.” *Ceram. Int.*, 40(PART A), 347–355.

Gomez, J., Rico, A., Múñez, C. J., Poza, P., and Utrilla, V. (2009). “Correlation of mechanical properties and electrochemical impedance spectroscopy analysis of thermal barrier coatings.” *Surf. Coat. Technol.*, 204(6–7), 812–815.

Guo, L., Xin, H., Zhang, Z., Zhang, X., and Ye, F. (2020). “Microstructure modification of  $\text{Y}_2\text{O}_3$  stabilized  $\text{ZrO}_2$  thermal barrier coatings by laser glazing and the effects on the hot corrosion resistance.” *J. Adv. Ceram.*, 9(2), 232–242.

Gurrappa, I. (1999). “Hot corrosion behavior of CM 247 LC alloy in  $\text{Na}_2\text{SO}_4$  and NaCl

environments.” *Oxid. Met.*, 51(5), 353–382.

Han, Y., Zhu, Z., Zhang, B., Chu, Y., Zhang, Y., and Fan, J. (2018). “Effects of process parameters of vacuum pre-oxidation on the microstructural evolution of CoCrAlY coating deposited by HVOF.” *J. Alloys Compd.*, 735, 547–559.

Huang, K., 1, W. L., Pan, K., Lin, X., and Wang, A. (2020). “High Temperature Oxidation and Thermal Shock Properties of  $\text{La}_2\text{Zr}_2\text{O}_7$  Thermal Barrier Coatings Deposited on Nickel-Based Superalloy by Laser-Cladding.” *Coatings*, 10, 1–3.

Jana, P., Jayan, P. S., Mandal, S., and Biswas, K. (2017). “Hot corrosion behaviour of rare-earth magnesium hexaaluminate based thermal barrier coatings under molten sulphate-vanadate salts.” *Surf. Coat. Technol.*, 322, 108–119.

Jarvis, E., and Carter, E. (2002). “The role of reactive elements in thermal barrier coatings.” *Comput. Sci. Eng.*, (1), 33–41.

Jonnalagadda, K. P., Mahade, S., Nicholas, C., Bjo, S., and Peng, R. L. (2017). “Hot Corrosion Mechanism in Multi-Layer Suspension Plasma Sprayed  $\text{Gd}_2\text{Zr}_2\text{O}_7/\text{YSZ}$  Thermal Barrier Coatings in the Presence of  $\text{V}_2\text{O}_5+\text{Na}_2\text{SO}_4$ .” *J. Therm. spray Technol.*, (26), 140–149.

Kaplan, M., Uyaner, M., Avcu, E., Yildiran Avcu, Y., and Karaoglanli, A. C. (2018). “Solid particle erosion behavior of thermal barrier coatings produced by atmospheric plasma spray technique.” *Mech. Adv. Mater. Struct.*, (June), 1–7.

Karabaş, M., Bal, E., and Taptik, Y. (2017). “Hot Corrosion Behaviour of Plasma Sprayed Alumina + YSZ Particle Composite Coating 1.” *Prot. Met. Phys. Chem. Surfaces*, 53(5), 859–863.

Keyvani, A., Saremi, M., Heydarzadeh Sohi, M., Valefi, Z., Yeganeh, M., and Kobayashi, A. (2014). “Microstructural stability of nanostructured YSZ-alumina composite TBC compared to conventional YSZ coatings by means of oxidation and hot corrosion tests.” *J. Alloys Compd.*, 600, 151–158.

Khan, M. A., Anand, A. V., Duraiselvam, M., Rao, K. S., Singh, R. A., and Jayalakshmi, S. (2021). “Thermal shock resistance and thermal insulation capability of

laser-glazed functionally graded lanthanum magnesium hexaluminate/yttria-stabilised zirconia thermal barrier coating.” *Materials (Basel)*, 14(14).

Klement, U., Ekberg, J., and Ganvir, A. (2017). “EBSD analysis and assessment of porosity in thermal barrier coatings produced by axial suspension plasma spraying (ASPS).” *Mater. Sci. Forum*, 879, 972–977.

Kokini, K., Takeuchi, Y. R., and Choules, B. D. (1996). “Surface thermal cracking of thermal barrier coatings owing to stress relaxation: Zirconia vs. Mullite.” *Surf. Coatings Technol.*, 82(1–2), 77–82.

Krishnamurthy, N., Murali, M. S., Venkataraman, B., and Mukunda, P. G. (2012). “Characterization and solid particle erosion behavior of plasma sprayed alumina and calcia-stabilized zirconia coatings on Al-6061 substrate.” *Wear*, 274–275, 15–27.

Kuroda, S., Kawakita, J., Watanabe, M., and Katanoda, H. (2008). “Warm spraying - A novel coating process based on high-velocity impact of solid particles.” *Sci. Technol. Adv. Mater.*, 9(3).

Lampke, T., Meyer, D., Alisch, G., Wielage, B., Pokhmurska, H., Klapkiv, M., and Student, M. (2011). “Corrosion and wear behavior of alumina coatings obtained by various methods.” *Mater. Sci.*, 46(5), 591–598.

Leushake, U., Krell, T., Schulz, U., Peters, M., Kaysser, W. A., and Rabin, B. H. (1997). “Microstructure and phase stability of EB-PVD alumina and alumina/zirconia for thermal barrier coating applications.” *Surf. Coatings Technol.*, 94–95, 131–136.

Li, C., Yang, G., and Ohmori, A. (2006). “Relationship between particle erosion and lamellar microstructure for plasma-sprayed alumina coatings.” *Wear*, 260, 1166–1172.

Li, S., Liu, Z. G., and Ouyang, J. H. (2010). “Hot corrosion behaviour of  $\text{Yb}_2\text{Zr}_2\text{O}_7$  ceramic coated with  $\text{V}_2\text{O}_5$  at temperatures of 600–800°C in air.” *Corros. Sci.*, 52(10), 3568–3572.

Li, W., Li, Z., An, G., Cheng, B., Song, Q., Sun, J., Vaganov, V., Wang, C., and Goransky, G. (2022). “Isothermal Oxidation TGO Growth Behaviors of Laser-Remolten LZO/YSZ Thermal Barrier Coatings.” *Coatings*, 12(2).

- Li, X., Huang, X., Yang, Q., and Tang, Z. (2014). "Effects of substrate material and TBC structure on the cyclic oxidation resistance of TBC systems." *Surf. Coatings Technol.*, 258, 49–61.
- Liu, S., Tian, Z., Shen, L., Qiu, M., and Gao, X. (2021). "Monte Carlo simulation of ceramic grain growth during laser ablation processing." *Optik (Stuttg.)*, 227, 165569.
- Liu, X., Wang, T., Li, C., Zheng, Z., and Li, Q. (2016). "Microstructural evolution and growth kinetics of thermally grown oxides in plasma sprayed thermal barrier coatings." *Prog. Nat. Sci. Mater. Int.*, 26(1), 103–111.
- Mahade, S., Curry, N., Björklund, S., Markocsan, N., and Nylén, P. (2016). "Failure analysis of Gd<sub>2</sub>Zr<sub>2</sub>O<sub>7</sub>/YSZ multi-layered thermal barrier coatings subjected to thermal cyclic fatigue." *J. Alloys Compd.*, 689, 1011–1019.
- Mahade, S., Venkat, A., Curry, N., Leitner, M., and Joshi, S. (2021). "Erosion performance of atmospheric plasma sprayed thermal barrier coatings with diverse porosity levels." *Coatings*, 11(1), 1–21.
- Matikainen, V., Niemi, K., Koivuluoto, H., and Vuoristo, P. (2014). "Abrasion, erosion and cavitation erosion wear properties of thermally sprayed alumina based coatings." *Coatings*, 4(1), 18–36.
- Miller, R. A. (1997). "Thermal barrier coatings for aircraft engines: History and directions." *J. Therm. Spray Technol.*, 6(1), 35–42.
- Mohammadi, M., Kobayashi, A., Javadpour, S., and Jahromi, S. A. J. (2018). "Evaluation of hot corrosion behaviors of Al<sub>2</sub>O<sub>3</sub>-YSZ composite TBC on gradient MCrAlY coatings in the presence of Na<sub>2</sub>SO<sub>4</sub>-NaVO<sub>3</sub> salt." *Vacuum*, (April), 0–1.
- Mohan G Hebsur. (2002). "Oxidation resistant and low coefficient of thermal expansion NiAl-CoCrAlY alloy."
- Moriya, R., Iguchi, M., Sasaki, S., and Yan, J. (2016). "Surface Property Modification of Alumina Sprayed Coatings Using Nd:YAG Laser." *Procedia CIRP*, 42, 464–469.
- Moskal, G. (2009). "Thermal barrier coatings : characteristics of microstructure and properties , generation and directions of development of bond." *Manuf. Eng.*, 37(2),

323–331.

Mrowec, S., and Stoklosa, A. (1974). “Calculations of Parabolic Rate Constants for Metal Oxidation.” *Oxid. Met.*, 8(6), 379–391.

Munawar, A. U., Schulz, U., Cerri, G., and Lau, H. (2014). “Microstructure and cyclic lifetime of Gd and Dy-containing EB-PVD TBCs deposited as single and double-layer on various bond coats.” *Surf. Coatings Technol.*, 245, 92–101.

Múnez, C. J., Gómez-García, J., Sevillano, F., Poza, P., and Utrilla, M. V. (2011). “Improving thermal barrier coatings by laser remelting.” *J. Nanosci. Nanotechnol.*, 11(10), 8724–8729.

Muruges, L., and Scattergood, R. O. (1991). “Effect of erodent properties on the erosion of alumina.” *J. Mater. Sci.*, 26(20), 5456–5466.

Naib, S. (2016). “Modelling the influence of water droplet impacts on steam turbine blade surfaces.”, Thesis, University of Starttgart.

Narita, T., Hayashi, S., Lang, F. Q., and Thosin, K. Z. (2005). “The Role of Bond Coat in Advanced Thermal Barrier Coating.” *Mater. Sci. Forum*, 502, 99–104.

Nath, S., Manna, I., and Majumdar, J. D. (2014). “Kinetics and mechanism of isothermal oxidation of compositionally graded yttria stabilized zirconia (YSZ) based thermal barrier coating.” *Corros. Sci.*, 88, 10–22.

Nicholls, J. R., Deakin, M. J., and Rickerby, D. S. (1999). “A comparison between the erosion behaviour of thermal spray and electron beam physical vapour deposition thermal barrier coatings.” *Wear*, 233–235, 352–361.

Ning, S. M., Yu, Q. M., Liu, T. J., Zhang, K., Zhang, H. L., Wang, Y., and Li, Z. H. (2022). “Influence of particle shape on erosion behavior of EB-PVD thermal barrier coatings.” *Ceram. Int.*, 48(6), 8627–8640.

Nouri, A., and Sola, A. (2019). “Powder morphology in thermal spraying.” *J. Adv. Manuf. Process.*, 1(3).

Patnaik, P. C. (n.d.). “State of the Art and Future Trends in the Development of Thermal Barrier Coating Systems.” (2006), 1–20.

- Persson, J., and Nygren, M. (1992). "Interpretation of the Parabolic and Nonparabolic Oxidation Behavior of Silicon Oxynitride." *J. Am. Ceram. Soc.*, 75(12), 3377–84.
- Presby, M. J., and Harder, B. J. (2021). "Solid particle erosion of a plasma spray – physical vapor deposition environmental barrier coating in a combustion environment." *Ceram. Int.*, 47(17), 24403–24411.
- Psyllaki, P. P., Jeandin, M., and Pantelis, D. I. (2001). "Microstructure and wear mechanisms of thermal-sprayed alumina coatings." *Mater. Lett.*, 47(January), 77–82.
- Puspitasari, P., Andoko, A., and Kurniawan, P. (2021). "Failure analysis of a gas turbine blade: A review." *IOP Conf. Ser. Mater. Sci. Eng.*, 1034(1), 012156.
- Qureshi, I. N., Shahid, M., and Nusair Khan, A. (2016). "Hot Corrosion of Yttria-Stabilized Zirconia Coating, in a Mixture of Sodium Sulfate and Vanadium Oxide at 950 °C." *J. Therm. Spray Technol.*, 25(3), 567–579.
- Ramachandran, C. S., Balasubramanian, V., and Ananthapadmanabhan, P. V. (2013). "Erosion of atmospheric plasma sprayed rare earth oxide coatings under air suspended corundum particles." *Ceram. Int.*, 39(1), 649–672.
- Ramaswamy, P., Seetharamu, S., and Raob, (1997). "Al<sub>2</sub>O<sub>3</sub>-ZrO<sub>2</sub> composite coatings for thermal barrier applications." *Compos. Sci. Technol.*, 57, 81–89.
- Ramesh, M., and Marimuthu, K. (2020). "Microstructural, thermal and wear behavior of YSZ/Al<sub>2</sub>O<sub>3</sub> thermal barrier coatings for gun barrel applications." *Dig. J. Nanomater. Biostructures*, 15(2), 527–536.
- Ramesh, M. R., Prakash, S., Nath, S. K., Sapra, P. K., and Venkataraman, B. (2010). "Solid particle erosion of HVOF sprayed WC-Co/NiCrFeSiB coatings." *Wear*, 269(3–4), 197–205.
- Ramm, D. A. J., Hutchings, M., and Clyne, T. W. (1993). "Erosion resistance and adhesion of composite metal/ceramic coatings produced by plasma spraying." *J. Phys.*, 3(7), 913–919.
- Reza, M. S., Aqida, S. N., and Ismail, I. (2018). "Laser surface modification of Yttria

Stabilized Zirconia (YSZ) thermal barrier coating on AISI H13 tool steel substrate.” *IOP Conf. Ser. Mater. Sci. Eng.*

Sadeghi, E., Markocsan, N., and Joshi, S. (2019). *Advances in Corrosion-Resistant Thermal Spray Coatings for Renewable Energy Power Plants. Part I: Effect of Composition and Microstructure. J. Therm. Spray Technol.*, Springer US.

Saral, U., and Toplan, N. (2009). “Thermal cycle properties of plasma sprayed YSZ/Al<sub>2</sub>O<sub>3</sub> thermal barrier coatings.” *Surf. Eng.*, 25(7), 541–547.

Saremi, M., Afrasiabi, A., and Kobayashi, A. (2008). “Microstructural analysis of YSZ and YSZ/Al<sub>2</sub>O<sub>3</sub> plasma sprayed thermal barrier coatings after high temperature oxidation.” *Surf. Coatings Technol.*, 202(14), 3233–3238.

Singh, H., Puri, D., and Prakash, S. (2005). “Some studies on hot corrosion performance of plasma sprayed coatings on a Fe-based superalloy.” *Surf. Coatings Technol.*, 192(1), 27–38.

Singh, H., Puri, D., and Prakash, S. (2007). “An overview of Na<sub>2</sub>SO<sub>4</sub> AND/OR V<sub>2</sub>O<sub>5</sub> induced hot corrosion of Fe- and Ni-Based superalloys.” *Rev. Adv. Mater. Sci.*, 16(1–2), 27–50.

Smialek, J. L., Jacobson, N. S., Gleeson, B., Hovis, D. B., and Heuer, A. H. (2013). *Oxygen Permeability and Grain-Boundary Diffusion Applied to Alumina Scales. Nasa Tm 217855.*

Smith, M. F. (2007). “Comparing cold spray with thermal spray coating technologies.” *Cold Spray Mater. Depos. Process Fundam. Appl.*, 43–61.

Soare, A., Csaki, I., Sohaciu, M., Oprea, C., Soare, S., Costina, I., and Petrescu, M. I. (2017). “New Bond Coat Materials for Thermal Barrier Coating Systems Processed Via Different Routes.” *IOP Conf. Ser. Mater. Sci. Eng.*, 209(1), 1–6.

Soares, C. (2008). *Gas Turbines: An Introduction and Applications. Gas Turbines*, <http://dx.doi.org/10.1016/B978-0-12-410461-7.00001-8>.

Song, D., Song, T., Paik, U., Lyu, G., Jung, Y.-G., Choi, B.-G., Kim, I.-S., and Zhang, J. (2019). “Crack-Growth Behavior in Thermal Barrier Coatings with Cyclic Thermal



Exposure.” *Coatings*, 9(6), 365.

Song, X., Meng, F., Kong, M., Liu, Z., Huang, L., Zheng, X., and Zeng, Y. (2017). “Relationship between cracks and microstructures in APS YSZ coatings at elevated temperatures.” *Mater. Charact.*, 131(February), 277–284.

Sreedhar, G., Alam, M., and Raja, V. S. (2009). “Surface & Coatings Technology Hot corrosion behaviour of plasma sprayed YSZ/Al<sub>2</sub>O<sub>3</sub> dispersed NiCrAlY coatings on Inconel-718 superalloy.” *Surf. Coat. Technol.*, 204(3), 291–299.

Stecura, S. (1985). “Optimization of the NiCrAl-Y/ZrO<sub>2</sub>-Y<sub>2</sub>O<sub>3</sub> Thermal Barrier System.” *Nasa Tech. Memo.*, 86905.

Strang, A. (2000). *Materials for high temperature power generation and process plant applications*.

Swadźba, R. (2018). “Interfacial phenomena and evolution of modified aluminide bondcoatings in Thermal Barrier Coatings.” *Appl. Surf. Sci.*, 445, 133–144.

Tao, S., Yang, J., Li, W., Shao, F., Zhong, X., Zhao, H., Zhuang, Y., Ni, J., Tao, S., and Yang, K. (2020). “Thermal stability of plasma-sprayed thick thermal barrier coatings using triplex ProTM-200 torch.” *Coatings*, 10(9), 1–16.

Tarasi, F., Medraj, M., Dolatabadi, A., Oberste-Berghaus, J., and Moreau, C. (2010). “Phase formation and transformation in alumina/YSZ nanocomposite coating deposited by suspension plasma spray process.” *J. Therm. Spray Technol.*, 19(4), 787–795.

Tawancy. (1998). “Failure Mechanism of a thermal barrier coating system on a Ni base superalloy.” *J. Mater. Sci.*, 33, 681–686.

Thomas, A., El-Wahabi, M., Cabrera, J. M., and Prado, J. M. (2006). “High temperature deformation of Inconel 718.” *J. Mater. Process. Technol.*, 177(1–3), 469–472.

Torkashvand, K., Poursaeidi, E., and Mohammadi, M. (2018). “Effect of TGO thickness on the thermal barrier coatings life under thermal shock and thermal cycle loading.” *Ceram. Int.*, 44(8), 9283–9293.

Tsai, P. C., Lee, J. H., and Chang, C. L. (2007). “Improving the erosion resistance of plasma-sprayed zirconia thermal barrier coatings by laser glazing.” *Surf. Coatings*

*Technol.*, 202(4–7), 719–724.

Tucker C, R. (1994). “Thermal Spray Coatings.” *ASM Handbook.*, 5(Surf. Eng.), 497–509.

Wang, D., Tian, Z., Shen, L., Liu, Z., and Huang, Y. (2014). “Effects of laser remelting on microstructure and solid particle erosion characteristics of  $ZrO_2$ -7wt%  $Y_2O_3$  thermal barrier coating prepared by plasma spraying.” *Ceram. Int.*, 40(6), 8791–8799.

Wang, X., Guo, L., Peng, H., Zheng, L., Guo, H., and Gong, S. (2015). “Hot-corrosion behavior of a  $La_2Ce_2O_7$ /YSZ thermal barrier coating exposed to  $Na_2SO_4+V_2O_5$  or  $V_2O_5$  salt at 900 °c.” *Ceram. Int.*, 41(5), 6604–6609.

Wellman, R. G., and Nicholls, J. R. (2008). “Erosion, corrosion and erosion-corrosion of EB PVD thermal barrier coatings.” *Tribol. Int.*, 41(7), 657–662.

Westergård, R., Erickson, L. C., Axén, N., Hawthorne, H. M., and Hogmark, S. (1998). “The erosion and abrasion characteristics of alumina coatings plasma sprayed under different spraying conditions.” *Tribol. Int.*, 31(5), 271–279.

Xiaoyun, X. I. E., Hongbo, G. U. O., Shengkai, G., and Huibin, X. U. (2012). “Hot corrosion behavior of double-ceramic-layer  $LaTi_2Al_9O_{19}$ /YSZ thermal barrier coatings.” *Chinese J. Aeronaut.*, 25(1), 137–142.

Yang, Z., Wang, W., Deng, S., Fang, H., Yang, T., and Wang, L. (2021). “Thermal shock behavior and particle erosion resistance of toughened GZ coatings prepared by atmospheric plasma spraying.” *Coatings*, 11(12).

Yugeswaran, S., Kobayashi, A., and Ananthapadmanabhan, P. V. (2012). “Hot corrosion behaviors of gas tunnel type plasma sprayed  $La_2Zr_2O_7$  thermal barrier coatings.” *J. Eur. Ceram. Soc.*, 32(4), 823–834.

Zhang, C., Fei, J., Guo, L., Yu, J., Zhang, B., Yan, Z., and Ye, F. (2018). “Thermal cycling and hot corrosion behavior of a novel  $LaPO_4$ /YSZ double-ceramic-layer thermal barrier coating.” *Ceram. Int.*, 44(8), 8818–8826.

Zhang, H., and LeBlanc, S. (2016). “Processing parameters for selective laser sintering or melting of oxide ceramics.” *Intech*, INTECH open science, 13.

Zhang, H., and LeBlanc, S. (2018). "Additive Manufacturing of High-performance Metals and Alloys - Modeling and Optimization liquid." *Intech, C. A.*, 89–124.

Zhang, Z., and Modest, F. (1998). "Temperature-Dependent Absorptances of Ceramics for Nd : YAG and CO<sub>2</sub> Laser Processing Applications." *Trans. ASME*, 120(May), 322–327.

Zhu, C., Javed, A., Li, P., Yang, F., Liang, G. Y., and Xiao, P. (2012). "A study of the microstructure and oxidation behavior of alumina/yttria-stabilized zirconia (Al<sub>2</sub>O<sub>3</sub>/YSZ) thermal barrier coatings." *Surf. Coatings Technol.*, 212, 214–222.

Zvereva, I., Smirnov, Y., Gusarov, V., Popova, V., and Choisnet, J. (2003). "Complex aluminates RE<sub>2</sub>SrAl<sub>2</sub>O<sub>7</sub>(RE = La, Nd, Sm-Ho): Cation ordering and stability of the double perovskite slab-rocksalt layer P2/RS intergrowth." *Solid State Sci.*, 5(2), 343–349.



## Bio-Data

### PERSONAL DETAILS

Name: Fredy James J

Address: Thumbiamkuzhiyil

Kuravilangad

Kottayam

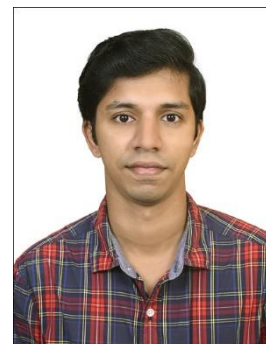
Kerala,

Pin-686633

Date of Birth : 14-02-1991

Email: [fredyjamesj@gmail.com](mailto:fredyjamesj@gmail.com)

Mobile: +91-8907652462



### EDUCATIONAL QUALIFICATIONS

- ✓ **Doctor of Philosophy** (Thesis submitted)  
Title: Development of  $\text{Al}_2\text{O}_3$  -  $\text{Sm}_2\text{SrAl}_2\text{O}_7$  composite thermal barrier coatings for high temperature applications  
National Institute of Technology, Karnataka
- ✓ **Master of Technology**  
Industrial Metallurgy, 2013-15  
PSG College of Technology  
Anna University, Chennai.
- ✓ **Bachelor of Technology**  
Mechanical Engineering, 2008-12  
St. Joseph's College of Engineering and Technology  
Mahatma Gandhi University, Kottayam.

### PUBLICATIONS

#### Scientific Journals

1. Fredy James J, Shashi Bhushan Arya, Satish Tailor, "Hot corrosion behavior of  $\text{Al}_2\text{O}_3$  +  $\text{Sm}_2\text{SrAl}_2\text{O}_7$  composite thermal barrier coatings", Materials and Corrosion, 2022, 1-5, doi:10.1002/maco.20221340

2. Fredy James J, Shashi Bhushan Arya, Satish Tailor, "Erosion behavior of  $\text{Al}_2\text{O}_3$  +  $\text{Sm}_2\text{SrAl}_2\text{O}_7$  composite thermal barrier coatings", *Materials Today Proceedings*, 66, 2022, 3853-3858. <https://doi.org/10.1016/j.matpr.2022.06.294>
3. Fredy James J, Shashi Bhushan Arya, D Satish Kumar, "Isothermal oxidation characteristics of laser-treated  $\text{Al}_2\text{O}_3$  +  $\text{Sm}_2\text{SrAl}_2\text{O}_7$  composite thermal barrier coatings", *Materials and Corrosion*, April 2023, doi: 10.1002/maco.202313813.
4. Fredy James J, Shashi Bhushan Arya, S Yadav, C P Paul, "Effect of surface modification on erosion behavior of Alumina - Samarium strontium aluminate composite thermal barrier coatings", (Under Review in *Journal of Materials Engineering and Performance*).
5. Fredy James J, Shashi Bhushan Arya, "Hot corrosion of laser modified  $\text{Al}_2\text{O}_3$  -  $\text{Sm}_2\text{SrAl}_2\text{O}_7$  composite coatings in aviation and marine environments" (Under Review in *Transactions of Indian Institute of Metals*).

### **Book Chapter**

1. Shashi Bhushan Arya and Fredy James J, *Tribocorrosion: Fundamentals, Methods, and Materials*, Chapter 3 - Electrochemical methods in tribocorrosion 2021, ISBN: 978-0-12-818916-0, <https://doi.org/10.1016/C2018-0-04450-3>

### **Conferences**

1. Fredy James J, Kunal Bhole, Shashi Bhushan Arya, CMAS hot corrosion behavior of  $\text{Al}_2\text{O}_3$  +  $\text{Sm}_2\text{SrAl}_2\text{O}_7$  composite thermal barrier coatings, First National Thermal Spray Conference, NTSC-2023, 18-19 February 2023, Jodhpur.
2. Fredy James J, Shashi Bhushan Arya, Enhancement of corrosion resistance of  $\text{Al}_2\text{O}_3$  +  $\text{Sm}_2\text{SrAl}_2\text{O}_7$  composite thermal barrier coatings by laser treatment, International Conference on Corrosion and Coatings, CSIR-NML, Tata Steel, NIT Jamshedpur, 7-8 December 2022, Jamshedpur.

3. Fredy James J, Shashi Bhushan Arya, Satish Tailor, Erosion behavior of  $\text{Al}_2\text{O}_3$  +  $\text{Sm}_2\text{SrAl}_2\text{O}_7$  composite thermal barrier coatings, Symposium on Failure and Preventive Maintenance of Machineries March 8-9, 2022, (CSIR-CMERI) M.G. Avenue, Durgapur.
  
4. Fredy James J, Shashi Bhushan Arya, Johnkutty Eldho, A Venugopal, The oxidation behavior of air plasma sprayed ceramic  $\text{Sm}_2\text{SrAl}_2\text{O}_7$  composite thermal barrier coatings, International Symposium on Advanced Materials for Industrial and Societal Applications, NMD ATM, 13-16 November 2019, Thiruvananthapuram.